© Copyright 2021

Soohyung Lee

Theoretical and Experimental Investigations of Resonant Light-Matter Interactions in Ternary Metal Chalcogenide Nanocrystals

Soohyung Lee

A dissertation

submitted in partial fulfillment of the

requirements for the degree of

Doctor of Philosophy

University of Washington

2021

Reading Committee:

Vincent C. Holmberg, Chair

Lilo D. Pozzo

Qiuming Yu

Program Authorized to Offer Degree:

Chemical Engineering

University of Washington

Abstract

Theoretical and Experimental Investigations of Resonant Light-Matter Interactions in Ternary Metal Chalcogenide Nanocrystals

Soohyung Lee

Chair of the Supervisory Committee:
Vincent C. Holmberg
Chemical Engineering

The interaction of light with subwavelength nanomaterials has been extensively investigated for more than a century in both theoretical science and engineering. In particular, the resonant interaction of light with plasmonic metal nanocrystals (NCs) – including gold, silver, and platinum – has been of great interest in multiple fields of study due to their extraordinary optical effects in the near- and far-field enhancement via localized surface plasmon resonance (LSPR). Consequently, manipulation of light using plasmonic metal NCs has enabled the development of a broad range of applications from nonlinear optics to sensing. However, the nearly-fixed dielectric properties and high ohmic losses of metal NCs have been a central bottleneck for improving the performance of photonic and plasmonic devices.

The maturation of nanophotonics has often necessitated the search for novel materials. Recently, new emphasis has been placed on ternary chalcopyrite-phase copper iron sulfide

($CuFeS_2$) intermediate band semiconductor NCs as an alternative to plasmonic metal NCs due to their resonant light interactions that strongly absorb and scatter incident light in the visible region, analogous to the plasmonic response of metal NCs. Interestingly, however, the underlying physics of the optical properties of $CuFeS_2$ NCs are distinctly different from plasmonic metal NCs, since $CuFeS_2$ is an all-dielectric material having no free charges in their ground state. In order to fully realize its potential for technological applications, a detailed understanding of the unique optical properties of $CuFeS_2$ NCs is a prerequisite. In this regard, this dissertation explores, both theoretically and experimentally, the resonant optical properties of ternary metal chalcogenide intermediate band semiconductor NCs.

Herein, we present a set of experimental and computational results, allowing for a clear differentiation between two fundamentally different modes of resonant excitation present in ternary metal chalcogenide NC systems: (i) a quasi-static dielectric resonance (DR) and (ii) a LSPR. In the first part of the dissertation, we demonstrated that bornite-phase copper iron sulfide (Cu_5FeS_4) NCs exhibit tunable optical characteristics from visible to near-infrared that are strongly dependent on their iron content. Our experimental results on bornite-phase copper iron sulfide NCs showed that manipulating the iron content of the material modulates the intensity of the DR response, and moreover, that post-synthetic compositional manipulation via simple oxidative chemistry can be used to tune directly between the DR and LSPR mechanisms. We further confirmed an analogous DR-to-LSPR evolution in $CuFeS_2$ NCs subjected to the influence of oxidizing agents and added ions. In addition, electronic band structure calculations by density functional theory demonstrated that the presence of an intermediate band of states formed by empty Fe d-orbitals plays an important role in the occurrence of a DR in the visible-frequency regime.

In the second part of the dissertation, we expanded our knowledge on the DR properties of ternary metal chalcogenide NCs by developing a synthetic protocol for colloidal intermediate band silver iron sulfide ($AgFeS_2$) NCs. Through synthetic studies of $AgFeS_2$ NCs involving a two-step heterogeneous nucleation process, the synthesis of Ag seed NCs and their subsequent growth into $AgFeS_2$ NCs, we clearly differentiate between the DR and LSPR. Moreover, we confirm that increasing the gap between the valence band and the intermediate band causes a blue-shift of the DR in ternary metal chalcogenide intermediate band NC systems based on a comparative study of the DR properties of $AgFeS_2$ and $CuFeS_2$ NCs.

Taken together, this work represents a significant step forward in the understanding of the plasmonic-like optical response of intermediate-band-semiconductor ternary metal chalcogenide NCs, which could lead to important ramifications for future applications of these materials.

TABLE OF CONTENTS

LIST OF FIGURES

ACKNOWLEDGEMENTS

First and foremost, I would like to thank my family for their unconditional love and support. Especially, I am truly grateful to my parents for their support from 5000 miles away. They always believe in me and encourage me to finish my PhD studies. I would not have been able to complete this journey without their love and support.

I am indebted to many people for their help, support, and guidance throughout my studies at the University of Washington. I would like to express my deepest gratitude and sincere thanks to my advisor, Dr. Vincent Holmberg for his advice, guidance, support, and encouragement. I am particularly grateful to him for giving me a lot of freedom in my PhD and for always inspiring me new ideas. His professional and personal guidance has been of fundamental help for my development as an independent researcher.

I would also like to thank my committee members, Professor Pozzo D. Lilo and Professor Quiming Yu for their valuable feedback, suggestions, and guidance in my research. Also special thanks to Professor Brandi Cossairt for serving as a graduate school representative.

I also wish to acknowledge all the collaborators throughout the years. I feel fortunate to have the opportunities to work with many talented scientists. Dr. Sandeep Ghosh, thank you for all your wisdom you shared with me and helping me with my first paper publication. I am also grateful to Professor Daniel Gamelin, Professor Xiaosong Li and their research group. I would especially like to thank Dr. Chad Hoyer and Dr. Hongbin Liu for their hard work in the computational work that

provides important insight into my dissertation. This dissertation would not have been possible without their support.

I also appreciate all of my current and past Holmberg research group members. My sincere thanks to Dr. Elena Pandres, Fahad Alamer, Brittany Bishop, Dr. Grant Williamson, Sabiha Rustam, Nicole Thompson, Yiheng Zhang, Ge Gu, Chih-Wei Hsu, Kevin Lee, Yao-Yu Li, Ziqi Jiang, Srivathsav Venkatesh, and Karlie Davis. It was a great pleasure working with you guys. I am also truly grateful to all my friends for always encouraging me to finish my PhD.

Last but not least, I would like to express my acknowledgement to the financial support that I received through my PhD studies. The work presented in this dissertation was mainly supported by the National Science Foundation (NSF) through the UW Molecular Engineering Materials Center, a Materials Research Science and Engineering Center (DMR-1719797). I also acknowledge that this work was supported by the University of Washington Molecular Engineering Institute, and part of this work was conducted at the Molecular Analysis Facility, which is supported in part by the National Science Foundation (grant ECC-1542101).

DEDICATION

Dedicated to all the people who have had a great impact on this journey

Chapter 1. INTRODUCTION

The interaction of light with subwavelength nanomaterials has historically been an area of great interest in both theoretical science and engineering. Since the pioneering report by Michael Faraday in the middle of the 19th century demonstrating that colloidal gold nanoparticles exhibit a ruby-red color in contrast to bulk gold,[1] the unique optical properties of metallic nanoparticles in particular have been the subject of intense investigation.[2-4] The progression of such intensive research is represented by plasmonics.[4-6] The past several decades have seen immense advances in this field driven by the recent development of the colloidal synthesis of nanomaterials.[5, 7-8]

Noble metal nanoparticles such as gold and silver have attracted considerable attention as an important class of plasmonic nanomaterial due to their unique interaction with light in the visible region via the localized surface plasmon resonance (LSPR).[2-5, 9-10] An LSPR is a collective, coherent oscillation of free charge carriers in a small nanoparticle that occurs in resonance with incident light of a specific wavelength (**Figure 1.1**).[2-5, 9-10] These collective charge density oscillations result in an enhanced electromagnetic field at the nanoparticle surface.[2-5, 9-10] This in turn allows the plasmonic nanoparticles to have a large extinction cross-section and be used to manipulate electric fields to nanoscopic length scales well below the diffraction limit.[11-12]

Another intriguing effect of the excitation of an LSPR is transfer of photon energy to energetic carriers and heat[13-14] through resonant interaction with the incident light.[15-17] Hence, noble metal nanoparticles have been explored for a wide range of applications, including nonlinear optics,[12, 18] sensors,[10, 19-20] photothermal therapy,[14, 21] and photocatalysis.[15-17] However, despite the promise of unprecedented capabilities in noble metal nanocrystals, their applications in optical and plasmonic devices suffer from the high ohmic losses and intrinsically fixed dielectric properties of metals.[22-

[25] As a consequence, there has been a push to develop alternative plasmonic materials over the last few decades.

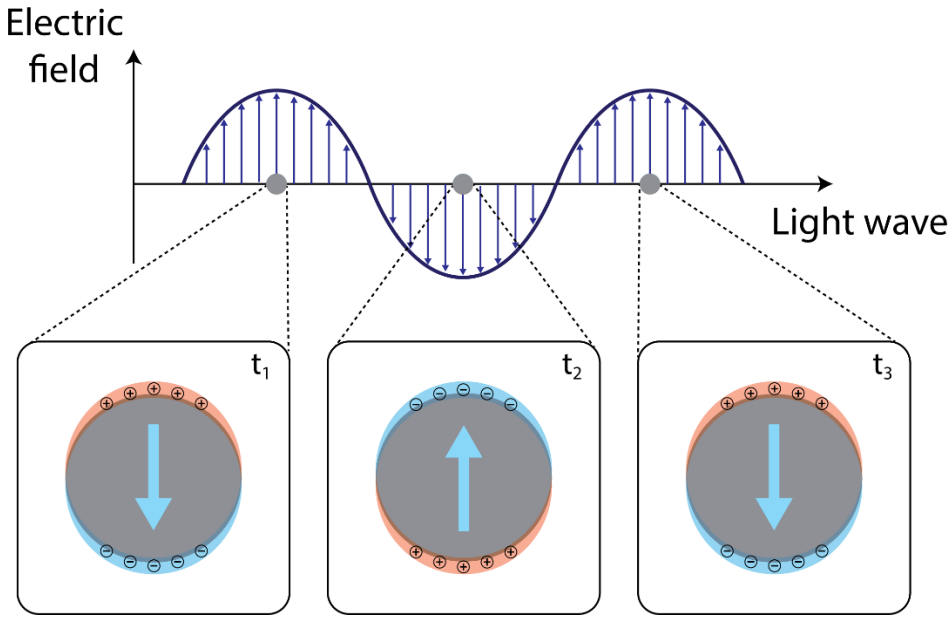

Figure 1.1. Schematic of the excitation of LSPR showing the collective, coherent oscillations of free charge carriers in resonant with the incident light.

LSPRs are commonly observed in noble metal nanostructures due to the resonant interaction of their free electrons with the electromagnetic field of impinging light.[2-5, 9-10] However, the excitation of LSPRs is not exclusively limited to metal nanocrystals, and can also be observed in nonmetallic nanomaterials that possess appreciable free carrier concentrations.[26-28] During the past decade, many studies have demonstrated the plasmonic properties of several types of degenerately doped semiconductor nanocrystals, including copper chalcogenides,[29-32] oxygen-deficient transition metal oxides,[33-34] doped metal oxides,[35-38] and phosphorous or boron-doped silicon nanocrystals.[39-41]

These plasmonic semiconductor nanocrystals have emerged as a new family of plasmonic materials with highly tunable plasmonic properties and have led to significant improvements in

technologies based on plasmonics, including theragnosis,[42-44] sensing,[45-46] and electrochromic smart windows.[47-48]

Moreover, recent studies showed that degenerately doped semiconductor nanoparticles can serve as alternative plasmonic materials to noble metals by mitigating plasmonic losses.[22, 49-50] However, while plasmonic semiconductor nanocrystals are envisioned as an attractive platform for replacing noble metal nanoparticles, their LSPR energy typically lies lower than that of the plasmonic metal NCs due to the characteristics of semiconductors that have much lower carrier density than that of metals.[26-29] So far, a viable replacement for plasmonic metal nanocrystals in the visible spectrum has remained elusive.

In recent years, chalcopyrite copper iron sulfide ($CuFeS_2$) nanocrystals were suggested as another attractive option to replace plasmonic metal nanocrystals.[51] Interestingly, for the case of $CuFeS_2$ nanocrystals, it has been shown that they exhibit strong absorption and scattering of light in the visible region, analogous to the observed plasmonic response in noble metal nanocrystals.[51-53] However, it is important to note that, in contrast to metallic nanocrystals, $CuFeS_2$ is considered as a class of all-dielectric intermediate band gap semiconductor.[51] Therefore, the origin of their optical properties is quite different from that of the LSPR. However, the underlying physics of the strong light absorption and scattering exhibited by $CuFeS_2$ nanocrystals remain poorly understood.

Similar to the way that a complete understanding of the fundamental properties of plasmonic nanocrystals led to the development of a variety of applications, materials research plays an important role in advanced technology. In this perspective, this work aims to explore the resonant interaction of light with ternary metal chalcogenide intermediate band semiconductor nanocrystals.

References

1. Faraday, M., The Bakerian Lecture: Experimental relations of gold (and other metals) to light. *Philosophical Transactions of the Royal Society of London* **1857,** *147*, 145-181.

2. Eustis, S.; El-Sayed, M. A., Why gold nanoparticles are more precious than pretty gold: Noble metal surface plasmon resonance and its enhancement of the radiative and nonradiative properties of nanocrystals of different shapes. *Chemical Society Reviews* **2006,** *35* (3), 209-217.

3. Zhang, J. Z.; Noguez, C., Plasmonic Optical Properties and Applications of Metal Nanostructures. *Plasmonics* **2008,** *3* (4), 127-150.

4. Pelton, M.; Bryant, G. W., *Introduction to Metal-Nanoparticle Plasmonics*. Wiley: 2013.

5. Pelton, M.; Aizpurua, J.; Bryant, G., Metal-nanoparticle plasmonics. *Laser & Photonics Reviews* **2008,** *2* (3), 136-159.

6. Halas, N. J., Plasmonics: An Emerging Field Fostered by Nano Letters. *Nano Letters* **2010,** *10* (10), 3816-3822.

7. Pileni, M. P., Control of the Size and Shape of Inorganic Nanocrystals at Various Scales from Nano to Macrodomains. *The Journal of Physical Chemistry C* **2007,** *111* (26), 9019-9038.

8. Kovalenko, M. V.; Manna, L.; Cabot, A.; Hens, Z.; Talapin, D. V.; Kagan, C. R.; Klimov, V. I.; Rogach, A. L.; Reiss, P.; Milliron, D. J.; Guyot-Sionnnest, P.; Konstantatos, G.; Parak, W. J.; Hyeon, T.; Korgel, B. A.; Murray, C. B.; Heiss, W., Prospects of Nanoscience with Nanocrystals. *ACS Nano* **2015,** *9* (2), 1012-1057.

9. S. L.; El-Sayed, M. A., Optical Properties and Ultrafast Dynamics of Metallic Nanocrystals. *Annual Review of Physical Chemistry* **2003,** *54* (1), 331-366.

10. Mayer, K. M.; Hafner, J. H., Localized Surface Plasmon Resonance Sensors. *Chemical Reviews* **2011,** *111* (6), 3828-3857.

11. Gramotnev, D. K.; Bozhevolnyi, S. I., Plasmonics beyond the diffraction limit. *Nature Photonics* **2010,** *4* (2), 83-91.

12. Schuller, J. A.; Barnard, E. S.; Cai, W.; Jun, Y. C.; White, J. S.; Brongersma, M. L., Plasmonics for extreme light concentration and manipulation. *Nature Materials* **2010,** *9* (3), 193-204.

13. Jauffred, L.; Samadi, A.; Klingberg, H.; Bendix, P. M.; Oddershede, L. B., Plasmonic Heating of Nanostructures. *Chemical Reviews* **2019,** *119* (13), 8087-8130.

14. Baffou, G.; Quidant, R., Thermo-plasmonics: using metallic nanostructures as nano-sources of heat. *Laser & Photonics Reviews* **2013,** *7* (2), 171-187.

15. Brongersma, M. L.; Halas, N. J.; Nordlander, P., Plasmon-induced hot carrier science and technology. *Nature Nanotechnology* **2015,** *10* (1), 25-34.

16. Zhang, X.; Chen, Y. L.; Liu, R.-S.; Tsai, D. P., Plasmonic photocatalysis. *Reports on Progress in Physics* **2013,** *76* (4), 046401.

17. Kale, M. J.; Avanesian, T.; Christopher, P., Direct Photocatalysis by Plasmonic Nanostructures. *ACS Catalysis* **2014,** *4* (1), 116-128.

18. Kauranen, M.; Zayats, A. V., Nonlinear plasmonics. *Nature Photonics* **2012,** *6* (11), 737-748.

19. Brolo, A. G., Plasmonics for future biosensors. *Nature Photonics* **2012,** *6* (11), 709-713.

20. Anker, J. N.; Hall, W. P.; Lyandres, O.; Shah, N. C.; Zhao, J.; Van Duyne, R. P., Biosensing with plasmonic nanosensors. *Nature Materials* **2008,** *7* (6), 442-453.

21. Huang, X.; Jain, P. K.; El-Sayed, I. H.; El-Sayed, M. A., Plasmonic photothermal therapy (PPTT) using gold nanoparticles. *Lasers in Medical Science* **2007,** *23* (3), 217.

22. Naik, G. V.; Shalaev, V. M.; Boltasseva, A., Alternative Plasmonic Materials: Beyond Gold and Silver. *Advanced Materials* **2013,** *25* (24), 3264-3294.

23. Gutiérrez, Y.; Brown, A. S.; Moreno, F.; Losurdo, M., Plasmonics beyond noble metals: Exploiting phase and compositional changes for manipulating plasmonic performance. *Journal of Applied Physics* **2020,** *128* (8), 080901.

24. Ozbay, E., Plasmonics: Merging Photonics and Electronics at Nanoscale Dimensions. *Science* **2006,** *311* (5758), 189-193.

25. Fang, Y.; Sun, M., Nanoplasmonic waveguides: towards applications in integrated nanophotonic circuits. *Light: Science & Applications* **2015,** *4* (6), e294-e294.

26. Comin, A.; Manna, L., New materials for tunable plasmonic colloidal nanocrystals. *Chemical Society Reviews* **2014,** *43* (11), 3957-3975.

27. Kriegel, I.; Scotognella, F.; Manna, L., Plasmonic doped semiconductor nanocrystals: Properties, fabrication, applications and perspectives. *Physics Reports* **2017,** *674*, 1-52.

28. Agrawal, A.; Cho, S. H.; Zandi, O.; Ghosh, S.; Johns, R. W.; Milliron, D. J., Localized Surface Plasmon Resonance in Semiconductor Nanocrystals. *Chemical Reviews* **2018,** *118* (6), 3121-3207.

29. Luther, J. M.; Jain, P. K.; Ewers, T.; Alivisatos, A. P., Localized surface plasmon resonances arising from free carriers in doped quantum dots. *Nature Materials* **2011,** *10* (5), 361-366.

30. Dorfs, D.; Härtling, T.; Miszta, K.; Bigall, N. C.; Kim, M. R.; Genovese, A.; Falqui, A.; Povia, M.; Manna, L., Reversible Tunability of the Near-Infrared Valence Band Plasmon Resonance in $Cu_{2-x}Se$ Nanocrystals. *Journal of the American Chemical Society* **2011,** *133* (29), 11175-11180.

31. Kriegel, I.; Jiang, C.; Rodríguez-Fernández, J.; Schaller, R. D.; Talapin, D. V.; da Como, E.; Feldmann, J., Tuning the Excitonic and Plasmonic Properties of Copper Chalcogenide Nanocrystals. *Journal of the American Chemical Society* **2012,** *134* (3), 1583-1590.

32. Zhao, Y.; Pan, H.; Lou, Y.; Qiu, X.; Zhu, J.; Burda, C., Plasmonic $Cu_{2-x}S$ Nanocrystals: Optical and Structural Properties of Copper-Deficient Copper(I) Sulfides. *Journal of the American Chemical Society* **2009,** *131* (12), 4253-4261.

33. Manthiram, K.; Alivisatos, A. P., Tunable Localized Surface Plasmon Resonances in Tungsten Oxide Nanocrystals. *Journal of the American Chemical Society* **2012,** *134* (9), 3995-3998.

34. Huang, Q.; Hu, S.; Zhuang, J.; Wang, X., MoO_{3-x}-Based Hybrids with Tunable Localized Surface Plasmon Resonances: Chemical Oxidation Driving Transformation from Ultrathin Nanosheets to Nanotubes. *Chemistry – A European Journal* **2012,** *18* (48), 15283-15287.

35. Buonsanti, R.; Llordes, A.; Aloni, S.; Helms, B. A.; Milliron, D. J., Tunable Infrared Absorption and Visible Transparency of Colloidal Aluminum-Doped Zinc Oxide Nanocrystals. *Nano Letters* **2011,** *11* (11), 4706-4710.

36. Kanehara, M.; Koike, H.; Yoshinaga, T.; Teranishi, T., Indium Tin Oxide Nanoparticles with Compositionally Tunable Surface Plasmon Resonance Frequencies in the Near-IR Region. *Journal of the American Chemical Society* **2009,** *131* (49), 17736-17737.

37. Gordon, T. R.; Paik, T.; Klein, D. R.; Naik, G. V.; Caglayan, H.; Boltasseva, A.; Murray, C. B., Shape-Dependent Plasmonic Response and Directed Self-Assembly in a New Semiconductor Building Block, Indium-Doped Cadmium Oxide (ICO). *Nano Letters* **2013,** *13* (6), 2857-2863.

38. Lounis, S. D.; Runnerstrom, E. L.; Llordés, A.; Milliron, D. J., Defect Chemistry and Plasmon Physics of Colloidal Metal Oxide Nanocrystals. *The Journal of Physical Chemistry Letters* **2014,** *5* (9), 1564-1574.

39. Rowe, D. J.; Jeong, J. S.; Mkhoyan, K. A.; Kortshagen, U. R., Phosphorus-Doped Silicon Nanocrystals Exhibiting Mid-Infrared Localized Surface Plasmon Resonance. *Nano Letters* **2013,** *13* (3), 1317-1322.

40. Kramer, N. J.; Schramke, K. S.; Kortshagen, U. R., Plasmonic Properties of Silicon Nanocrystals Doped with Boron and Phosphorus. *Nano Letters* **2015,** *15* (8), 5597-5603.

41. Zhou, S.; Pi, X.; Ni, Z.; Ding, Y.; Jiang, Y.; Jin, C.; Delerue, C.; Yang, D.; Nozaki, T., Comparative Study on the Localized Surface Plasmon Resonance of Boron- and Phosphorus-Doped Silicon Nanocrystals. *ACS Nano* **2015,** *9* (1), 378-386.

42. Hessel, C. M.; Pattani, V. P.; Rasch, M.; Panthani, M. G.; Koo, B.; Tunnell, J. W.; Korgel, B. A., Copper Selenide Nanocrystals for Photothermal Therapy. *Nano Letters* **2011,** *11* (6), 2560-2566.

43. Ding, X.; Liow, C. H.; Zhang, M.; Huang, R.; Li, C.; Shen, H.; Liu, M.; Zou, Y.; Gao, N.; Zhang, Z.; Li, Y.; Wang, Q.; Li, S.; Jiang, J., Surface Plasmon Resonance Enhanced Light Absorption and Photothermal Therapy in the Second Near-Infrared Window. *Journal of the American Chemical Society* **2014,** *136* (44), 15684-15693.

44. Wen, L.; Chen, L.; Zheng, S.; Zeng, J.; Duan, G.; Wang, Y.; Wang, G.; Chai, Z.; Li, Z.; Gao, M., Ultrasmall Biocompatible WO_{3-x} Nanodots for Multi-Modality Imaging and Combined Therapy of Cancers. *Advanced Materials* **2016,** *28* (25), 5072-5079.

45. Kalanur, S. S.; Lee, Y.-A.; Seo, H., Eye-readable gasochromic and optical hydrogen gas sensor based on CuS–Pd. *RSC Advances* **2015,** *5* (12), 9028-9034.

46. Tan, X.; Wang, L.; Cheng, C.; Yan, X.; Shen, B.; Zhang, J., Plasmonic MoO_{3-x}@MoO_3 nanosheets for highly sensitive SERS detection through nanoshell-isolated electromagnetic enhancement. *Chemical Communications* **2016,** *52* (14), 2893-2896.

47. Runnerstrom, E. L.; Llordés, A.; Lounis, S. D.; Milliron, D. J., Nanostructured electrochromic smart windows: traditional materials and NIR-selective plasmonic nanocrystals. *Chemical Communications* **2014,** *50* (73), 10555-10572.

48. Garcia, G.; Buonsanti, R.; Llordes, A.; Runnerstrom, E. L.; Bergerud, A.; Milliron, D. J., Near-Infrared Spectrally Selective Plasmonic Electrochromic Thin Films. *Advanced Optical Materials* **2013,** *1* (3), 215-220.

49. West, P. R.; Ishii, S.; Naik, G. V.; Emani, N. K.; Shalaev, V. M.; Boltasseva, A., Searching for better plasmonic materials. *Laser & Photonics Reviews* **2010,** *4* (6), 795-808.

50. Boltasseva, A.; Atwater, H. A., Low-Loss Plasmonic Metamaterials. *Science* **2011,** *331* (6015), 290-291.

51. Gaspari, R.; Della Valle, G.; Ghosh, S.; Kriegel, I.; Scotognella, F.; Cavalli, A.; Manna, L., Quasi-Static Resonances in the Visible Spectrum from All-Dielectric Intermediate Band Semiconductor Nanocrystals. *Nano Letters* **2017,** *17* (12), 7691-7695.

52. Ghosh, S.; Avellini, T.; Petrelli, A.; Kriegel, I.; Gaspari, R.; Almeida, G.; Bertoni, G.; Cavalli, A.; Scotognella, F.; Pellegrino, T.; Manna, L., Colloidal $CuFeS_2$ Nanocrystals: Intermediate Fe d-Band Leads to High Photothermal Conversion Efficiency. *Chemistry of Materials* **2016,** *28* (13), 4848-4858.

53. Sugathan, A.; Bhattacharyya, B.; Kishore, V. V. R.; Kumar, A.; Rajasekar, G. P.; Sarma, D. D.; Pandey, A., Why Does $CuFeS_2$ Resemble Gold? *The Journal of Physical Chemistry Letters* **2018,** *9* (4), 696-701.

Chapter 2. BACKGROUND KNOWLEDGE

This chapter is dedicated to the theoretical background which is necessary to better understand the work presented in this dissertation. Specifically, we begin with the fundamentals of electromagnetic theory to explore in detail the consequences of this dissertation.

2.1 ELECTROMAGNETIC THEORY

2.1.1 *Maxwell's Equations in Matter*

In the interaction of light with matter, Maxwell's equations are the most obvious starting point because these equations describe the behavior of the electromagnetic field and provide the basis of electromagnetism. In SI units Maxwell's equations for the macroscopic electromagnetic field at interior points in matter, also known as Maxwell's macroscopic equations, are expressed as[1-5]

$$\nabla \cdot \mathbf{D} = \rho_F \tag{2.1}$$

$$\nabla \cdot \mathbf{B} = 0 \tag{2.2}$$

$$\nabla \times \mathbf{E} = -\frac{\partial \boldsymbol{B}}{\partial t} \tag{2.3}$$

$$\nabla \times \mathbf{H} = \frac{\partial \boldsymbol{D}}{\partial t} + \boldsymbol{J_F} \tag{2.4}$$

where **D** is the electric displacement defined in Equation 2.5, ρ_F is the free charge density, **B** is the magnetic induction, **E** is the electric field, **H** is the magnetic field defined in Equation 2.6, and $\boldsymbol{J_F}$ is the free current density.

$$\mathbf{D} = \varepsilon_0 \mathbf{E} + \mathbf{P} \tag{2.5}$$

$$\mathbf{H} = \frac{1}{\mu_0}\mathbf{B} - \mathbf{M} \tag{2.6}$$

where ε_0 is the permittivity of free space, **P** is the electric polarization, μ_0 is the permeability of free space, and **M** is the magnetization.

As listed in Equations 2.1 – 2.4, Maxwell's macroscopic equations relate the four fields **D** (the electric displacement), **B** (the magnetic induction), **E** (the electric field), and **H** (the magnetic field) with the free charge carrier density and current density.[1-5] However, these equations are not sufficient in and of themselves to apply Maxwell's macroscopic equations to fully describe a materials interaction with the electric and magnetic fields of an electromagnetic wave in space-time.[1-5] It is therefore necessary to introduce the so-called constitutive relations, which describe the response of matter under the influence of the fields. Let us consider a linear, homogeneous, and isotropic medium for simplicity. In that case, the constitutive relations are given by[1-5]

$$\mathbf{D} = \varepsilon_0 \varepsilon_r \mathbf{E} = \varepsilon \mathbf{E} \tag{2.7}$$

$$\mathbf{B} = \mu_0 \mu_r \mathbf{H} = \mu \mathbf{H} \tag{2.8}$$

$$\boldsymbol{J_F} = \sigma \mathbf{E} \tag{2.9}$$

where ε_r is the relative permittivity or dielectric constant, ε is the permittivity, μ_r is the relative permeability, μ is the permeability, and σ is the conductivity. Using the above relations, we can now further link the electric displacement to the electric field and the magnetic field to the magnetic induction via the permittivity (ε) and permeability (μ). Moreover, it can be seen that the propagation of the wave through a medium is dictated by the permittivity, permeability, and conductivity of the material.

In any medium other than a vacuum, the permittivity and permeability are affected by the polarization properties of the material. Thus, the electromagnetic response of matter can also be described using the electric and magnetic susceptibilities χ_e and χ_m, which relate the electric polarization to the electric field and the magnetization to the magnetic field, respectively. For linear materials, the electric polarization and magnetization are given by[1-5]

$$\mathbf{P} = \varepsilon_0 \chi_e \mathbf{E} \tag{2.10}$$

$$\mathbf{M} = \chi_m \mathbf{H} \tag{2.11}$$

By substituting the above equations into the definition of Equation 2.5 and 2.6 we have

$$\mathbf{D} = \varepsilon_0 \mathbf{E} + \mathbf{P} = \varepsilon_0 \mathbf{E} + \varepsilon_0 \chi_e \mathbf{E} = \varepsilon_0 (1 + \chi_e) \mathbf{E} \tag{2.12}$$

$$\mathbf{B} = \mu_0 (\mathbf{H} + \mathbf{M}) = \mu_0 (\mathbf{H} + \chi_m \mathbf{H}) = \mu_0 (1 + \chi_m) \mathbf{H} \tag{2.13}$$

Then, using the first two constitutive relations 2.7 and 2.8, we can find that the permittivity and permeability are related to the electric and magnetic susceptibilities as follows

$$\mathbf{D} = \varepsilon_0 (1 + \chi_e) \mathbf{E} = \varepsilon_0 \varepsilon_r \mathbf{E} = \varepsilon \mathbf{E} \tag{2.14}$$

$$\mathbf{B} = \mu_0 (1 + \chi_m) \mathbf{H} = \mu_0 \mu_r \mathbf{H} = \mu \mathbf{H} \tag{2.15}$$

Finally, we can derive the relation between the relative permittivity and electric susceptibility as well as the relative permeability and magnetic susceptibility.

$$\varepsilon_r = (1 + \chi_e) \tag{2.16}$$

$$\mu_r = (1 + \chi_m) \tag{2.17}$$

The above equations show that the electric and magnetic susceptibilities are directly related to the permittivity and permeability of the material and thus influence the interaction of light with matter. This in turn means that we can make a prediction of the optical and magnetic properties of materials if we know the electric and magnetic susceptibilities, or the permittivity and permeability.

2.1.2 *Wave Equation*

One of the significant achievements of Maxwell's equations is the prediction of the electromagnetic wave phenomenon. Based on Maxwell's equations, understanding electromagnetic wave propagation in a medium can be provided by a set of partial differential equations.[5-6] To see this, let us consider a homogeneous, linear, and isotropic medium, in which the permittivity ε and permeability μ are constant over the entire medium, independent of the

magnitudes and directions of the electric and magnetic fields. Now, assuming that there are no free charges (i.e. $\boldsymbol{J_F} = 0$), then with constitutive relations, Maxwell's equations are given as[5-6]

$$\nabla \cdot \mathbf{E} = 0 \tag{2.18}$$

$$\nabla \cdot \mathbf{H} = 0 \tag{2.19}$$

$$\nabla \times \mathbf{E} = -\mu \frac{\partial \mathbf{H}}{\partial t} \tag{2.20}$$

$$\nabla \times \mathbf{H} = \varepsilon \frac{\partial \mathbf{E}}{\partial t} + \sigma \mathbf{E} \tag{2.21}$$

Taking the curl of both sides of Equation 2.20 and 2.21, we have

$$\nabla \times (\nabla \times \mathbf{E}) = \nabla \times \left(-\mu \frac{\partial \mathbf{H}}{\partial t}\right) = -\varepsilon\mu \frac{\partial^2 \mathbf{E}}{\partial t^2} - \sigma\mu \frac{\partial \mathbf{E}}{\partial t} \tag{2.22}$$

$$\nabla \times (\nabla \times \mathbf{H}) = \nabla \times \left(\varepsilon \frac{\partial \mathbf{E}}{\partial t} + \sigma \mathbf{E}\right) = -\varepsilon\mu \frac{\partial^2 \mathbf{H}}{\partial t^2} - \sigma\mu \frac{\partial \mathbf{H}}{\partial t} \tag{2.23}$$

Then, using the vector identity, $\nabla \times \nabla \times \vec{A} = \nabla\left(\nabla \cdot \vec{A}\right) - \nabla \cdot \left(\nabla \vec{A}\right)$, we can rewrite Equation 2.22 and 2.23 as

$$\nabla^2 \mathbf{E} = \varepsilon\mu \frac{\partial^2 \mathbf{E}}{\partial t^2} + \sigma\mu \frac{\partial \mathbf{E}}{\partial t} \tag{2.24}$$

$$\nabla^2 \mathbf{H} = \varepsilon\mu \frac{\partial^2 \mathbf{H}}{\partial t^2} + \sigma\mu \frac{\partial \mathbf{H}}{\partial t} \tag{2.25}$$

The above is known as the homogeneous equations for damped wave motion. To see the simplest form of wave equation, we may further assume the propagation of electromagnetic waves in nondissipative media where $\sigma = 0$. Then, the homogeneous equation for an undamped wave results[5-6]

$$\nabla^2 \mathbf{E} - \mu\varepsilon \frac{\partial^2 \mathbf{E}}{\partial t^2} = 0 \tag{2.26}$$

$$\nabla^2 \mathbf{H} - \mu\varepsilon \frac{\partial^2 \mathbf{H}}{\partial t^2} = 0 \tag{2.27}$$

which shows that the wave propagates in the media at speed v

$$\mathrm{v} = \frac{1}{\sqrt{\varepsilon\mu}} = \frac{c}{n} \tag{2.28}$$

where c is the speed of light in vacuum and n is the refractive index of material.

2.1.3 *Poynting's Theorem*

In electrodynamics, Poynting's theorem is of fundamental significance and represents the conservation of energy for electromagnetic fields. According to the Poynting's theorem, energy conservation in electromagnetic phenomena can be deduced as a general integral of the field equations.[1, 7-9] Starting from two curl equations of Maxwell's equations and applying some mathematical manipulations, we have

$$\mathbf{H} \cdot (\nabla \times \mathbf{E}) - \mathbf{E} \cdot (\nabla \times \mathbf{H}) = -\mathbf{H} \cdot \frac{\partial \mathbf{B}}{\partial t} - \mathbf{E} \cdot \frac{\partial \mathbf{D}}{\partial t} - \mathbf{E} \cdot \boldsymbol{J_F} \tag{2.29}$$

Then, using the vector identity, $\nabla \cdot (\vec{A} \times \vec{B}) = \vec{B} \cdot (\nabla \times \vec{A}) - \vec{A} \cdot (\nabla \times \vec{B})$, we can rewrite the terms on the left-hand side of Equation 2.29

$$\nabla \cdot (\mathbf{E} \times \mathbf{H}) = -\mathbf{H} \cdot \frac{\partial \mathbf{B}}{\partial t} - \mathbf{E} \cdot \frac{\partial \mathbf{D}}{\partial t} - \mathbf{E} \cdot \boldsymbol{J_F} \tag{2.30}$$

In a simple medium, in which the permittivity ε, permeability μ, and conductivity σ are constant, we find

$$\mathbf{H} \cdot \frac{\partial \mathbf{B}}{\partial t} = \mathbf{H} \cdot \frac{\partial (\mu \mathbf{H})}{\partial t} = \frac{1}{2} \frac{\partial (\mu \mathbf{H} \cdot \mathbf{H})}{\partial t} = \frac{\partial}{\partial t} \left(\frac{1}{2} \mu \mathbf{H}^2\right) \tag{2.31}$$

$$\mathbf{E} \cdot \frac{\partial \mathbf{D}}{\partial t} = \mathbf{E} \cdot \frac{\partial (\varepsilon \mathbf{E})}{\partial t} = \frac{1}{2} \frac{\partial (\varepsilon \mathbf{E} \cdot \mathbf{E})}{\partial t} = \frac{\partial}{\partial t} \left(\frac{1}{2} \varepsilon \mathbf{E}^2\right) \tag{2.32}$$

$$\mathbf{E} \cdot \boldsymbol{J_F} = \mathbf{E} \cdot (\sigma \mathbf{E}) = \sigma \mathbf{E}^2 \tag{2.33}$$

Equation 2.30 can then be written as

$$\nabla \cdot (\mathbf{E} \times \mathbf{H}) = -\frac{\partial}{\partial t} \left(\frac{1}{2} \mu \mathbf{H}^2 + \frac{1}{2} \varepsilon \mathbf{E}^2\right) - \sigma \mathbf{E}^2 \tag{2.34}$$

Finally, upon integrating both sides of Equation 2.34 over a volume V, and applying the divergence theorem, the result is

$$\oint_s \ (\mathbf{E} \times \mathbf{H}) \cdot ds = -\frac{\partial}{\partial t} \int_{\mathrm{V}} \left(\frac{1}{2} \mu \mathbf{H}^2 + \frac{1}{2} \varepsilon \mathbf{E}^2\right) d\mathrm{V} - \int_{\mathrm{V}} \ \sigma \mathbf{E}^2 \, d\mathrm{V} \tag{2.35}$$

The above equation is referred to as the Poynting's theorem. Note that the factor $\mathbf{E} \times \mathbf{H}$ is called the Poynting vector, which describes the magnitude and direction of the rate of transfer of electromagnetic energy at all points of space.[1, 7-9] Herein, each of the terms on the right-hand side of Equation 2.35 has a physical significance. The first term on the right side represents the rate of changes of the electric and magnetic energies stored in the volume and the second term on the right side refers to the ohmic power dissipated in the volume.[1, 7-9] Accordingly, Poynting's theorem states that the flow of electromagnetic energy across a control boundary of the region accounts for the ohmic power loss in the volume and the rate of change of energy in the electromagnetic field within the volume.[1, 7-9]

2.2 Drude-Lorentz Model for Dielectric Function of a Material

The optical response of a material can be understood using its characteristic optical properties by means of the complex dielectric function ($\varepsilon = \varepsilon' + i\varepsilon''$), also known as relative permittivity.[2-3, 10-11] Note that this parameter is often called "dielectric constant", however, it is actually not a fixed value over the electromagnetic spectrum. In the microscopic point of view, the dielectric function of a material represents the polarizability of atoms and molecules in a material to an externally applied electromagnetic field, which can account for a qualitative understanding of the origins and underlying physics of LSPRs in plasmonic nanocrystals.[3, 10-13] Therefore, it is important to explore how the complex dielectric function of a material changes as a function of the frequency of the applied field.

2.2.1 *Lorentz Oscillator Model*

Let us begin with a classical description of the Lorentz oscillator model to derive the frequency-dependent dielectric function of a dielectric material. According to the Lorentz model, an electron is treated as being bound to the positively charged ion as a damped harmonic oscillator system subject to the driving force of an applied electromagnetic field.[2-3, 11-12] Assuming that the electric field of an electromagnetic wave has a harmonic time dependence, and the magnetic field contribution could be neglected. Then the electron's equation of motion in the presence of an external electric field **E**(t), analogous to the motion of a spring-mass system, can be written as[2-3, 11-12]

$$m_e\ddot{\boldsymbol{r}} + m_e\gamma\dot{\boldsymbol{r}} + m_e\omega_0^2\boldsymbol{r} = e\mathbf{E}(t) \tag{2.36}$$

where m_e is the electron mass, γ is the damping constant, ω_0 is the natural frequency of oscillation of the electron, r is the displacement of the oscillator, and e is the electron charge. By considering the time-dependence of a harmonic electric field ($\mathbf{E}(t) = \mathbf{E}(\omega)e^{-i\omega t}$), the functional form of the solution is then given by

$$\boldsymbol{r}(t) = \boldsymbol{r}(\omega)e^{-i\omega t} \tag{2.37}$$

Plugging this into Equation 2.36 gives

$$\boldsymbol{r}(\omega) = \frac{e}{m_e}\frac{1}{(\omega_0^2-\omega^2-i\gamma\omega)}\mathbf{E}(\omega) \tag{2.38}$$

Moreover, since each displacement of an electron results in a dipole moment that contributes to the macroscopic polarization (**P**), which is defined as the average electric dipole moment per unit volume of the medium, the microscopic dipole moment (***p***) can be connected to the polarization with a carrier density (n) as follows[11-13]

$$\mathbf{P} = n \cdot \boldsymbol{p} = n \cdot (e \cdot \boldsymbol{r}) \tag{2.39}$$

Then, the polarization can be expressed as

$$\mathbf{P}(\omega) = \frac{ne^2}{m_e}\frac{1}{(\omega_0^2-\omega^2-i\gamma\omega)}\mathbf{E}(\omega) = \frac{\omega_p^2}{(\omega_0^2-\omega^2-i\gamma\omega)}\varepsilon_0\mathbf{E}(\omega) \quad (2.40)$$

where ω_p is the plasma frequency, which is defined below:

$$\omega_p = \sqrt{\frac{ne^2}{\varepsilon_0 m_e}} \quad (2.41)$$

Recalling that for linear materials the polarization is related to the electric field by $\mathbf{P} = \varepsilon_0\chi_e\mathbf{E}$, we therefore get the frequency-dependent susceptibility

$$\chi_e(\omega) = \frac{\omega_p^2}{(\omega_0^2-\omega^2-i\gamma\omega)} \quad (2.42)$$

Finally, with the relation between the electric susceptibility and the dielectric function (Equation 2.16), we obtain the corresponding frequency-dependent dielectric function[2-3, 10-13]

$$\varepsilon(\omega) = 1 + \chi_e = 1 + \frac{\omega_p^2}{(\omega_0^2-\omega^2-i\gamma\omega)} \quad (2.43)$$

Which can be further separated into its real, ε', and imaginary, ε'', components of the complex dielectric function as follows

$$\varepsilon'(\omega) = 1 + \frac{\omega_p^2}{(\omega_0^2-\omega^2-i\gamma\omega)} \quad (2.44)$$

$$\varepsilon''(\omega) = \frac{\omega_p^2}{(\omega_0^2-\omega^2-i\gamma\omega)} \quad (2.45)$$

2.2.2 *Drude Model*

In contrast to dielectric materials, the optical properties of metals are mainly dominated by the contribution of their loosely bound conduction band electrons, which behave as a free electron gas.[2-4, 10-13] In 1900, Paul Drude proposed a model that the kinetic theory of gases can be applied to understanding the transport and optical properties of electrons in metals.[14] Since these electrons can be considered to move nearly freely in between collisions with unspecified collision centers

(*e.g.*, other electrons, lattice ions, and defects), the response of a metal to an external electric field can be described by the specific case of the Lorentz oscillator model without having a restoring force, that is, by setting the resonator restoring force equal to zero ($\omega_0 = 0$) in Equation 2.36.[2-4, 10-13] Then, the dielectric function of free electrons can be derived as

$$\varepsilon(\omega) = 1 - \frac{\omega_p^2}{\omega^2 + i\gamma\omega} \tag{2.46}$$

Note that the damping parameter (γ) represents the bulk collision frequency of the carriers in this case, which is given by the inverse of the mean electron collision time, τ, *i.e.* $\gamma = 1/\tau$.[2-4] For a small particle with a size comparable to the mean free path of the electrons, the Drude damping parameter is needed to take account of the electron-surface scattering, which becomes dominant in the nanoscale regime. Thus, the modified damping parameter is given as[13, 15-16]

$$\gamma(r) = \gamma_0 + \frac{Av_F}{r} \tag{2.47}$$

where γ_0 is the bulk damping constant, A is a theory-dependent constant that includes details of the scattering process, and v_F is the velocity of the electrons at the Fermi energy.

Despite its drastic assumptions, the Drude model has been found to provide reasonable prediction for the dielectric function of many metals such as aluminum and alkali metals.[2, 11] However, this model neglects electrons in the valence band, thereby not accurately describing the dielectric function of the noble metals like gold and silver at photon energies higher than the interband transition threshold. To account for a substantial bound electron component, the modified Drude dielectric function that includes the contributions of bound electrons, ($\varepsilon = \varepsilon_{free} + \varepsilon_{bound}$), is required.[2, 4, 10-11, 17] Therefore, using the Drude and Lorentz models together, we have

$$\varepsilon(\omega) = 1 - \frac{\omega_p^2}{\omega^2 + i\gamma\omega} + \sum \frac{\omega_{pj}^2}{\omega_j^2 - \omega^2 - i\gamma_j\omega} \tag{2.48}$$

Note that an extension of the Drude-Lorentz model to more than one oscillator is used for better description of the dielectric function.

2.3 Optical Properties of Metal Nanoparticles

Noble metals such as gold and silver have been recognized as a valuable resource for a very long time in their aesthetic aspect due to their shine and lustrous look. However, when the physical dimensions of metals are reduced to the nanometer regime, their optical properties are significantly different from those of the bulk material.[18] This interesting phenomenon has been of great interest to scientists for centuries. The first scientific report on the changes of their optical properties is the ruby color of colloidal gold synthesized by Michael Faraday in 1857.[19] Since that time, quantitative and qualitative studies in the optical properties of metal nanoparticles have accelerated dramatically.[20-21] Consequently, it turns out that the physical origin of the unique optical properties of metal nanoparticles is the coherent oscillation of the conduction band electrons induced by the interacting electromagnetic field.[2, 11, 13] These collective, coherent oscillation of the electrons in resonance with the incident light in a metallic nanoparticle is called the localized surface plasmon resonance (LSPR) and dominates the optical response of the metal nanoparticle.[2-4]

2.3.1 *Resonant Condition for Observing LSPR Excitation*

In 1908, Gustav Mie first developed an analytical solution to the Maxwell's equations for a homogeneous sphere of arbitrary radius illuminated by a plane electromagnetic wave in order to explain the varied color of colloidal gold and its size dependency.[21] However, the Mie solution to Maxwell's equations take the form of an infinite series of spherical multipole partial waves, which

is a complicated mathematical function and therefore a difficult model with which to intepret the LSPR properties of metal nanoparticles.[2-3, 11] To account for the LSPR condition, let us consider a homogeneous sphere of a radius much smaller than the wavelength ($r << \lambda$) for simplicity. In this case, the electric field of the light can be taken to be constant, and it is possible to employ the so-called quasi-static approximation, where the interaction is governed by electrostatics rather than electrodynamics.[2-4, 12-13] Then, the light scattering by a sphere can be addressed by solving the Laplace equation for the potential, $\nabla^2\Phi = 0$, which is much easier to solve.

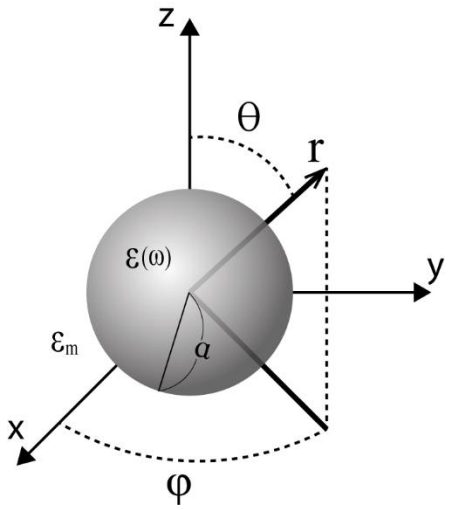

Figure 2.1. Sketch of a homogeneous sphere in spherical coordinates

Taking into account the geometry of our problem, the use of spherical coordinates is convenient to solve the equation. As shown in **Figure 2.1**, consider a homogeneous sphere with radius a and dielectric function $\varepsilon(\omega)$, surrounded by a medium of permittivity ε_m and placed in a uniform static electric field $\mathbf{E} = E_0\hat{z}$. Since the problem possesses azimuthal symmetry, the general solution of the Laplace equation is of the form[2-4, 12-13]

$$\Phi(r,\theta) = \sum_{l=0}^{\infty}[A_l r^l + B_l r^{-l-1}]P_l(\cos\theta) \qquad (2.49)$$

Where $P_l(\cos\theta)$ are the Legendre Polynomials of order l, A_l and B_l are constants to be determined using the boundary conditions, and θ is the angle between the position vector r at point P and the z-axis. Moreover, due to the requirement that the potentials must remain finite at the origin, the solution for the potentials inside and outside the sphere can be written as[2-4, 12-13]

$$\Phi_{in}(r,\theta) = \sum_{l=0}^{\infty} A_l r^l P_l(\cos\theta) \tag{2.50}$$

$$\Phi_{out}(r,\theta) = \sum_{l=0}^{\infty} [B_l r^l + C_l r^{-l-1}] P_l(\cos\theta) \tag{2.51}$$

Now, considering the boundary conditions that are satisfied far away from the sphere ($r \to \infty$) and at the sphere surface ($r = a$), we can determine the coefficients A_l, B_l, and C_l. As for $r \to \infty$, there is no significant field distortion by the effect of the sphere.[2-4, 12-13] Thus, we must have $\Phi_{out} \to -E_0 z = -E_0 r cos\theta$ in Equation 2.51, which demands that $B_1 = -E_0$ and $B_l = 0$ for $l \neq 1$. Moreover, applying the remaining boundary conditions at the sphere surface, that use equality of the tangential components of the electric field and equality of the normal components of the displacement field

$$-\frac{1}{a}\frac{\partial \Phi_{in}}{\partial \theta}\Big|_{r=a} = -\frac{1}{a}\frac{\partial \Phi_{out}}{\partial \theta}\Big|_{r=a} \tag{2.52}$$

$$-\varepsilon_0 \varepsilon \frac{\partial \Phi_{in}}{\partial r}\Big|_{r=a} = -\varepsilon_0 \varepsilon_m \frac{\partial \Phi_{out}}{\partial r}\Big|_{r=a} \tag{2.53}$$

yielding

$$A_1 a = -E_0 a + C_1 a^{-2} \tag{2.54}$$

$$\varepsilon A_1 = -\varepsilon_m E_0 - 2\varepsilon_m C_1 a^{-3} \tag{2.55}$$

and $A_l = C_l = 0$ for $l \neq 1$. This finally leads to the coefficients:

$$A_1 = -\frac{3\varepsilon_m}{\varepsilon + 2\varepsilon_m} E_0 \tag{2.56}$$

$$B_1 = E_0 \tag{2.57}$$

$$C_1 = \frac{\varepsilon - \varepsilon_m}{\varepsilon + 2\varepsilon_m} E_0 a^3 \tag{2.58}$$

Therefore, the potentials inside and outside the sphere can be written as[2-4, 12-13]

$$\Phi_{in} = -\frac{3\varepsilon_m}{\varepsilon+2\varepsilon_m} E_0 r\, cos\theta \tag{2.59}$$

$$\Phi_{out} = -E_0 r\, cos\theta + \frac{\varepsilon-\varepsilon_m}{\varepsilon+2\varepsilon_m} E_0 a^3 \frac{cos\theta}{r^2} \tag{2.60}$$

From the above equation, it can be seen that the potential diverges to infinity when $\varepsilon + 2\varepsilon_m$ approaches zero at certain frequencies, which implies that the fields are resonantly enhanced. In fact, this response is considered as that of a dipole resonance induced by an externally applied electric field, which can be represented as an LSPR for metal nanoparticles.[2-4, 12-13] Generally, however, this resonant condition cannot be fulfilled exactly because ε_m is typically real and positive, whereas $\varepsilon(\omega)$ has a nonzero imaginary part ($Im[\varepsilon(\omega)] \neq 0$). Thus, the resonance condition is simplified to the so-called Fröhlich condition[2-4, 12-13]

$$Re[\varepsilon(\omega)] = -2\varepsilon_m \tag{2.61}$$

Here it is also instructive to examine the distribution of the electric field. Since the electric field is given by the negative gradient of the potential ($\mathbf{E} = -\nabla\Phi$), the resulting electric field can be expressed as[2-4, 12-13]

$$\mathbf{E}_{in} = -\frac{3\varepsilon_m}{\varepsilon+2\varepsilon_m} E_0 \hat{k} \tag{2.62}$$

$$\mathbf{E}_{out} = E_0 \hat{k} + \frac{\varepsilon-\varepsilon_m}{\varepsilon+2\varepsilon_m} \frac{E_0 a^3}{r^3} (2cos\theta \hat{r} + sin\theta \hat{\theta}) \tag{2.63}$$

Where $\hat{k} = cos\theta \hat{r} - sin\theta \hat{\theta}$ is used. Note that the second term of Equation 2.63 shows a similar form to the electric field of a perfect dipole.[2-4, 12-13] Indeed, we can rewrite the potential outside the sphere by introducing the dipole moment $\boldsymbol{p}$

$$\Phi_{out} = -E_0 r\, cos\theta + \frac{\boldsymbol{p} cos\theta}{4\pi\varepsilon_0\varepsilon_m r^2} \tag{2.64}$$

where

$$\boldsymbol{p} = 4\pi\varepsilon_0\varepsilon_m a^3 \frac{\varepsilon-\varepsilon_m}{\varepsilon+2\varepsilon_m} E_0\hat{k} \quad (2.65)$$

Comparing the potential outside the sphere with the potential due to an ideal dipole aligned along the z axis ($\Phi_{dip} = \frac{\boldsymbol{p}\cdot\hat{r}}{4\pi\varepsilon_m r^3} = \frac{\boldsymbol{p}\cos\theta}{4\pi\varepsilon_m r^2}$), we can see that Φ_{out} represents the superposition of the applied field and that of a dipole located at the origin.[2-4, 12-13] Thus, we may conclude that the applied field induces a dipole moment inside the sphere of magnitude proportional to $|\boldsymbol{E_0}|$.

From the above derivation, we can also connect the dielectric function with the polarizability, which can be used to calculate the extinction cross section of a small sphere under the quasi-static approximation. If we introduce the polarizability α, defined via $\boldsymbol{p} = \varepsilon_0\varepsilon_m\alpha\boldsymbol{E_0}$, then we have[2-4, 12-13]

$$\alpha = 4\pi a^3 \frac{\varepsilon-\varepsilon_m}{\varepsilon+2\varepsilon_m} \quad (2.66)$$

As expected, it can also be seen that the polarizability would be maximized at the Fröhlich resonance condition.

2.3.2 *Plasmonic properties of metal nanoparticles*

Above, it is shown that an applied electric field to a small sphere under the quasi-static approximation can induce an oscillating dipole when the resonant condition is met. In principle, the induced dipole moment or polarizability that we introduced in the preceding section describes the response of a sphere to incident light.[2-3, 11, 13] However, these quantities are not usually observable in the actual experiments. Therefore, it is useful to introduce the so-called extinction cross section (C_{ext}), which quantifies how much the irradiance of electromagnetic waves incident on an object loses its intensity by a sum of scattering and absorption cross sections.[2-3, 11, 13] Since the scattering and absorption cross sections are a measure for the probability of energy dissipation

processes by scattering and absorption, they can be defined as the ratio of the scattering and absorption rate of the object to the energy density of the incident wave, respectively.[2-3, 11, 13]

$$C_{sca} = \frac{W_{sca}}{I_0},\ C_{abs} = \frac{W_{abs}}{I_0} \tag{2.67}$$

where W_{sca} is the scattered energy rate, W_{abs} is the absorbed energy rate, and I_0 is the energy flux density of the incident light. Thus, we can calculate the absorption and scattering cross sections by analysis of the Poynting vector and integration over all angles. Finally, the cross sections for scattering and absorption by a sphere in the electrostatic approximations are given by[2, 4, 13]

$$C_{sca} = \frac{128\pi^5}{3}\frac{a^6}{\lambda^4}\left|\frac{\varepsilon-\varepsilon_m}{\varepsilon+2\varepsilon_m}\right|^2 = \frac{k^4}{6\pi}|\alpha|^2 \tag{2.68}$$

$$C_{abs} = 8\pi^2\frac{a^3}{\lambda}Im\left\{\frac{\varepsilon-\varepsilon_m}{\varepsilon+2\varepsilon_m}\right\} = kIm\{\alpha\} \tag{2.69}$$

where k is the wavevector in the medium. From the equations above, it is clear that both absorption and scattering are greatly enhanced when the Fröhlich resonance condition is met, either through excitation of an LSPR or other means. Having obtained the expressions for the scattering and absorption cross sections of a sphere in the quasi-static approximation, the basic features of plasmonic properties could be understood. In the following, we will discuss the effects of size, shape, and dielectric medium surrounding the plasmonic nanoparticles on the LSPR for a deeper insight into the optical properties of metallic nanocrystals.

2.3.2.1 Effect of Nanoparticle Size on the LSPR

The plasmonic properties of metal nanoparticles are strongly dependent on the size, shape, and ambient medium.[4, 13, 22-23] **Figure 2.2** shows the extinction spectra of various sizes of gold nanoparticles with diameters of 9, 22, 48, and 99 nm.[22] As shown in **Figure 2.2**, the nanoparticle size has a direct impact on the changes of position and width of LSPR peak because of two main

factors. Firstly, for the larger particles (>25 nm for gold particles) where the quasi-static approximation breaks down, an increase in the size results in a red-shift and broadening of the plasmon band due to so-called retardation effects.[22-24] Moreover, as the particle size continues to increase, higher order oscillation modes that contribute to additional extinction peaks can appear and become dominant (not shown here) since the carriers are no longer homogeneously polarized by the electric field of light.[22-24] Secondly, a noticeable size effect emerges as the nanoparticle size becomes much smaller than the mean free path length of the carriers due to an additional damping process by electron-surface scattering.[15-16, 22] This introduces a size dependence damping term in the Drude formula for the dielectric function of the material, as discussed in the previous section. Therefore, the LSPR band is broadened and blue-shifted with decreasing particle size.

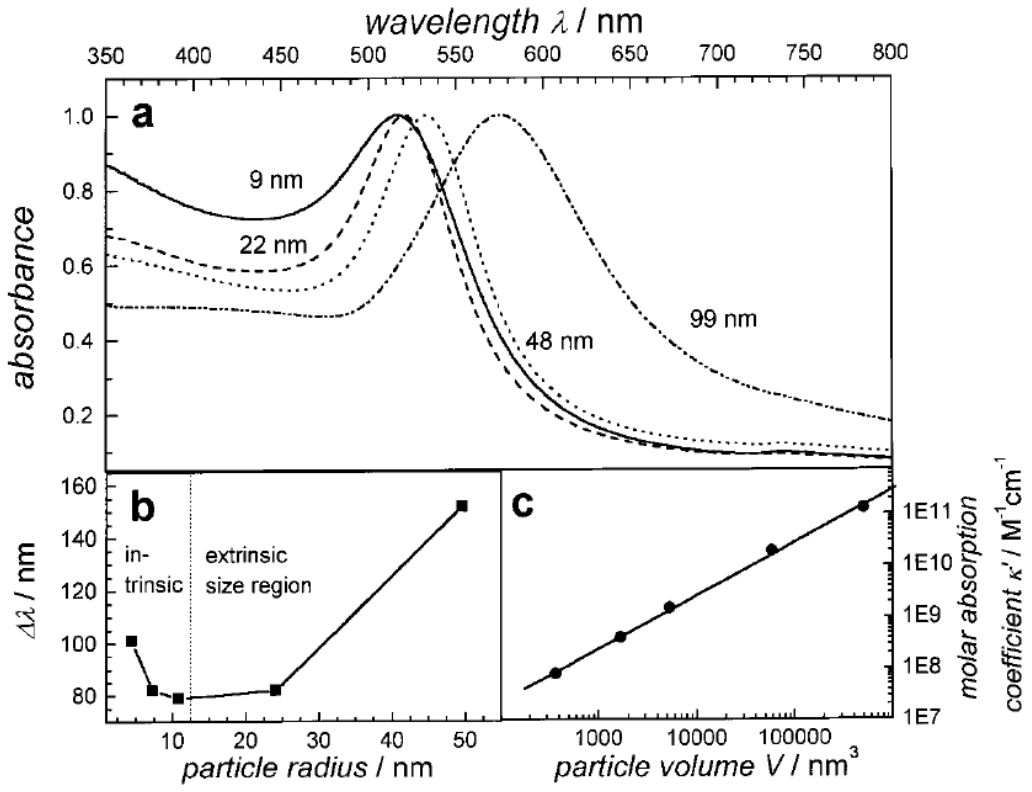

Figure 2.2. Effects of the nanoparticle size on the LSPR in colloidal solutions of gold nanoparticles. (a) Extinction spectra for spherical gold nanoparticles of various sizes in water, (b)

variation of the LSPR bandwidth against the size of the gold nanoparticles, and (c) Dependence of the extinction coefficients of gold nanoparticles on their volume. Reprinted with permission from Reference 22. Copyright (1999) American Chemical Society.

2.3.2.2 Effect of Nanoparticle Shape on the LSPR

So far, we have considered a spherical particle due to the high symmetry that the excitation of LSPR is independent of the polarization direction of the incident light. However, as the spherical symmetry is broken, light polarization plays an important role in the LSPR properties. The most common example of this is rod-shaped metal nanoparticles that generally have two plasmon resonance modes for light polarized longitudinally and transversely along the long- and short-axis of the nanorod, respectively.[22-23, 25-27] **Figure 2.3** illustrates that the shape of metal nanostructures can dramatically affect their plasmonic properties. Particularly, it has been shown that the longitudinal resonance is considerably red-shifted and depends strongly on the gold nanorod aspect ratio, whereas the transverse resonance lies close to the observed LSPR peak for spherical seed particles (~520 nm).[22, 25]

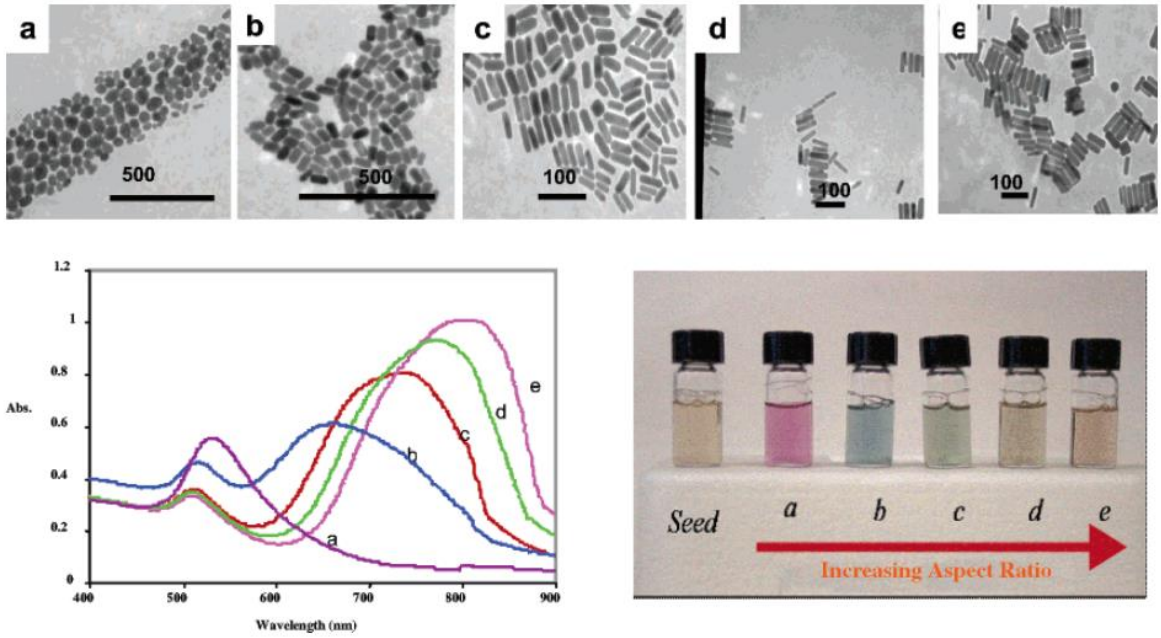

Figure 2.3. Shape dependence of the LSPR. Top panel: Transmission electron microscopy (TEM) images of gold nanorods of various aspect ratios. Aspect ratio = 1.35 ± 0.32, 1.95 ± 0.34, 3.06 ± 0.28, 3.50 ± 0.29, and 4.42 ± 0.23 (From a-e). Bottom panel: Representative extinction spectra (left) and photographs (right) of colloidal gold nanorods with different aspect ratios. Reprinted with permission from Reference 25. Copyright (2005) American Chemical Society.

2.3.2.3 Effect of Surrounding Medium on the LSPR

Besides the nanoparticle size and shape, changing the ambient medium around plasmonic nanoparticles can also have an impact on their plasmonic properties.[23, 28-29] **Figure 2.4** shows the influence of the surrounding medium on the LSPR peak position of gold nanoparticles that a red-shift in LSPR peak position is observed with increasing refractive index of the solvent.[28] The observed red-shifting of the LSPR can be explained by changes in the Fröhlich condition, as discussed in Section 2.3.1.[23, 28-29] Intuitively, this also can be understood by recognizing that an

increase in the dielectric constant of the medium results in a reduced Coulombic restoring force of the carriers, thus leading to a decrease of the resonance frequency.

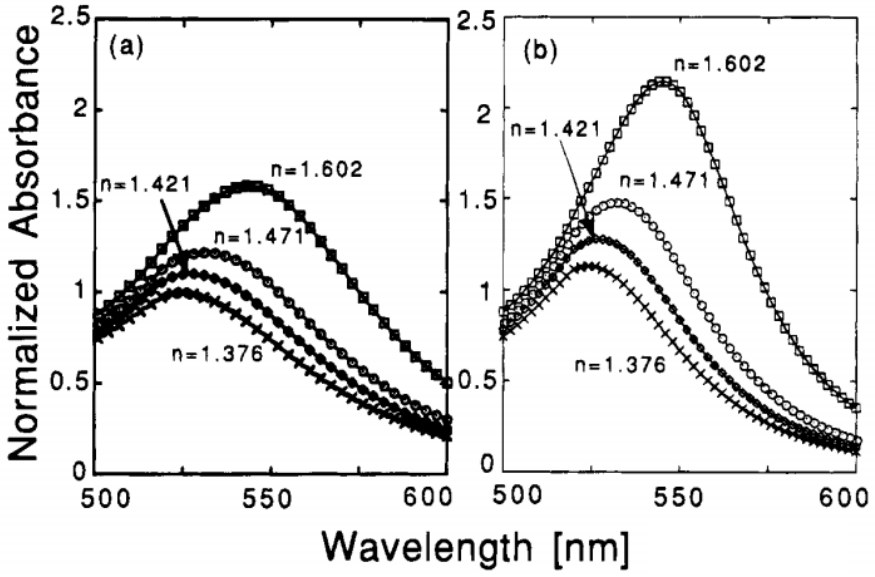

Figure 2.4. (a) Calculated and (b) experimentally obtained extinction spectra for 8nm gold nanoparticles suspended in different media, cyclohexane (n=1376), dodecane (n=1.421), decalin (n=1.471), and carbon disulfide (n=1.602). Adapted with permission from Reference 28. Copyright (1994) American Chemical Society.

2.4 LSPRs IN COPPER CHALCOGENIDE SEMICONDUCTOR NCs

Over the past decade, degenerately-doped semiconductor nanocrystals have emerged as a new class of plasmonic nanomaterials with highly tunable LSPR properties over a wide spectral range, which stems from active control over the carrier density in the nanocrystals.[30-32] Although it is well-known that the LSPR characteristics of metal nanoparticles can be tuned by variation of the size, shape, choice of metal, or dielectric environment surrounding the nanoparticles, plasmonic metal nanoparticles offer a limited LSPR tunability due to their high charge carrier concentration

on the order of ~10^{22} cm^{-3}.[30-32] Since the spectral position of the LSPR is strongly affected by its charge carrier concentrations (**Figure 2.5**),[33] degenerately-doped semiconductor nanocrystals are an attractive subset of plasmonic materials that enable more control over their LSPR properties.

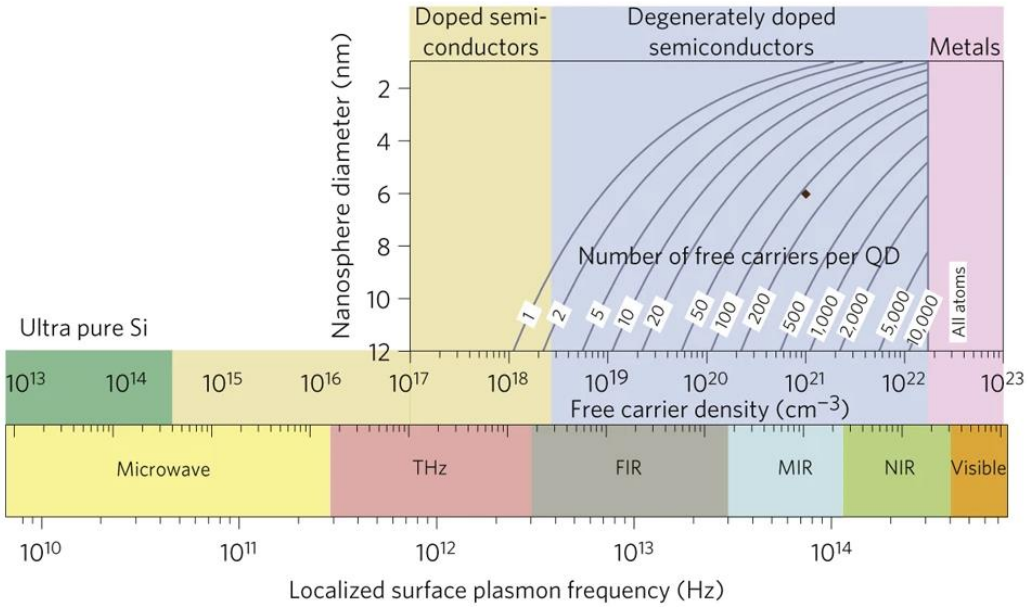

Figure 2.5. Dependence of the LSPR frequency on the concentration of free charge carriers in a spherical nanoparticle. Reprinted with permission from Reference 33. Copyright (2011) Macmillan Publishers Ltd: Nature Materials.

Notably, unlike metallic nanoparticles, the LSPR frequency of degenerately doped semiconductor nanocrystals can be tuned over a broad wavelength range in the near- to mid-infrared by controlling the degree of doping.[30-32] More interestingly, the LSPR in plasmonic semiconductor NCs can also be dynamically modulated via post-synthetic chemical, photochemical, and electrochemical reactions.[30-32] Such flexible capability of the LSPR in degenerately-doped semiconductor NCs has opened new possibilities for the application of plasmonic nanomaterials in sensors, electrochromics, and optoelectronic devices.[30-32]

To date, LSPRs in nonmetallic nanomaterials have been found for a variety of degenerately doped semiconductor nanocrystals, including copper chalcogenides,[33-37] oxygen-deficient transition metal oxides,[38-39] doped metal oxides,[40-44] and phosphorous or boron-doped silicon nanocrystals.[45-47] Among many plasmonic semiconductor nanocrystals, copper chalcogenide NCs, namely copper sulfide, copper selenide, copper telluride, and the related alloy NCs, have captured researchers' attention due to their unique properties of self-doping induced by intrinsic formation of copper vacancies in ambient air.[33, 35-37]

Since the discovery of LSPRs in copper sulfide semiconductor NCs by Zhao *et al.* in 2009,[34] many studies have demonstrated that copper chalcogenide NCs can sustain LSPRs through the resonant excitation of high concentrations of free hole carriers present in the valence band generated by large numbers of copper vacancies.[33-37] **Figure 2.6** shows the evolution of the LSPR in binary copper chalcogenide NCs, which arises from the large level of copper vacancies in the material upon exposure to air.[35] Moreover, it has been reported that the position and intensity of the LSPR peak are sensitive to the hole carrier density and chemical composition within the nanocrystals.[33-37, 48-50] Therefore, the LSPR characteristics of the copper chalcogenide NCs can be tuned through the engineering of copper vacancies either by modulating chemical composition and crystal structure during synthesis or using a post-synthetic modification of the NCs via redox reaction.[36-37, 48-50]

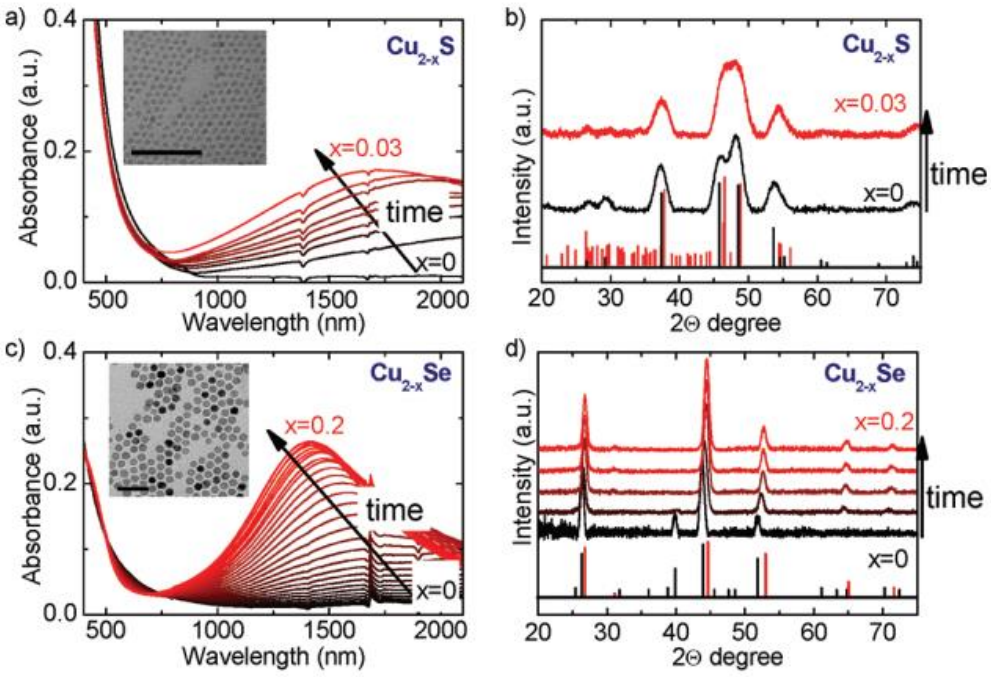

Figure 2.6. Evolution of the LSPR in copper chalcogenide NCs during oxidation. Optical and structural changes of (a) $Cu_{2-x}S$ and (b) $Cu_{2-x}Se$ NCs as a function of oxidation under ambient conditions. Adapted with permission from Reference 35. Copyright (2012) American Chemical Society.

2.5 Optical Properties of $CuFeS_2$ Nanocrystals: Quasi-Static Dielectric Resonance

Recently, increasing attention has been paid to the optical properties of $CuFeS_2$ NCs that exhibit a pronounced "plasmon-like" resonant absorption in the visible spectrum.[51-54] The unique optical properties of $CuFeS_2$ NCs have been ascribed to the occurrence of LSPR without solid evidence due to the similarity with the optical properties of gold nanoparticles.[51-52] However, considering the low free carrier density of all-dielectric intermediate-band semiconductor $CuFeS_2$ NCs,[54-55] this interpretation is doubtful because plasmonic nanomaterials rely on large free carrier

densities to generate a negative permittivity at the LSPR frequency – thus enabling the Fröhlich resonance condition and associated divergent polarizability that gives rise to resonant absorption and scattering features.[54]

A recent report by Gaspari *et al.* theoretically showed that the plasmonic-like behavior of $CuFeS_2$ NCs is associated with the intermediate band in this material, which enables a negative permittivity in the visible region.[54] As a result, the unique electronic structure of intermediate band semiconductors can provide quasi-static optical resonances in $CuFeS_2$ NCs, in contrast to the free-carrier reliant LSPR that occurs in plasmonic metal nanoparticles. However, the quasi-static dielectric resonance in intermediate band semiconductor nanocrystals has not been widely studied as yet and is rarely reported in the literature.

2.6 REFERENCES

1. Stratton, J. A., *Electromagnetic Theory*. McGraw-Hill Book Company, 1941.
2. Craig F. Bohren; D. R. H., *Absorption and Scattering of Light by Small Particles*. Wiley, 1998.
3. Toropov, A. A.; Shubina, T. V., *Plasmonic Effects in Metal-Semiconductor Nanostructures*. Oxford University Press, 2015.
4. Maier, S. A., *Plasmonics: Fundamentals and Applications*. Springer, 2007.
5. Kerker, M.; Press, A., *The Scattering of Light, and Other Electromagnetic Radiation*. Academic Press, 1969.
6. Born, M.; Wolf, E., *Principles of Optics: Electromagnetic Theory of Propagation, Interference and Diffraction of Light*. Pergamon Press, 1959.
7. D, J. J., *Classical Electrodynamics*. John Wiley, 1975.
8. Cheng, D. K., *Field and Wave Electromagnetics*. Addison-Wesley Publishing Company, 1989.
9. Lee, Y. H., *Introduction to Engineering Electromagnetics*. Springer Berlin Heidelberg, 2013.
10. Nickelson, L., *Electromagnetic Theory and Plasmonics for Engineers*. Springer Singapore, 2018.
11. Quinten, M., *Optical Properties of Nanoparticle Systems: Mie and Beyond*. Wiley, 2011.

12. Shah, K., *Plasma and Plasmonics*. De Gruyter, 2018.

13. Pelton, M.; Bryant, G. W., *Introduction to Metal-Nanoparticle Plasmonics*. Wiley, 2013.

14. Drude, P., Zur Elektronentheorie der Metalle. *Annalen der Physik* **1900,** *306* (3), 566-613.

15. Hartland, G. V., Optical Studies of Dynamics in Noble Metal Nanostructures. *Chemical Reviews* **2011,** *111* (6), 3858-3887.

16. Shabaninezhad, M.; Ramakrishna, G., Theoretical Investigation of Plasmonic Properties of Quantum-Sized Silver Nanoparticles. *Plasmonics* **2020,** *15* (3), 783-795.

17. Fan, X.; Zheng, W.; Singh, D. J., Light scattering and surface plasmons on small spherical particles. *Light: Science & Applications* **2014,** *3* (6), e179-e179.

18. Eustis, S.; El-Sayed, M. A., Why gold nanoparticles are more precious than pretty gold: Noble metal surface plasmon resonance and its enhancement of the radiative and nonradiative properties of nanocrystals of different shapes. *Chemical Society Reviews* **2006,** *35* (3), 209-217.

19. Faraday, M., The Bakerian Lecture: Experimental relations of gold (and other metals) to light. *Philosophical Transactions of the Royal Society of London* **1857,** *147*, 145-181.

20. Zsigmondy, R. A.; Alexander, J., *Colloids and the Ultramicroscope: A Manual of Colloid Chemistry and Ultramicroscopy*. 1909.

21. Mie, G., Beiträge zur Optik trüber Medien, speziell kolloidaler Metallösungen. *Annalen der Physik* **1908,** *330* (3), 377-445.

22. Link, S.; El-Sayed, M. A., Spectral Properties and Relaxation Dynamics of Surface Plasmon Electronic Oscillations in Gold and Silver Nanodots and Nanorods. *The Journal of Physical Chemistry B* **1999,** *103* (40), 8410-8426.

23. Kelly, K. L.; Coronado, E.; Zhao, L. L.; Schatz, G. C., The Optical Properties of Metal Nanoparticles: The Influence of Size, Shape, and Dielectric Environment. *The Journal of Physical Chemistry B* **2003,** *107* (3), 668-677.

24. Evanoff Jr., D. D.; Chumanov, G., Synthesis and Optical Properties of Silver Nanoparticles and Arrays. *ChemPhysChem* **2005,** *6* (7), 1221-1231.

25. Murphy, C. J.; Sau, T. K.; Gole, A. M.; Orendorff, C. J.; Gao, J.; Gou, L.; Hunyadi, S. E.; Li, T., Anisotropic Metal Nanoparticles: Synthesis, Assembly, and Optical Applications. *The Journal of Physical Chemistry B* **2005,** *109* (29), 13857-13870.

26. Myroshnychenko, V.; Rodríguez-Fernández, J.; Pastoriza-Santos, I.; Funston, A. M.; Novo, C.; Mulvaney, P.; Liz-Marzán, L. M.; García de Abajo, F. J., Modelling the optical response of gold nanoparticles. *Chemical Society Reviews* **2008,** *37* (9), 1792-1805.

27. Mock, J. J.; Barbic, M.; Smith, D. R.; Schultz, D. A.; Schultz, S., Shape effects in plasmon resonance of individual colloidal silver nanoparticles. *The Journal of Chemical Physics* **2002,** *116* (15), 6755-6759.

28. Underwood, S.; Mulvaney, P., Effect of the Solution Refractive Index on the Color of Gold Colloids. *Langmuir* **1994,** *10* (10), 3427-3430.

29. Mayer, K. M.; Hafner, J. H., Localized Surface Plasmon Resonance Sensors. *Chemical Reviews* **2011,** *111* (6), 3828-3857.

30. Comin, A.; Manna, L., New materials for tunable plasmonic colloidal nanocrystals. *Chemical Society Reviews* **2014,** *43* (11), 3957-3975.

31. Agrawal, A.; Cho, S. H.; Zandi, O.; Ghosh, S.; Johns, R. W.; Milliron, D. J., Localized Surface Plasmon Resonance in Semiconductor Nanocrystals. *Chemical Reviews* **2018,** *118* (6), 3121-3207.

32. Kriegel, I.; Scotognella, F.; Manna, L., Plasmonic doped semiconductor nanocrystals: Properties, fabrication, applications and perspectives. *Physics Reports* **2017,** *674*, 1-52.

33. Luther, J. M.; Jain, P. K.; Ewers, T.; Alivisatos, A. P., Localized surface plasmon resonances arising from free carriers in doped quantum dots. *Nature Materials* **2011,** *10* (5), 361-366.

34. Zhao, Y.; Pan, H.; Lou, Y.; Qiu, X.; Zhu, J.; Burda, C., Plasmonic $Cu_{2-x}S$ Nanocrystals: Optical and Structural Properties of Copper-Deficient Copper(I) Sulfides. *Journal of the American Chemical Society* **2009,** *131* (12), 4253-4261.

35. Kriegel, I.; Jiang, C.; Rodríguez-Fernández, J.; Schaller, R. D.; Talapin, D. V.; da Como, E.; Feldmann, J., Tuning the Excitonic and Plasmonic Properties of Copper Chalcogenide Nanocrystals. *Journal of the American Chemical Society* **2012,** *134* (3), 1583-1590.

36. Dorfs, D.; Härtling, T.; Miszta, K.; Bigall, N. C.; Kim, M. R.; Genovese, A.; Falqui, A.; Povia, M.; Manna, L., Reversible Tunability of the Near-Infrared Valence Band Plasmon Resonance in $Cu_{2-x}Se$ Nanocrystals. *Journal of the American Chemical Society* **2011,** *133* (29), 11175-11180.

37. Saldanha, P. L.; Brescia, R.; Prato, M.; Li, H.; Povia, M.; Manna, L.; Lesnyak, V., Generalized One-Pot Synthesis of Copper Sulfide, Selenide-Sulfide, and Telluride-Sulfide Nanoparticles. *Chemistry of Materials* **2014,** *26* (3), 1442-1449.

38. Manthiram, K.; Alivisatos, A. P., Tunable Localized Surface Plasmon Resonances in Tungsten Oxide Nanocrystals. *Journal of the American Chemical Society* **2012,** *134* (9), 3995-3998.

39. Huang, Q.; Hu, S.; Zhuang, J.; Wang, X., MoO_{3-x}-Based Hybrids with Tunable Localized Surface Plasmon Resonances: Chemical Oxidation Driving Transformation from Ultrathin Nanosheets to Nanotubes. *Chemistry – A European Journal* **2012,** *18* (48), 15283-15287.

40. Kanehara, M.; Koike, H.; Yoshinaga, T.; Teranishi, T., Indium Tin Oxide Nanoparticles with Compositionally Tunable Surface Plasmon Resonance Frequencies in the Near-IR Region. *Journal of the American Chemical Society* **2009,** *131* (49), 17736-17737.

41. Lounis, S. D.; Runnerstrom, E. L.; Llordés, A.; Milliron, D. J., Defect Chemistry and Plasmon Physics of Colloidal Metal Oxide Nanocrystals. *The Journal of Physical Chemistry Letters* **2014,** *5* (9), 1564-1574.

42. Buonsanti, R.; Llordes, A.; Aloni, S.; Helms, B. A.; Milliron, D. J., Tunable Infrared Absorption and Visible Transparency of Colloidal Aluminum-Doped Zinc Oxide Nanocrystals. *Nano Letters* **2011,** *11* (11), 4706-4710.

43. Gordon, T. R.; Paik, T.; Klein, D. R.; Naik, G. V.; Caglayan, H.; Boltasseva, A.; Murray, C. B., Shape-Dependent Plasmonic Response and Directed Self-Assembly in a New Semiconductor Building Block, Indium-Doped Cadmium Oxide (ICO). *Nano Letters* **2013,** *13* (6), 2857-2863.

44. Garcia, G.; Buonsanti, R.; Runnerstrom, E. L.; Mendelsberg, R. J.; Llordes, A.; Anders, A.; Richardson, T. J.; Milliron, D. J., Dynamically Modulating the Surface Plasmon Resonance of Doped Semiconductor Nanocrystals. *Nano Letters* **2011,** *11* (10), 4415-4420.

45. Kramer, N. J.; Schramke, K. S.; Kortshagen, U. R., Plasmonic Properties of Silicon Nanocrystals Doped with Boron and Phosphorus. *Nano Letters* **2015,** *15* (8), 5597-5603.

46. Rowe, D. J.; Jeong, J. S.; Mkhoyan, K. A.; Kortshagen, U. R., Phosphorus-Doped Silicon Nanocrystals Exhibiting Mid-Infrared Localized Surface Plasmon Resonance. *Nano Letters* **2013,** *13* (3), 1317-1322.

47. Zhou, S.; Pi, X.; Ni, Z.; Ding, Y.; Jiang, Y.; Jin, C.; Delerue, C.; Yang, D.; Nozaki, T., Comparative Study on the Localized Surface Plasmon Resonance of Boron- and Phosphorus-Doped Silicon Nanocrystals. *ACS Nano* **2015,** *9* (1), 378-386.

48. Wang, X.; Swihart, M. T., Controlling the Size, Shape, Phase, Band Gap, and Localized Surface Plasmon Resonance of $Cu_{2-x}S$ and Cu_xIn_yS Nanocrystals. *Chemistry of Materials* **2015,** *27* (5), 1786-1791.

49. Liu, X.; Wang, X.; Swihart, M. T., $Cu_{2-x}S_{1-y}Se_y$ Alloy Nanocrystals with Broadly Tunable Near-Infrared Localized Surface Plasmon Resonance. *Chemistry of Materials* **2013,** *25* (21), 4402-4408.

50. Jain, P. K.; Manthiram, K.; Engel, J. H.; White, S. L.; Faucheaux, J. A.; Alivisatos, A. P., Doped Nanocrystals as Plasmonic Probes of Redox Chemistry. *Angewandte Chemie International Edition* **2013,** *52* (51), 13671-13675.

51. Gabka, G.; Bujak, P.; Ostrowski, A.; Tomaszewski, W.; Lisowski, W.; Sobczak, J. W.; Pron, A., Cu–Fe–S Nanocrystals Exhibiting Tunable Localized Surface Plasmon Resonance in the Visible to NIR Spectral Ranges. *Inorganic Chemistry* **2016,** *55* (13), 6660-6669.

52. Kowalik, P.; Bujak, P.; Penkala, M.; Kotwica, K.; Kmita, A.; Gajewska, M.; Ostrowski, A.; Pron, A., Synthesis of $CuFeS_{2-x}Se_x$ – alloyed nanocrystals with localized surface plasmon resonance in the visible spectral range. *Journal of Materials Chemistry C* **2019,** *7* (21), 6246-6250.

53. Sugathan, A.; Bhattacharyya, B.; Kishore, V. V. R.; Kumar, A.; Rajasekar, G. P.; Sarma, D. D.; Pandey, A., Why Does $CuFeS_2$ Resemble Gold? *The Journal of Physical Chemistry Letters* **2018,** *9* (4), 696-701.

54. Gaspari, R.; Della Valle, G.; Ghosh, S.; Kriegel, I.; Scotognella, F.; Cavalli, A.; Manna, L., Quasi-Static Resonances in the Visible Spectrum from All-Dielectric Intermediate Band Semiconductor Nanocrystals. *Nano Letters* **2017,** *17* (12), 7691-7695.

55. Ghosh, S.; Avellini, T.; Petrelli, A.; Kriegel, I.; Gaspari, R.; Almeida, G.; Bertoni, G.; Cavalli, A.; Scotognella, F.; Pellegrino, T.; Manna, L., Colloidal $CuFeS_2$ Nanocrystals: Intermediate Fe d-Band Leads to High Photothermal Conversion Efficiency. *Chemistry of Materials* **2016,** *28* (13), 4848-4858.

Chapter 3. IRON-CONTENT-DEPENDENT, QUASI-STATIC DIELECTRIC RESONANCE AND LOCALIZED SURFACE PLASMON RESONANCE IN COPPER IRON SULFIDE NANOCRYSTALS

3.1 INTRODUCTION

Transition metals with partially filled d-orbitals are known to bestow interesting electronic, magnetic, and optical characteristics to the materials they constitute.[1-5] For instance, Re^{6+} being a d^1 system, confers metallic character to rhenium (+6) oxide,[3, 6] while the incorporation of Cr^{3+} (d^1 system) enables lower-energy photon absorption in relatively wide band gap semiconductors like $CuGaS_2$.[7] In metal sulfides, this influence manifests in the form of delocalized d-levels, which form a narrow band near the top of the valence band (VB) or deep in the band gap.[5, 8-9] The presence of this intermediate band (IB) has been demonstrated to render hitherto unknown optical responses at the nanoscale, as has recently been demonstrated for colloidal nanocrystals (NCs) of $CuFeS_2$,[5, 10-11] and Cu_3VS_4.[4, 12-13] Further, from the perspective of practical applications, IB semiconductor NCs are of significance as they enable a more efficient absorption of solar radiation,[14-15] improved thermoelectric efficiency,[16-17] and can be used as photothermal agents for cancer therapy.[5, 18-20]

Among the nanoscale metal chalcogenides, colloidal NCs of copper chalcogenides have been actively studied in recent times, owing to their structural, compositional, and stoichiometric versatility, and more importantly, for the "self-doped" intrinsic formation of copper vacancies that lead to the localized surface plasmon resonance (LSPR) response in the near infrared (NIR) region of the electromagnetic spectrum.[21-25] This optical response of binary copper chalcogenide NCs is tunable through manipulation of their composition, and the same principles have lately been extended to ternary and quaternary chalcogenide NCs as well,[25-27] albeit the mechanism underlying

the optical responses can be fundamentally different in different material systems. For instance, in contrast to the widely studied plasmonic Cu-S NCs, Ghosh and Gaspari *et al.* recently showed that a metal-like optical response in chalcopyrite $CuFeS_2$ NCs can be attributed to its unique band structure, which constitutes an IB of states generated by empty Fe 3d orbitals.[5, 10] Remarkably, when the IB is sufficiently close to the VB edge, the material can exhibit a negative real permittivity across a broad range of visible frequencies.[10] This negative real permittivity enables a Fröhlich resonance condition, leading to a quasi-static dielectric resonance (DR) and associated resonant absorption in the visible frequency regime, despite a complete lack of ground-state free charge carriers, as demonstrated in nanoscale $CuFeS_2$.[5, 10]

The presence of Fe, as the transition metal with partially filled d-orbitals, is then the defining factor in the optical signatures from these Cu-Fe-S systems. Similar to the experiments on binary Cu-S NCs, a modulation of this optical response through changing compositions has been demonstrated in some nanoscale Cu-Fe-S semiconductors.[28-30] For instance, the introduction of Cd in Cu-Fe-S NCs rendered them luminescent,[28] while a modulation of the DR was demonstrated through changing the S:Se ratio in $CuFeS_{2-x}Se_x$ alloyed NCs.[30] However, a comprehensive demonstration of the influence of changing Fe content on the optical responses of Cu-Fe-S NCs is necessary to develop a proper understanding of the spectral influence of the Fe 3d orbitals, and devise practical applications of these nanoscale semiconductors.

Here, we investigate the influence of iron content on the optical resonances and concomitantly, the electronic structure of bornite-phase, copper iron sulfide NCs, synthesized *via* a colloidal hot-injection route. The synthesis entails rapidly introducing a reactive sulfur precursor into a hot solution of copper and iron precursors in admixture with excess halide ions and organic surfactants. This halide-assisted synthetic method enabled both a monodisperse size distribution

and control over the composition of the as-synthesized bornite NCs, allowing for delineation of the relationship between Fe content, electronic structure, and the spectral characteristics of nanoscale Cu-Fe-S systems. As the Fe content of the as-synthesized bornite NCs was varied from 4.1 to 12.5%, significant changes in their optical extinction spectra were observed, with high-Fe-content NCs exhibiting the appearance of a strong absorption band in the visible frequency regime (centered at 490 nm; 2.53 eV), which we attribute to a Fe-3d IB-associated DR, while the low-Fe-content NCs exhibit a NIR LSPR response (centered at 1000 nm; 1.24 eV). Further, a DR-to-LSPR transition could be induced *via* simple aerobic oxidation of the as-synthesized bornite NCs, which was ascribed to the oxidatively driven removal of Fe (out of the NCs) by careful elemental analysis of the NC composition. A similar spectral transition was also demonstrated on chalcopyrite ($CuFeS_2$) NCs *via* controlled oxidation and addition of ions, which further corroborates the role of Fe 3d orbitals in the emergence of the visible frequency DR centered at 490 nm (2.53 eV) in nanoscale Cu-Fe-S systems. Density functional theory (DFT) calculations lend additional evidence in this regard, showing an increased contribution to the density of states in the IB as the Fe content of the bornite NCs is increased. These spectral changes are visually discernible, as the DR induces a purple-colored NC dispersion while the LSPR leads to a green color, for both bornite and chalcopyrite NCs. These joint investigations validate that the intense 490-nm band in nanoscale Cu-Fe-S systems cannot be attributed to the more widely known LSPR response that arises from the collective oscillations of free charge carriers, and is indeed due to their unique band structure which contains an intermediate Fe d-band that enables a Frölich resonance in the visible region. These optical modulations *via* compositional tuning yield a more holistic understanding of the DR response of Cu-Fe-S NCs, and can be further engineered into dynamic material systems.

3.2 Results and Discussion

The synthesis of bornite-phase copper iron sulfide NCs with controlled iron-content was performed *via* hot injection on a Schlenk line, where a reactive sulfur precursor (hexamethyldisilathiane in octadecene) was rapidly injected into a hot solution of copper (II) and iron (III) chlorides in a mixture of trioctylphosphine oxide, oleylamine, oleic acid and octadecene. The metal-precursor solution was also charged with excess sodium chloride, in order to ensure that the reaction medium was halide rich. The presence of excess halide species was necessary to obtain the desired iron-content while maintaining a monodisperse size distribution in these NCs,[31] as it is important to balance the reactivity of the two metal precursors for a chosen stoichiometry in ternary copper chalcogenide NCs,[5, 32] as has been demonstrated previously for various colloidal NCs.[32-34] When the synthesis was performed with no added halide ions in the system, large, polydisperse, low-iron-content bornite NCs with a platelet-like morphology resulted, predominantly exhibiting a broad NIR LSPR optical signature (Figure A.1). However, for the experiments described herein, it was critical that samples of monodisperse, phase-pure bornite NCs with tunable iron content were produced (Figure A.2), both of which were achieved *via* the presence of the excess halide ions. In these syntheses, the quantity of $FeCl_3$ was adjusted relative to a fixed amount of $CuCl_2$, with representative transmission electron microscopy (TEM) and high-resolution TEM (HRTEM) images of the resulting NCs shown in **Figure 3.1**. Iron contents ranging from 4.1 at.% (**Figure 3.1**a) to 12.5 at.% (**Figure 3.1**b) were obtained, as determined by elemental analysis *via* energy-dispersive X-ray spectroscopy (Table A1), and these stoichiometries are respectively referred to as “low-Fe” and “high-Fe” bornite in this work. As a reference, the crystal structure of the two major bornite polymorphs, Cu_5FeS_4 (10 at.% Fe) and Cu_2FeS_2 (20 at.% Fe) are shown in Figure A3, where S atoms form a face-centered cubic lattice with Cu and Fe atoms residing in a subset of

the tetrahedral sites, as compared to the fully tetragonal chalcopyrite $CuFeS_2$ structure. The iron-content difference between these bornite polymorphs can be appreciated from the fact that in a unit cell, a Cu-atom in Cu_5FeS_4 is essentially replaced by an Fe-atom in Cu_2FeS_2 (or $Cu_4Fe_2S_4$, for the sake of clarity) and considering that the NCs reported here exhibit stoichiometries which can be interpolated between these extreme cases, this system is particularly well suited for studying the effect of Fe-content on the optical signatures exhibited by nanoscale Cu-Fe-S materials. In comparison, the main difference between the bornite and chalcopyrite structures is in the relative occupation of tetrahedrally coordinated Cu and Fe atoms, as can be appreciated from their crystal structures shown in Figure A.3.

The tighter size control afforded by the halide-assisted synthesis can be discerned from the fact that the as-synthesized NCs exhibit a relatively uniform size distribution with average diameters of 16.2 ± 2.1 and 15.4 ± 1.4 nm, respectively, for the low-Fe and high-Fe compositions (Figure A2). HRTEM images (**Figure 3.1**, panels a and b insets) reveal the single-crystalline nature of the as-synthesized NCs, with the measured interplanar distances corresponding to the (044) lattice planes of the cubic bornite structure. Interestingly, the measured interplanar spacing was found to be dependent on the Fe content of the NCs, with higher Fe-content NCs exhibiting a narrower (044) d-spacing. This is suggestive of lattice compression as the Fe content in the NC increases, and indeed this can be correlated to the smaller ionic radius of Fe (compared to Cu), leading to a decreased lattice constant as the Fe atoms progressively replace Cu atoms in the NC lattice. In fact, a more general set of evidence in this regard is obtained from X-ray diffraction (XRD) measurements (**Figure 3.1**c), which further corroborates the observed trend. The high-Fe bornite NC diffraction patterns can be clearly ascribed to the cubic bornite phase (**Figure 3.1**c), with the indexed diffraction peaks systematically shifting toward higher Bragg angles upon

increasing Fe content. As mentioned above, the NCs reported herein exhibit stoichiometries which range between the bornite polymorphs of Cu_5FeS_4 and Cu_2FeS_2, and this fact is also apparent in the XRD patterns shown in Figure 1c. Cu_2FeS_2 exhibits higher Bragg angles in comparison to Cu_5FeS_4, in line with the fact that Cu_2FeS_2 has a higher Fe-content (20%) and the high-Fe bornite NCs (12.5% Fe) actually exhibit Bragg angles closer to the Cu_2FeS_2 polymorph. On the other hand, low-Fe bornite NCs (4.1% Fe) have Bragg angles closer to the Cu_5FeS_4 polymorph, while the other stoichiometries systematically fall in between these cases. In addition, this systematic shift in the XRD patterns confirms that the additional iron has been uniformly incorporated into the crystal lattice.[35-36] The lattice constants calculated from each of the measured XRD patterns are plotted in Figure 1d as a function of the measured Fe-content for each respective sample. Notably, the calculated lattice constants are remarkably consistent with the lattice parameters determined from TEM (Figure A.4), with the results of both measurements shown overlaid in Figure A5. However, the most striking difference between the low-Fe and high-Fe bornite NCs is in their optical extinction profiles (**Figure 3.1**e), which were found to exhibit strong, resonant extinction features with iron-content-dependent intensities at distinct visible and near-infrared (NIR) frequencies. As discussed in detail below, we attribute these extinction features to two fundamentally different types of resonant excitation.

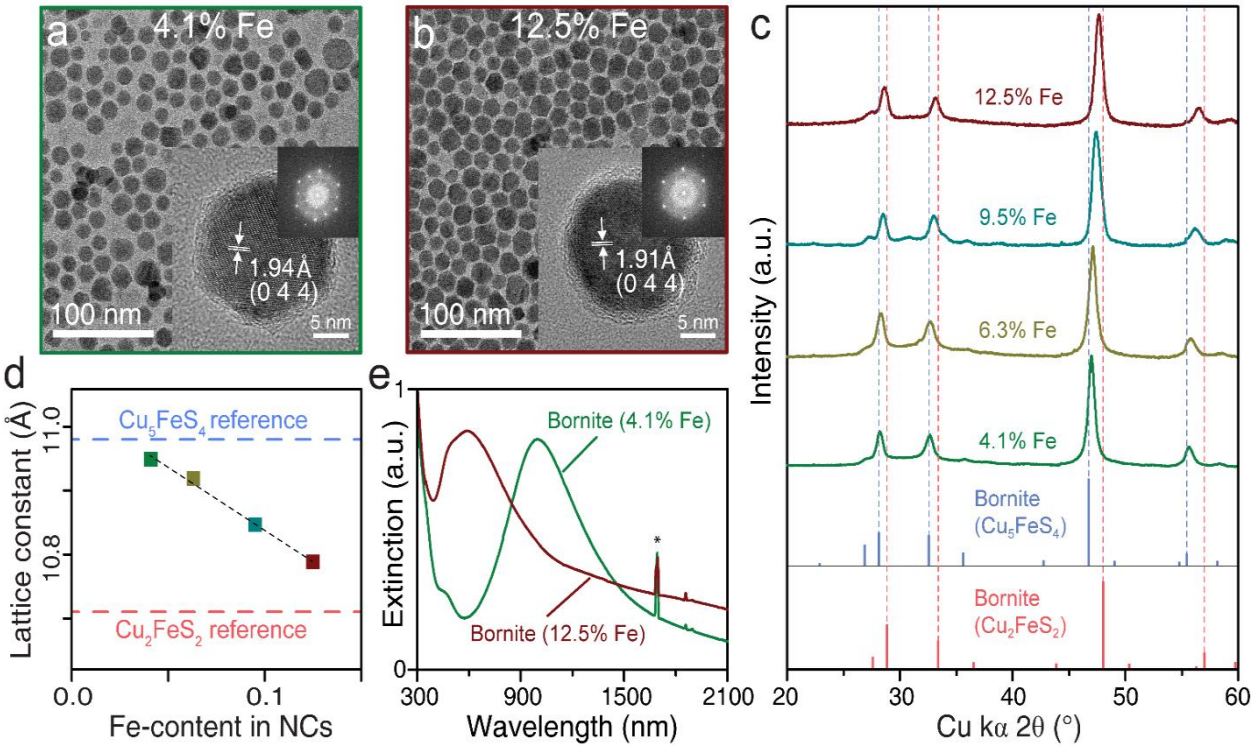

Figure 3.1. Structural and morphological characterization of the as-synthesized bornite NCs. TEM images of (a) low-Fe and (b) high-Fe bornite NCs; insets show the respective HRTEM images and fast Fourier transforms of individual NCs. (c) XRD patterns of NC samples with varied Fe-content, in comparison to reference lines for bornite Cu_5FeS_4 (PDF #98-000-6587; blue lines) and bornite Cu_2FeS_2 (PDF #98-000-4849; red lines). (d) Bornite NC lattice constants determined from the XRD patterns in panel c, flanked by representative bornite polymorphs. (e) UV-vis-NIR extinction spectra of as-synthesized bornite NCs with the lowest and highest Fe content. Spectral artifacts caused by the NIR absorption bands of the chloroform solvent are marked by asterisks.

Since the absorption and scattering cross-sections of a colloidal nanostructure are directly related to its polarizability, where $\sigma_{abs} = k \cdot Im\{\alpha\}$, $\sigma_{scat} = \frac{k^4}{6\pi}|\alpha|^2$, and k is the wavevector of the incident light, the wavelengths at which resonant extinction features occur can be readily determined *via* an examination of the polarizability, α, of the nanostructure, which can be extracted by solving Maxwell's equations for a dielectric particle subjected to an incident electromagnetic

wave.[37] For a nanostructure with a spherical shape, the resulting polarizability is given by the following Mie theory expression:

$$\alpha = 3\epsilon_0 V \frac{(\varepsilon - \varepsilon_m)}{(\varepsilon + 2\varepsilon_m)} \quad (3.1)$$

where ϵ_0 is the permittivity of free space, V is the volume of the nanostructure, ε_m is the dielectric function of the surrounding medium, and ε is the complex permittivity of the nanostructure itself.[37] At certain frequencies, depending on the relative permittivities of the nanostructure and the surrounding medium, the denominator of the above expression for the polarizabilty approaches zero, resulting in a divergent polarizibility and subsequent resonant abosorption and scattering profiles.[37] For a dielectric sphere, the Fröhlich resonance condition (where $\varepsilon + 2\varepsilon_m \rightarrow 0$) occurs at specific frequencies where the real component of the nanostructure permittivity, ε', is equal to $-2\varepsilon_m$.[37] Thus, for colloidal NCs with typical ligands and solvent media, resonant absorption and scattering features occur at frequencies where the real component of the nanostructure dielectric function becomes negative.[3, 38-39]

For metallic and highly doped semiconductor nanostructures, it is the high density of free charge carriers that enables a negative real permittivity, typically in the visible-to-infrared frequency regime, resulting in the collective, coherent excitation of a localized surface plasmon resonance (LSPR) at the frequency where the polarizability of the structure diverges.[38-40] While free-charge-carrier-enabled localized surface plasmon resonances (LSPRs) are perhaps the most well-known class of resonant excitation in colloidal nanomaterials, it should be noted that other important modes of resonant excitation also exist. Since the permittivity of an inorganic material is a complex, additive function with many components, including free carrier contributions, interband and intraband electronic excitations, and phononic vibrational excitations, these collective contributions can give rise to negative real permittivities at a variety of frequencies.[38]

For example, many inorganic dielectric materials exhibit high-frequency negative permittivities, and Mie resonances at the corresponding energies in the ultraviolet are quite common.[3, 41-42] Moreover, as mentioned earlier in the introduction, it was recently demonstrated that IB semiconductor NCs can exhibit visible-frequency negative real permittivities that give rise to strong, visible-frequency DR if the material possesses an IB of states that lies in close proximity to the edge of the VB.[10]

As can be seen in Figure 1e and S9, low-Fe and high-Fe bornite NCs exhibit dramatically different UV-vis-NIR extinction spectra that depend strongly on the Fe content of the NC. While low-Fe bornite NCs (< 7 at.% Fe) were found to exhibit a strong LSPR peak in the NIR, similar to what has been observed previously in many copper sulfide NC systems,[43-45] an additional extinction feature centered at 490 nm, which is not typically observed in copper sulfide NCs, was also observed. For the high-Fe bornite compositions (above ~9%), the small feature at 490 nm was found to have significantly increased intensity (**Figure 3.1**e), dominating the extinction characteristics of the material relative to the NIR LSPR response observed in the low-Fe bornite NCs.

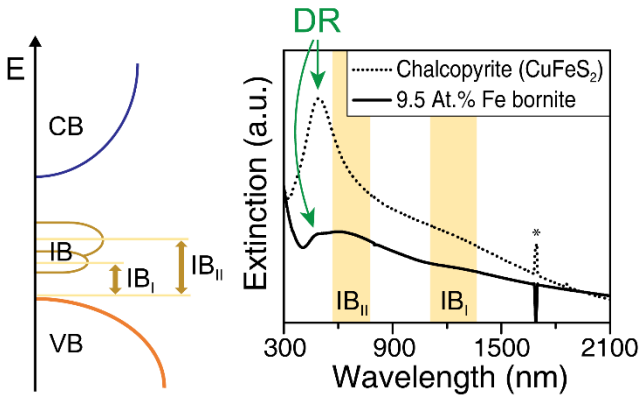

Figure 3.2. A schematic band structure of chalcopyrite-phase copper iron sulfide showing the optical transitions between states in the valence band (VB) and the intermediate band (IB), and comparison of UV-vis-NIR extinction spectra of stoichiometric chalcopyrite NCs and bornite

NCs with 9.5 at.% Fe. Spectral artifacts caused by the NIR absorption bands of the chloroform solvent are marked by asterisks.

Notably, absorption features with iron-content-dependent intensities have been observed in bulk-scale, Fe-doped, chalcopyrite-phase $CuGaS_2$ and $CuAlS_2$ materials.[46] These previous observations, along with the recent demonstration of quasi-static dielectric resonances in chalcopyrite-phase copper iron sulfide NCs,[10] led us to hypothesize that the strongly iron-content-dependent optical transition that we observe in bornite-phase copper iron sulfide may potentially be due to resonant transitions associated with a set of Fe-related states near the edge of the bornite VB. As a comparison, chalcopyrite-phase $CuFeS_2$ NCs with analogous sizes were also synthesized, with the extinction characteristics of bornite-phase, 9.5 at.% Fe NCs shown overlaid on the chalcopyrite $CuFeS_2$ extinction data (**Figure 3.2**). The previously reported DR is clearly observed in the chalcopyrite sample, at a similar frequency to that of the observed 490-nm extinction peak in the bornite NC samples. Furthermore, two additional distinguishable absorption features are observed as broad shoulders in the high-Fe bornite NCs, with peak positions at about 600 nm and 1250 nm, respectively. Notably, these two absorption bands also closely resemble the electronic transitions from the VB to the IB in chalcopyrite copper iron sulfide NCs that were previously reported by Oguchi *et al.*,[47] suggesting the existence of two similar sub-bandgap transitions in the bornite-phase copper iron sulfide NCs.

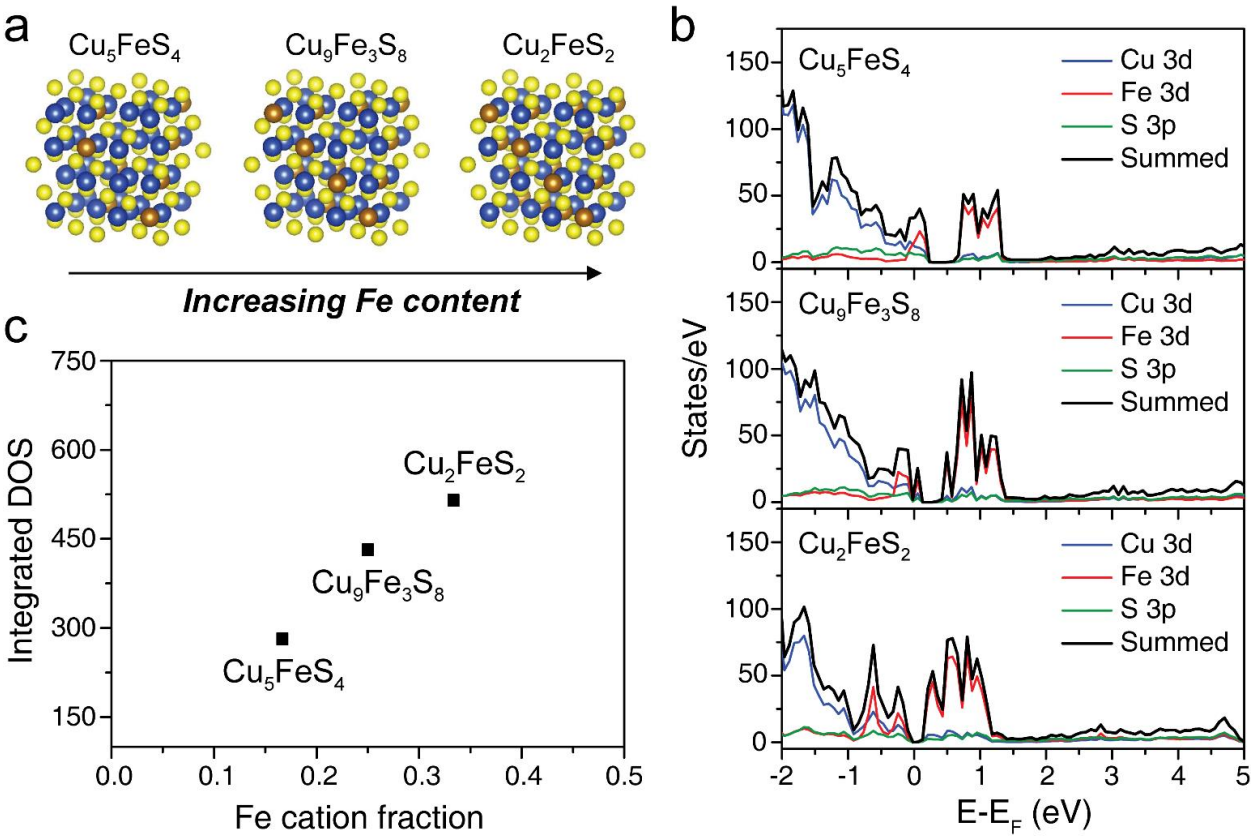

Figure 3.3. (a) Crystal structures, (b) atomic-projected density of states (DOS), and (c) integrated DOS of Fe 3d in the IB for a series of bornite copper iron sulfides.

In order to test the hypothesis that the iron-related extinction feature of bornite in the visible region occurs due to the mid-gap Fe 3d states located above the VB edge, density functional theory (DFT) calculations were carried out to determine the electronic structure of bornite-phase copper iron sulfide with different levels of iron content. Using intermediate-cubic-phase bornite (Cu_5FeS_4, *Fm3m*; 10 at.% Fe) as a starting point – as corroborated by the experimental XRD patterns in Figure 1 – the stoichiometry was systematically altered by gradually replacing tetrahedrally coordinated Cu atoms with additional Fe. The resulting integrated density of states (DOS) for three different stoichiometric bornite phases are shown in **Figure 3.3**a. As can be seen from the atomic-projected DOS curves (**Figure 3.3**b), bornite indeed possesses an intense IB of states dominated by empty Fe 3d orbitals just above the VB. Moreover, the integrated density of states in the IB is

strongly dependent on the iron content of the material (**Figure 3.3**c), agreeing with the iron-content-dependent intensity of the resonant optical transition observed at 490 nm in the bornite-phase NCs. Due to the strong similarities with the computational results of Gaspari *et al.*,[10] our data suggests that bornite NCs are an example of an IB semiconductor that exhibits a tunable, iron-content-dependent quasi-static DR in the visible frequency range. Also, we observe that the partial substitution of Cu atoms in Cu_5FeS_4 by Fe not only increases the DOS of the IB, but also decreases the gap between the VB and the IB, thus favoring the occurrence of a quasi-static DR by extending the range of negative permittivity.[10]

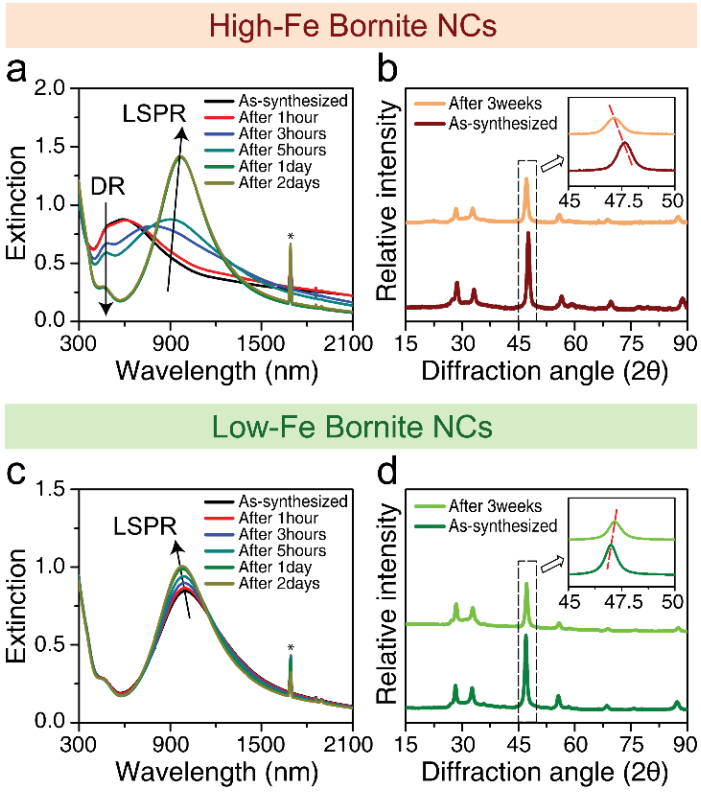

Figure 3.4. Optical and structural changes of the bornite NCs as a function of oxidation under ambient conditions. (a, b) high-Fe, and (c, d) low-Fe bornite NCs. Panels a and c show the spectral evolution of the respective NCs as the oxidation progresses over the course of two days. Spectral artifacts caused by the NIR absorption bands of the chloroform solvent are marked by asterisks. Panels b and d include the XRD patterns collected for the as-synthesized NCs and the oxidized NCs after 3 weeks of air exposure.

It is well known that nanoscale binary copper chalcogenides are prone to oxidation into more thermodynamically stable phases, and these phase changes are accompanied with changes in their optical characteristics.[48-49] Binary copper chalcogenides become self-doped upon exposure to air, through the well-established mechanism of Cu atom expulsion,[49] due to the high mobility of Cu ions in these lattices.[50] However, in a ternary Cu-Fe-S system like bornite or chalcopyrite, the iron atoms are in an energetically unfavorable tetrahedral coordination, which makes lattice expulsion of Fe-atoms upon external influence more likely.[51] In fact, very few naturally occurring minerals are found with Fe atoms in tetrahedral coordination due to this reason,[52] and likewise, we found that oxidation of as-synthesized bornite NCs leads to expulsion of Fe atoms from the lattice. The resulting variations in the iron content of the NCs have a large impact on their spectral characteristics. In case of the high-Fe bornite NCs, the initially dominant extinction feature at 490 nm decreases in intensity as the Fe-atoms are slowly expelled from the NCs by exposing them to ambient conditions (**Figure 3.4**a), while the NIR LSPR feature gradually intensifies and eventually dominates the spectrum. The origin of this LSPR band in these oxidized NCs is similar to that of binary Cu-S NCs, where metal vacancies in the NC lattice leave holes behind as charge compensation. As Fe atoms are expelled from the lattice, the stoichiometry of these NCs approach that of a nanoscale Cu-S system, and further oxidation leads to a LSPR response due to the increased density of holes in the VB. This behavior is more apparent in the extinction spectra of low-Fe bornite NCs (**Figure 3.4**c), which exhibit a LSPR band which gradually intensifies and blue-shifts upon air exposure. Such a blue-shift could conceivably be explained by increased vacancy formation in bornite NCs upon oxidation, analogous to what is known to occur in binary copper chalcogenide NCs.[21-22, 25] This will be discussed in more detail later in the text. XRD analysis of the NCs before and after these oxidative changes suggest that there was a slight shift

to higher Bragg angles for all peaks in the XRD pattern of the low-Fe bornite sample upon exposure to air for 3 weeks (**Figure 3.4**d), indicating a decrease in the lattice parameter due to the formation of copper vacancies.[45, 53] In contrast, it can clearly be seen that the lattice parameter of the high-Fe bornite NCs *increases* as the material is oxidized (**Figure 3.4**b). This *increase* in lattice parameter along with the decrease in intensity of the iron-related extinction feature, indicates oxidatively driven expulsion of iron from the high-Fe bornite NCs.

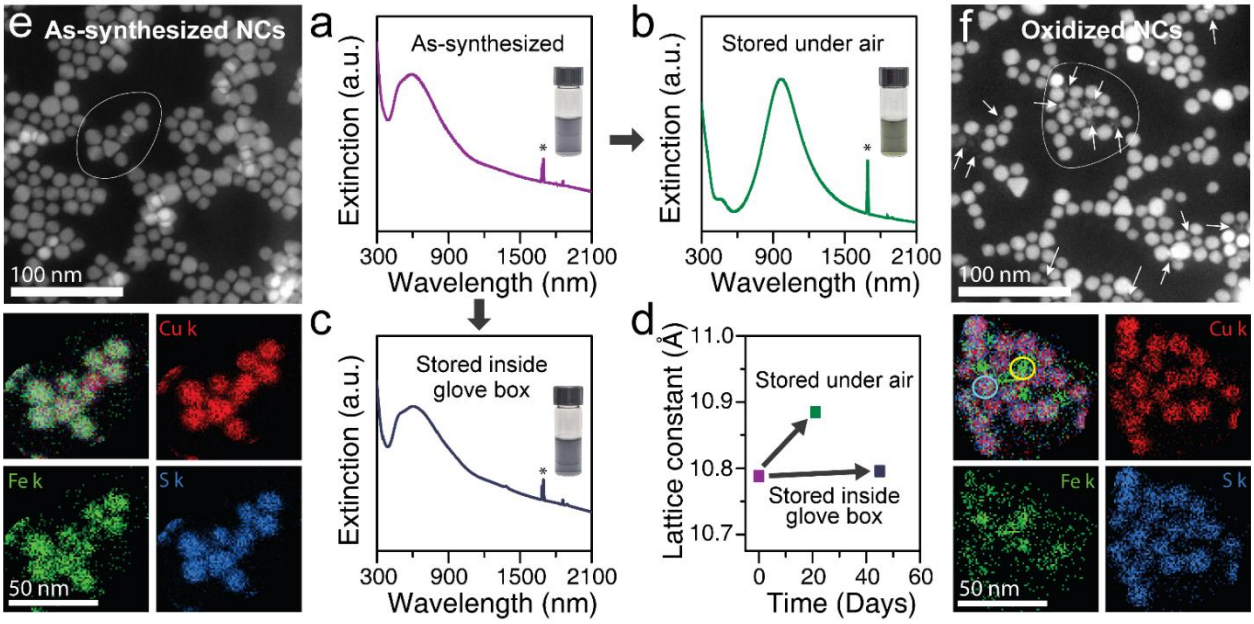

Figure 3.5. Oxidatively driven iron leaching and its influence on the optical signatures of bornite NCs. UV-vis-NIR extinction spectra of high-Fe bornite NCs: (a) as-synthesized, (b) after exposure to ambient air for 2 days, and (c) stored in a nitrogen-filled glove box for 45 days. Spectral artifacts caused by the NIR absorption bands of the chloroform solvent are marked by asterisks. Photographs of the corresponding NC dispersions are included as insets, and the lattice constants of the NCs (as determined by XRD measurements) are included in panel (d). HAADF-STEM images and elemental mapping of the (e) as-synthesized and (f) oxidized high-Fe bornite NCs. The presence of iron-rich granular matter in the oxidized NC sample (panel f) is marked by arrows, while the white encircling lines in both panels demarcate the regions on which EDXS mapping was performed. The corresponding composite and individual elemental STEM-EDXS maps are included below each panel (e and f).

The oxidation of the bornite NCs is also visually discernible, as the purple-colored dispersion of these NCs turns green upon air exposure (**Figure 3.5**, panels a and b). The drastic difference in visual appearance between the DR-exhibiting, as-synthesized (**Figure 3.5**a) and LSPR-exhibiting, air-oxidized (**Figure 3.5**b) bornite NC samples are immediately apparent, while the sample stored in an inert-atmosphere glove box shows very little change (**Figure 3.5**c) even after 45 days of storage. Likewise, the lattice parameter of the sample stored in the glove box remains unchanged, while the lattice parameter of the sample stored in air increases significantly upon oxidation (Figure 5d). This clearly demonstrates that the particles are stable under inert atmosphere and that oxidizing conditions are necessary to drive the observed spectral evolution.

Further experiments to track the oxidative changes of the high-Fe bornite NCs were then carried out using elemental mapping *via* energy-dispersive X-ray spectroscopy (EDXS), leading to additional direct evidence that elucidates the role of iron in these systems, as discussed above. Figures 5e and 5f show high-angle annular dark-field scanning TEM (HAADF-STEM) images for as-synthesized and oxidized bornite NCs, respectively. Apart from the readily discernible NCs in both images, some additional small granular matter is also immediately apparent in the oxidized NC sample (**Figure 3.5**f; arrows marking the regions of interest). EDXS mapping was then performed on a subset of the NCs in each sample (the analyzed regions are encircled by white lines in **Figure 3.5**, panels e and f) in order to establish a spatial distribution of the constituent elements. The as-synthesized high-Fe bornite NCs exhibit Cu, Fe, and S evenly distributed throughout the individual nanocrystals (**Figure 3.5**e). In contrast, while colocalization of the three elements over the NCs was still apparent after oxidation, significant leaching of iron from the NCs was clearly evident (**Figure 3.5**f). The iron signals in the EDXS maps were clearly more concentrated in the regions outside of the NCs after oxidation, revealing that the granular matter observed in the

oxidized samples is predominantly composed of iron. These observations were further corroborated by elemental analysis using inductively coupled plasma optical emission spectroscopy (ICP-OES) of the as-synthesized and oxidized high-Fe bornite NCs. After the NCs were precipitated using an anti-solvent, such that the precipitate and supernatant could be analyzed separately, larger concentrations of iron were detected in the supernatant of the oxidized sample (Table A.4).

The above results demonstrate that the diminished intensity of the extinction feature at 490 nm can be attributed to the selective expulsion of iron atoms from the bornite NCs under oxidative stress, which leads to changes in the electronic structure and dielectric response of the material, thereby altering the optical extinction characteristics. The nature of this 490-nm extinction band was further probed by testing its dependence on the refractive index of the surrounding medium. A systematic bathochromic shift of the extinction peak was observed with increasing solvent refractive index, providing additional evidence that this pronounced optical characteristic indeed arises from a Fe-3d IB-related quasi-static DR (Figure A.11), as has been demonstrated in chalcopyrite $CuFeS_2$ NCs.[10] Computational calculations of the permittivity of the bornite phases verify that the real part of their permittivity indeed turns negative in the visible frequency range as a consequence of their unique electronic structure (Figure A.12), giving rise to a quasi-static DR in nanoscale particles (see **Appendix A** for calculation details).[10]

Further evidence for the generality of the role of Fe in the resonant extinction characteristics of ternary Cu-Fe-S NCs was also demonstrated by inducing similar spectral transformations in chalcopyrite-phase $CuFeS_2$ NCs. However, since chalcopyrite NCs are much less susceptible to ambient oxidation than the bornite phase, the use of more aggressive oxidizing agents or added ions was necessary to transform the spectral characteristics of the chalcopyrite

NCs from an intense visible-frequency DR to a NIR LSPR. The colloidal chalcopyrite NCs used in these experiments were synthesized by a modified version of the procedure earlier reported by Ghosh *et al*.[5] NC purification and subsequent ion additions were performed in an inert atmosphere to eliminate effects of air exposure. Solutions of Cu(II), Cu(I), and Ce(IV) ions in methanol were added to the chalcopyrite NC solutions in small increments in screw-capped cuvettes, and the associated spectral changes were recorded (**Figure 3.6**). The aforementioned transition from an intense DR to a LSPR is immediately apparent in **Figure 3.6**a, where the spectral changes associated with the progressive addition of Cu(II) ions are shown. Since Cu(II) ions are oxidizing in nature,[54] the intensity of the DR at 490 nm diminishes due to the oxidatively driven expulsion of Fe atoms once again, while the LSPR centered at 1000 nm subsequently increases in intensity due to the formation of cation vacancies in the material. On the other hand, when Cu(I) ions are added to chalcopyrite NCs (**Figure 3.6**b), the DR similarly loses intensity due to the expulsion of Fe atoms, but subsequently, the LSPR peak appears briefly and then shifts to longer wavelengths (lower energy), eventually disappearing as the addition of Cu(I) ions is continued. This difference in evolution of the LSPR can be attributed to the replacement of holes in the NC lattice (left behind by the exiting Fe atoms) by the incoming copper atoms, when Cu(I) ions are added.[48-49] In case of Cu(II) addition described before, the oxidizing nature of $CuCl_2$ takes precedence and gives rise to the vacancy-generated LSPR signature in the chalcopyrite NCs (**Figure 3.6**a). Similar spectral signatures are also recorded when Ce(IV) ions are added to the chalcopyrite NCs (**Figure 3.6**c), where the DR loses intensity as Ce(IV) ions are progressively added. However, in this case, the significantly stronger oxidizing nature of Ce(IV) affects the NCs adversely as their concentration in solution increases, eventually leading to complete dissolution of the NCs.

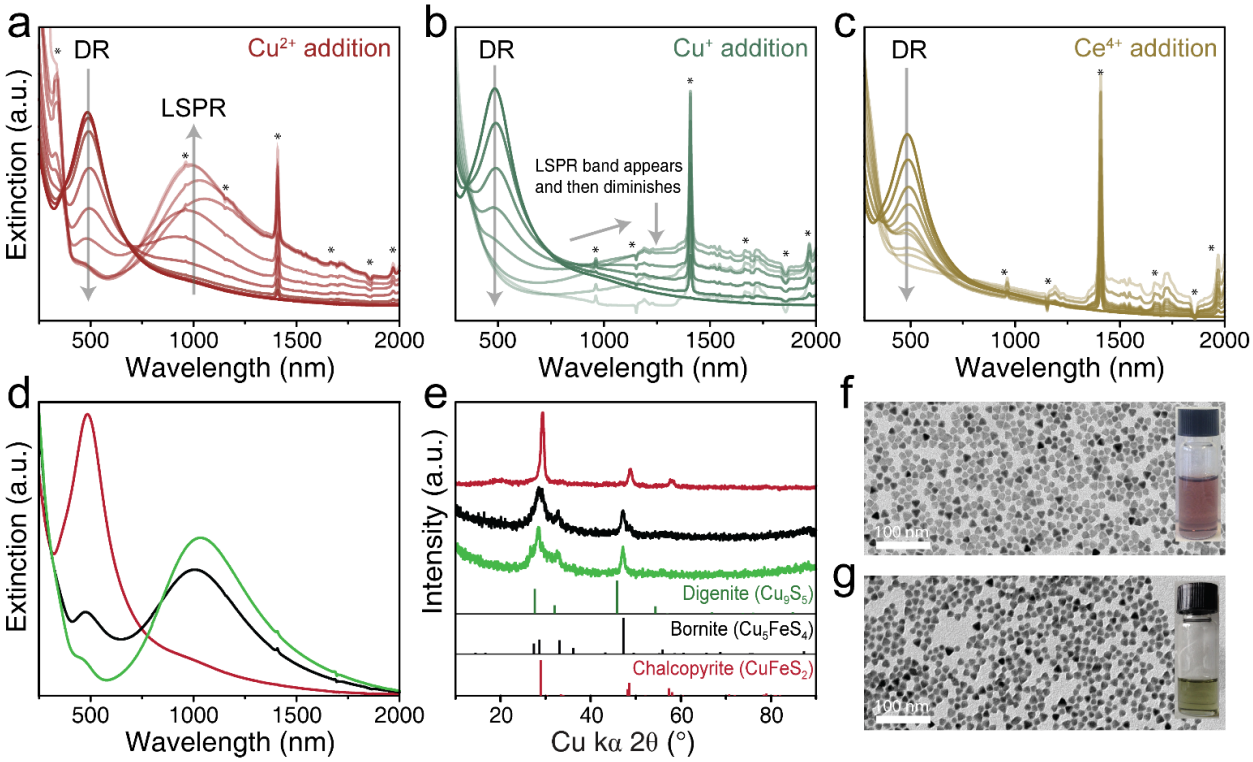

Figure 3.6. Evolution of the extinction spectra of chalcopyrite-phase $CuFeS_2$ NCs dispersed in chloroform during stepwise addition of (a) Cu(II), (b) Cu(I), and (c) Ce(IV) solutions in methanol. Spectral artifacts caused by the absorption bands of the methanol solvent are marked by asterisks. (d) Extinction spectra and (e) XRD patterns of chalcopyrite NCs oxidized to different extents by Cu(II) ions. Red, black, and green curves correspond to the as-synthesized, partially oxidized, and fully oxidized samples, respectively. Database powder XRD patterns for chalcopyrite $CuFeS_2$ (PDF #00-037-0471; red lines), bornite Cu_5FeS_4 (PDF #98-000-6587; black lines), and digenite Cu_9S_5 (PDF #01-089-2072; green lines) are included for reference. Representative TEM images of (f) as-synthesized and (g) fully oxidized NCs, with corresponding photographs of the NC dispersions included as insets.

A deeper understanding of the DR in ternary Cu-Fe-S NCs was gained through analysis of the changes in the optical and structural properties of chalcopyrite NCs upon progressive addition of Cu(II) ions (**Figure 3.6**, panels d, e, and f). The spectral responses for three samples at different stages of oxidation by Cu(II) ions are shown in **Figure 3.6**d. The as-synthesized (red curve) NCs exhibit the prominent DR at 490 nm, while the fully oxidized (green curve) NCs have a distinct

LSPR signature, and the partially oxidized (black curve) NCs display spectral responses midway between these extreme cases – *i.e.*, both DR and LSPR signatures are evident on the black curve. These NCs were further analyzed by way of XRD measurements (**Figure 3.6**e), and the diffraction pattern of the as-synthesized NCs matches with that of the bulk chalcopyrite powder XRD pattern. For the fully oxidized NCs, the diffraction pattern shows a mixture between the Fe-deficient bornite Cu-Fe-S phase (Cu_5FeS_4) and the Cu-deficient digenite Cu-S phase (Cu_9S_5). This occurrence of mixed phases in the oxidized NCs is not a surprise, since natural digenite always contains a small amount of iron and is considered to be stable only in the Cu-Fe-S system.[55] The Fe-deficiency clearly indicates Fe expulsion from the NC lattice and was further corroborated using elemental analysis on the oxidized NCs. These NCs were washed (by adding an anti-solvent like methanol), and the precipitate and supernatant were carefully collected for ICP-OES measurements. As demonstrated earlier for the bornite NCs, larger amounts of iron were detected in the supernatant, while the precipitate was found to be rich in copper and sulfur, confirming Fe-expulsion from the NC lattice. The oxidation is also visually discernible, as the color of the NC dispersion changes from purple (**Figure 3.6**f) to green (**Figure 3.6**g) upon oxidation. This controlled oxidation does not affect the morphology of these NCs, as can be appreciated from the TEM images in **Figure 3.6** panels f and g, and hence size- and shape-related factors do not influence the observed spectral changes.

The occurrence of mixed phases (Cu-Fe-S and Cu-S) in the oxidized NCs clearly explains the observation of both DR and LSPR in these systems. In fact, this is the reason why the fully oxidized NCs still show some remnant DR signature at 490 nm for both bornite (**Figure 3.5**) and chalcopyrite NCs (**Figure 3.6**). One important distinction between the DR and LSPR signatures can be drawn from the oxidation experiments of the chalcopyrite NCs described above – while the

intensity of both these spectral signatures were dependent on the level of oxidation, the position of the DR did not change during oxidative transformation, whereas the position of the LSPR did shift. This represents an important insight into the fundamental distinction between these two spectral processes – namely, that the DR in Cu-Fe-S NCs simply arises due to the unique band structure of the material and not due to vacancy doping, as is the norm in NCs of binary Cu-S phases. The LSPR signature in heavily doped semiconductor NCs, like that of vacancy-doped Cu-S NCs, is highly dependent on their charge carrier density.[56-58] Thus, both the position and intensity of the LSPR band is sensitive to oxidation and reduction of the NCs.[48-49, 56-58] For instance, the oxidation of copper chalcogenide NCs is expected to result in a blue-shifted and intensified LSPR band due to the increase in the concentration of free charge carriers (holes) by introduction of copper vacancies,[43-44, 48-49] as is also evident in this case. However, the peak position of the DR at 490 nm in the $CuFeS_2$ NCs remains unchanged upon oxidation, even after transformation of the crystal structure from chalcopyrite to bornite, while its intensity is strongly suppressed. This result, which is not in accordance with other LSPR studies on copper chalcogenide NCs,[43-45, 48] validates that the 490-nm extinction peak in chalcopyrite NCs is not attributable to collective oscillations of free charge carriers. It is rather a consequence of the quasi-static DR arising from an intermediate Fe d-band, and hence the intensity of this band decreases as Fe atoms are expelled from the NC lattice.

3.3 Summary and Conclusions

In summary, we have described a halide-assisted colloidal hot-injection synthesis of bornite NCs, which afforded both a monodisperse size distribution and compositional control, thus enabling comprehensive investigations into the influence of Fe content on the electronic structure

and optical characteristics of ternary Cu-Fe-S nanomaterials. The Fe content in these bornite NCs was varied from 4.1 to 12.5%, giving rise to two fundamentally different types of resonant excitation, with a high Fe content inducing a strong quasi-static DR extinction band centered at 490 nm, and lower-Fe-content bornite NCs exhibiting a cation-vacancy-induced LSPR signature. Moreover, it was also demonstrated that DRs in these ternary copper iron sulfide NCs can be modulated through active manipulation of their Fe content *via* oxidative methods. The tunability of the optical responses from DR to LSPR *via* the oxidative removal of Fe from the NCs was investigated in detail, proving that the presence of Fe in these NCs is closely tied to the occurrence of the IB in their electronic structure that enables a Frölich resonance condition in the visible frequency regime. These investigations entailed close monitoring of NC stoichiometry through elemental analysis and further confirmation by DFT calculations showing an associated increase in contribution to the density of states in the IB as the Fe content was increased, with HAADF-STEM elemental mapping and XRD measurements confirming that modulation of the optical response from a visible-frequency DR to a NIR LSPR can be attributed to the selective oxidation and expulsion of iron from the material. Interestingly, since both transitions occur in the visible-NIR region, they are visually discernible with the 490-nm (2.53 eV) DR inducing a purple color and the 1000-nm (1.24 eV) LSPR imparting a green color to the NC dispersion.

A similar set of transformations were observed when chalcopyrite NCs were subjected to the influence of oxidizing agents and added ions. While the as-synthesized chalcopyrite NCs exhibited the intense DR at 490 nm, strongly oxidizing conditions led to its evolution into a NIR LSPR, yielding further generality to the notion that the DR observed in nanoscale Cu-Fe-S systems is primarily due to the presence of the intermediate Fe d-band, and hence in turn, on the level of Fe incorporation in the material. The results presented here on these two Cu-Fe-S NC systems

conclusively establish that the observed DR in these systems is indeed due to their unique band structure with the Fe IB positioned just above the VB edge, enabling a negative real permittivity in the visible region. Overall, this yields a deeper understanding of the optoelectronic characteristics of ternary copper-iron-sulfide NCs and demonstrates a pathway for optical modulation in these NCs, which in turn has ramifications for the development of material systems with complex dynamic optical response.

3.4 Experimental Details

Materials: Copper (I) chloride (CuCl, 99.995%), Copper (II) chloride ($CuCl_2$, 97%), iron (III) chloride ($FeCl_3$, 97%), Sodium chloride (NaCl, ≥99.0%), Tetrakis(acetonitrile)copper(I) hexafluorophosphate (TACF, $[Cu(CH_3CN)_4]PF_6$, 97%), trioctylphosphine oxide (TOPO, 90%), oleylamine (OAM, ≥98%), oleic acid (OA, 90%), 1-octadecene (ODE, 90%), cerium (IV) ammonium nitrate (CAN, $(NH_4)_2Ce(NO_3)_6$, ≥99.99%), and chloroform (anhydrous, ≥99%) were purchased from Sigma-Aldrich. Bis(trimethylsilyl)sulfide ($S(Si(CH_3)_3)_2$, 95%), and ethanol (anhydrous, 200 proof, ≥99.5%) were obtained from Acros Organics. Methanol (Certified ACS) was purchased from Fisher Scientific. All chemicals were used as received without further purification.

Synthesis of bornite NCs: All synthetic endeavors were carried out using standard Schlenk line techniques aided by a nitrogen-filled glove box. In a typical synthesis, 0.8 mmol of copper (II) chloride (108 mg) and varying amounts of iron (III) chloride at a specified molar ratio (1:0.5, 1:0.75, 1:1, and 1:1.25) were mixed with different amounts of sodium chloride (between 0.6 and 1.8 mmol), 100 mg of TOPO, 1.2 mL of OAM, 1.2 mL of OA, and 5 mL of ODE in a three-neck round bottom flask. The mixture was heated to 100°C and degassed under vacuum for 1 h with

vigorous stirring. Then, the flask was heated to 240°C under nitrogen atmosphere and maintained at this temperature for 1 hour. Meanwhile, a sulfur precursor solution was prepared in a glove box by diluting 275 µL of bis(trimethylsilyl)sulfide with 1.23 mL of ODE. Afterwards, 1.5 mL of the sulfur precursor solution was rapidly injected into the reaction flask containing the copper and iron precursors at 240°C. The reaction temperature decreased to 225°C after the injection. The reaction proceeded at this temperature for 90 seconds, and then the flask was removed from the heating mantle to decrease the temperature to 50°C. In order to prevent solidification, 10 mL of anhydrous chloroform were added into the solution at 50°C. The NCs were washed by the addition of 7.5 mL of ethanol, followed by centrifugation at 6000 rpm (4200 RCF) for 10 minutes. Finally, the NCs were dispersed in 5 mL of anhydrous chloroform and centrifuged at 1500 rpm (260 RCF) for 1 minute to remove any poorly stabilized nanocrystals.

Synthesis of chalcopyrite NCs: This synthesis was performed using a modified version of the method previously reported by Ghosh *et al*.[5] In a three-neck round bottom flask, 0.4 mmol of copper (I) chloride (40 mg) and 0.8 mmol of iron (III) chloride (130 mg) were mixed with 100 mg of TOPO, 1.2 mL of OAM, 1.2 mL of OA, and 5 mL of ODE. The reaction mixture was degassed at 100°C for 1 hour under vacuum with vigorous stirring. Thereafter, the reaction mixture was heated to 240°C under nitrogen atmosphere. At this temperature, 225 µL of bis(trimethylsilyl)sulfide in 1 mL of ODE were rapidly injected into the flask, and the mixture was allowed to react at 220°C for 30 minutes. Subsequently, the flask was cooled to room temperature by removing the heating mantle and then 10 mL of chloroform were added at 50°C to prevent solidification of the reaction mixture. The final $CuFeS_2$ nanocrystals were purified by adding 9 mL of ethanol, followed by centrifugation at 6000 rpm (4200 RCF) for 10 minutes. Finally, the

resulting precipitate was dispersed in 5 mL of chloroform, and centrifuged again at 1500 rpm (260 RCF) for 1 minute to isolate any poorly stabilized nanocrystals.

Chemical modification of the chalcopyrite $CuFeS_2$ NCs: These experiments involved the preparation of samples in a nitrogen-filled glove box, and then subsequent measurement of spectra in 3-mL screw-capped cuvettes. The NCs were carefully handled in this inert atmosphere in order to avoid any potential effects of air exposure (*n.b.* the post-synthesis NC purification steps and subsequent ion additions were all performed inside the glove box). A typical experiment involved stepwise addition of oxidizing agents and ions directly to a cuvette containing 3 mL of $CuFeS_2$ NCs dispersed in chloroform, followed by measurement of extinction spectra after a 5-minute wait time in order to let the reaction complete prior to the next addition. The oxidizing agents (CAN and $CuCl_2$) and ions (Cu(I) complex, TACF) were prepared at a 0.01 M concentration in methanol and added in 10 µL increments. Low-volume additions were used to minimize the antisolvent effect of methanol on the NC solutions and avoid the effects of aggregation on the recorded spectra.

Computational details. Density functional theory (DFT) calculations were carried out using the Vienna ab initio simulation (VASP) package. Three different Cu-Fe-S materials of varying Fe concentration (Cu_2FeS_2, $Cu_9Fe_3S_8$, and Cu_5FeS_4) were modeled by taking a supercell approach composed of eight unit-cells in a 2x2x2 expansion. The lattice constant of the cubic supercell was set as 10.95 Å.[59] Norm-conserving pseudopotentials[60-61] and unrestricted PBE+U[62-63] were used in VASP.[64-67] A cutoff energy of 500 eV was used for the plane-wave basis. The atomic positions were optimized while keeping the lattice constant fixed on a 2x2x2 Monkhorst-Pack k-point mesh of the Brillouin zone.[68] A 6x6x6 k-point mesh was used for a subsequent density of states calculation. Further details can be found in the Supporting Information.

Transmission Electron Microscopy (TEM) analysis. Samples were prepared by dropping 15 µL of a dilute NC dispersion in chloroform on carbon-coated 200-mesh nickel TEM grids (Electron Microscopy Sciences). HRTEM, HAADF-STEM imaging, and EDXS analyses were performed at an accelerating voltage of 200 kV using a FEI Tecnai G2 F20 TEM equipped with an energy-dispersive X-ray spectroscopy detector (EDAX Element Silicon Drift Detector).

X-ray diffraction (XRD) analysis. Data collection was carried out using a Bruker D8 Discover diffractometer to determine the crystal structure of the materials. Samples were prepared by drop-casting concentrated NC dispersions onto a silicon substrate. XRD patterns were recorded using a Cu Kα X-ray source operating at 50 kV and 1000 µA.

Steady-state UV-vis-NIR extinction spectroscopy. Spectra of all NC dispersions were measured in a 1-cm-path-length quartz cuvette (Spectrocell) using either Varian Cary 60 UV-vis or Varian Cary 5000 UV-vis-NIR spectrophotometers.

Elemental analysis. Concentrations of copper, iron, and sulfur were determined by ICP-OES using a Perkin Elmer Optima 8300. NCs were digested in aqua regia prepared from ultrapure nitric acid and hydrochloric acid in a 1:3 volume ratio. Once digestion was complete overnight, samples were diluted using (18.2 MΩ) deionized water. Calibrations were performed using multi-element VII and sulfur ICP-OES standards obtained from EMD Millipore and Sigma-Aldrich, respectively.

3.5 REFERENCES

1. Vaughan, D. J.; Craig, J. R., *Mineral Chemistry of Metal Sulfides*. Cambridge University Press: 1978; p 72-155.
2. Vaughan, D. J.; Tossell, J. A., Electronic structures of sulfide minerals - Theory and experiment. *Phys. Chem. Miner.* **1983,** *9* (6), 253-262.

3. Ghosh, S.; Lu, H. C.; Cho, S. H.; Maruvada, T.; Price, M. C.; Milliron, D. J., Colloidal ReO_3 Nanocrystals: Extra Re d-Electron Instigating a Plasmonic Response. *J. Am. Chem. Soc.* **2019,** *141* (41), 16331-16343.

4. Mantella, V.; Ninova, S.; Saris, S.; Loiudice, A.; Aschauer, U.; Buonsanti, R., Synthesis and Size-Dependent Optical Properties of Intermediate Band Gap Cu_3VS_4 Nanocrystals. *Chem. Mater.* **2018,** *31* (2), 532-540.

5. Ghosh, S.; Avellini, T.; Petrelli, A.; Kriegel, I.; Gaspari, R.; Almeida, G.; Bertoni, G.; Cavalli, A.; Scotognella, F.; Pellegrino, T.; Manna, L., Colloidal $CuFeS_2$ Nanocrystals: Intermediate Fe d-Band Leads to High Photothermal Conversion Efficiency. *Chem. Mater.* **2016,** *28* (13), 4848-4858.

6. Ferretti, A.; Rogers, D. B.; Goodenough, J. B., The relation of the electrical conductivity in single crystals of rhenium trioxide to the conductivities of Sr_2MgReO_6 and Na_xWO_3. *J. Phys. Chem. Solids* **1965,** *26* (12), 2007-2011.

7. Chen, P.; Qin, M.; Chen, H.; Yang, C.; Wang, Y.; Huang, F., Cr incorporation in $CuGaS_2$ chalcopyrite: A new intermediate-band photovoltaic material with wide-spectrum solar absorption. *Phys. Status Solidi A* **2013,** *210* (6), 1098-1102.

8. Lucena, R.; Aguilera, I.; Palacios, P.; Wahnón, P.; Conesa, J. C., Synthesis and Spectral Properties of Nanocrystalline V-Substituted In_2S_3, a Novel Material for More Efficient Use of Solar Radiation. *Chem. Mater.* **2008,** *20* (16), 5125-5127.

9. Kehoe, A. B.; Scanlon, D. O.; Watson, G. W., The electronic structure of sulvanite structured semiconductors Cu_3MCh_4(M = V, Nb, Ta; Ch = S, Se, Te): prospects for optoelectronic applications. *J. Mater. Chem. C* **2015,** *3* (47), 12236-12244.

10. Gaspari, R.; Della Valle, G.; Ghosh, S.; Kriegel, I.; Scotognella, F.; Cavalli, A.; Manna, L., Quasi-Static Resonances in the Visible Spectrum from All-Dielectric Intermediate Band Semiconductor Nanocrystals. *Nano Lett.* **2017,** *17* (12), 7691-7695.

11. Avellini, T.; Soni, N.; Silvestri, N.; Fiorito, S.; De Donato, F.; De Mei, C.; Walther, M.; Cassani, M.; Ghosh, S.; Manna, L.; Stephan, H.; Pellegrino, T., Cation Exchange Protocols to Radiolabel Aqueous Stabilized ZnS, ZnSe, and $CuFeS_2$ Nanocrystals with ^{64}Cu for Dual Radio- and Photo-Thermal Therapy. *Adv. Funct. Mater.* **2020,** *30* (28), 2002362.

12. Lv, X. S.; Deng, Z. H.; Miao, F. X.; Gu, G. X.; Sun, Y. L.; Zhang, Q. L.; Wan, S. M., Fundamental optical and electrical properties of nano-Cu_3VS_4 thin film. *Opt. Mater.* **2012,** *34* (8), 1451-1454.

13. Liu, Y.; Ding, T.; Luo, X.; Li, Y.; Long, J.; Wu, K., Tuning Intermediate-Band Cu_3VS_4 Nanocrystals from Plasmonic-like to Excitonic via Shell-Coating. *Chem. Mater.* **2020,** *32* (1), 224-233.

14. Voros, M.; Galli, G.; Zimanyi, G. T., Colloidal Nanoparticles for Intermediate Band Solar Cells. *ACS Nano* **2015,** *9* (7), 6882-90.

15. Luque, A.; Martí, A.; Stanley, C., Understanding intermediate-band solar cells. *Nat. Photonics* **2012,** *6* (3), 146-152.

16. Gabka, G.; Zybała, R.; Bujak, P.; Ostrowski, A.; Chmielewski, M.; Lisowski, W.; Sobczak, J. W.; Pron, A., Facile Gram-Scale Synthesis of the First n-Type $CuFeS_2$ Nanocrystals for Thermoelectric Applications. *Eur. J. Inorg. Chem.* **2017,** *2017* (25), 3150-3153.

17. Vaure, L.; Liu, Y.; Cadavid, D.; Agnese, F.; Aldakov, D.; Pouget, S.; Cabot, A.; Reiss, P.; Chenevier, P., Doping and Surface Effects of $CuFeS_2$ Nanocrystals Used in Thermoelectric Nanocomposites. *ChemNanoMat* **2018,** *4* (9), 982-991.

18. Jiang, X.; Zhang, S.; Ren, F.; Chen, L.; Zeng, J.; Zhu, M.; Cheng, Z.; Gao, M.; Li, Z., Ultrasmall Magnetic $CuFeSe_2$ Ternary Nanocrystals for Multimodal Imaging Guided Photothermal Therapy of Cancer. *ACS Nano* **2017,** *11* (6), 5633-5645.

19. Li, B.; Yuan, F.; He, G.; Han, X.; Wang, X.; Qin, J.; Guo, Z. X.; Lu, X.; Wang, Q.; Parkin, I. P.; Wu, C., Ultrasmall $CuCo_2S_4$ Nanocrystals: All-in-One Theragnosis Nanoplatform with Magnetic Resonance/Near-Infrared Imaging for Efficiently Photothermal Therapy of Tumors. *Adv. Funct. Mater.* **2017,** *27* (10), 1606218.

20. Girma, W. M.; Tzing, S. H.; Tseng, P. J.; Huang, C. C.; Ling, Y. C.; Chang, J. Y., Synthesis of Cisplatin(IV) Prodrug-Tethered $CuFeS_2$ Nanoparticles in Tumor-Targeted Chemotherapy and Photothermal Therapy. *ACS Appl. Mater. Interfaces* **2018,** *10* (5), 4590-4602.

21. Park, J. Y.; Kim, S. J.; Chang, J. H.; Seo, H. K.; Lee, J. Y.; Yuk, J. M., Atomic visualization of a non-equilibrium sodiation pathway in copper sulfide. *Nat Commun* **2018,** *9* (1), 922.

22. Li, B.; Wang, Q.; Zou, R.; Liu, X.; Xu, K.; Li, W.; Hu, J., $Cu_{7.2}S_4$ nanocrystals: a novel photothermal agent with a 56.7% photothermal conversion efficiency for photothermal therapy of cancer cells. *Nanoscale* **2014,** *6* (6), 3274-82.

23. Liu, X.; Swihart, M. T., Heavily-doped colloidal semiconductor and metal oxide nanocrystals: an emerging new class of plasmonic nanomaterials. *Chem. Soc. Rev.* **2014,** *43* (11), 3908-20.

24. Comin, A.; Manna, L., New materials for tunable plasmonic colloidal nanocrystals. *Chem. Soc. Rev.* **2014,** *43* (11), 3957-75.

25. Coughlan, C.; Ibáñez, M.; Dobrozhan, O.; Singh, A.; Cabot, A.; Ryan, K. M., Compound Copper Chalcogenide Nanocrystals. *Chem. Rev.* **2017,** *117* (9), 5865-6109.

26. Akkerman, Q. A.; Genovese, A.; George, C.; Prato, M.; Moreels, I.; Casu, A.; Marras, S.; Curcio, A.; Scarpellini, A.; Pellegrino, T.; Manna, L.; Lesnyak, V., From Binary Cu_2S to Ternary Cu–In–S and Quaternary Cu–In–Zn–S Nanocrystals with Tunable Composition via Partial Cation Exchange. *ACS Nano* **2015,** *9* (1), 521-531.

27. Lesnyak, V.; George, C.; Genovese, A.; Prato, M.; Casu, A.; Ayyappan, S.; Scarpellini, A.; Manna, L., Alloyed Copper Chalcogenide Nanoplatelets via Partial Cation Exchange Reactions. *ACS Nano* **2014,** *8* (8), 8407-8418.

28. Wang, C.; Peng, L.; Yang, X.; Xie, R.; Feng, S., Cd-Cu-Fe-S quaternary nanocrystals exhibiting excellent optical/optoelectronic properties. *Nanoscale* **2019,** *11* (14), 6533-6537.

29. Bhattacharyya, B.; Pandey, A., $CuFeS_2$ Quantum Dots and Highly Luminescent $CuFeS_2$ Based Core/Shell Structures: Synthesis, Tunability, and Photophysics. *J. Am. Chem. Soc.* **2016,** *138* (32), 10207-13.

30. Kowalik, P.; Bujak, P.; Penkala, M.; Kotwica, K.; Kmita, A.; Gajewska, M.; Ostrowski, A.; Pron, A., Synthesis of $CuFeS_{2-x}Se_x$ – alloyed nanocrystals with localized surface plasmon resonance in the visible spectral range. *J. Mater. Chem. C* **2019,** *7* (21), 6246-6250.

31. Ghosh, S.; Gaspari, R.; Bertoni, G.; Spadaro, M. C.; Prato, M.; Turner, S.; Cavalli, A.; Manna, L.; Brescia, R., Pyramid-Shaped Wurtzite CdSe Nanocrystals with Inverted Polarity. *ACS Nano* **2015,** *9* (8), 8537-8546.

32. Zhong, H.; Lo, S. S.; Mirkovic, T.; Li, Y.; Ding, Y.; Li, Y.; Scholes, G. D., Noninjection Gram-Scale Synthesis of Monodisperse Pyramidal $CuInS_2$ Nanocrystals and Their Size-Dependent Properties. *ACS Nano* **2010,** *4* (9), 5253-5262.

33. Ghosh, S.; Manna, L., The Many "Facets" of Halide Ions in the Chemistry of Colloidal Inorganic Nanocrystals. *Chem. Rev.* **2018,** *118* (16), 7804-7864.

34. Reifsnyder, D. C.; Ye, X.; Gordon, T. R.; Song, C.; Murray, C. B., Three-Dimensional Self-Assembly of Chalcopyrite Copper Indium Diselenide Nanocrystals into Oriented Films. *ACS Nano* **2013,** *7* (5), 4307-4315.

35. Wang, X.; Swihart, M. T., Controlling the Size, Shape, Phase, Band Gap, and Localized Surface Plasmon Resonance of $Cu_{2-x}S$ and Cu_xIn_yS Nanocrystals. *Chem. Mater.* **2015,** *27* (5), 1786-1791.

36. Sungwoo Kim, M. K., Seajin Kim, Jin-Hyuk Heo, Jun Hong Noh, Sang Hyuk Im, Sang il Seok, Sang-Wook Kim, Fabrication of $CuInTe_2$ and $CuInTe_{2-x}Se_x$ Ternary Gradient Quantum Dots and Their Application to Solar Cells. *ACS Nano* **2013,** *7*, 4756-4763.

37. Bohren, C. F.; Huffman, D. R., Absorption and Scattering of Light by Small Particles. *John Wiley & Sons* **1998**, 130-157.

38. Agrawal, A.; Cho, S. H.; Zandi, O.; Ghosh, S.; Johns, R. W.; Milliron, D. J., Localized Surface Plasmon Resonance in Semiconductor Nanocrystals. *Chem. Rev.* **2018,** *118* (6), 3121-3207.

39. Comin, A.; Manna, L., New materials for tunable plasmonic colloidal nanocrystals. *Chem. Soc. Rev.* **2014,** *43* (11), 3957-3975.

40. Link, S.; El-Sayed, M. A., Spectral Properties and Relaxation Dynamics of Surface Plasmon Electronic Oscillations in Gold and Silver Nanodots and Nanorods. *J. Phys. Chem. B* **1999,** *103* (40), 8410-8426.

41. Philipp, H. R.; Ehrenreich, H., Optical Properties of Semiconductors. *Phys. Rev.* **1963,** *129* (4), 1550-1560.

42. Marton, L., Experiments on Low-Energy Electron Scattering and Energy Losses. *Rev. Mod. Phys.* **1956,** *28* (3), 172-183.

43. Jain, P. K.; Manthiram, K.; Engel, J. H.; White, S. L.; Faucheaux, J. A.; Alivisatos, A. P., Doped nanocrystals as plasmonic probes of redox chemistry. *Angew. Chem.* **2013,** *52* (51), 13671-5.

44. Luther, J. M.; Jain, P. K.; Ewers, T.; Alivisatos, A. P., Localized surface plasmon resonances arising from free carriers in doped quantum dots. *Nat. Mater.* **2011,** *10* (5), 361-6.

45. Kriegel, I.; Jiang, C.; Rodriguez-Fernandez, J.; Schaller, R. D.; Talapin, D. V.; da Como, E.; Feldmann, J., Tuning the excitonic and plasmonic properties of copper chalcogenide nanocrystals. *J. Am. Chem. Soc.* **2012,** *134* (3), 1583-90.

46. Teranishi, T.; Sato, K.; Kondo, K. i., Optical Properties of a Magnetic Semiconductor: Chalcopyrite $CuFeS_2$.: I. Absorption Spectra of $CuFeS_2$ and Fe-Doped $CuAlS_2$ and $CuGaS_2$. *J. Phys. Soc. Jpn.* **1974,** *36* (6), 1618-1624.

47. Tamio Oguchi, K. S., Teruo Teranishi, Optical Reflectivity Spectrum of a $CuFeS_2$ Single Crystal. *J. Phys. Soc. Jpn.* **1980,** *48* (1), 123-128.

48. Xie, Y.; Riedinger, A.; Prato, M.; Casu, A.; Genovese, A.; Guardia, P.; Sottini, S.; Sangregorio, C.; Miszta, K.; Ghosh, S.; Pellegrino, T.; Manna, L., Copper sulfide nanocrystals with tunable composition by reduction of covellite nanocrystals with Cu^+ ions. *J. Am. Chem. Soc.* **2013,** *135* (46), 17630-7.

49. Dorfs, D.; Hartling, T.; Miszta, K.; Bigall, N. C.; Kim, M. R.; Genovese, A.; Falqui, A.; Povia, M.; Manna, L., Reversible tunability of the near-infrared valence band plasmon resonance in $Cu_{2-x}Se$ nanocrystals. *J. Am. Chem. Soc.* **2011,** *133* (29), 11175-80.

50. Liu, H.; Shi, X.; Xu, F.; Zhang, L.; Zhang, W.; Chen, L.; Li, Q.; Uher, C.; Day, T.; Snyder, G. J., Copper ion liquid-like thermoelectrics. *Nat. Mater.* **2012,** *11* (5), 422-425.

51. Silvester, E.; Grieser, F.; Healy, T. W.; Meisel, D.; Sullivan, J. C., Thermodynamics and kinetics of the reaction of copper(II) and iron(III) with ultra-small colloidal chalcopyrite ($CuFeS_2$). *J. Chem. Soc., Faraday Trans.* **1994,** *90* (21), 3301-3307.

52. Kobayashi, H.; Onodera, H.; Kamimura, T., Electronic Properties of $CuFeS_2$ under Pressure Studied by Mössbauer Spectroscopy. *Hyperfine Interact. (C)* **2002**, 165-168.

53. Riha, S. C.; Johnson, D. C.; Prieto, A. L., Cu_2Se nanoparticles with tunable electronic properties due to a controlled solid-state phase transition driven by copper oxidation and cationic conduction. *J. Am. Chem. Soc.* **2011,** *133* (5), 1383-90.

54. Miszta, K.; Brescia, R.; Prato, M.; Bertoni, G.; Marras, S.; Xie, Y.; Ghosh, S.; Kim, M. R.; Manna, L., Hollow and Concave Nanoparticles via Preferential Oxidation of the Core in Colloidal Core/Shell Nanocrystals. *J. Am. Chem. Soc.* **2014,** *136* (25), 9061-9069.

55. Morimoto, N.; Koto, K., Phase relations of the Cu-S system at low temperatures: stability of anilite. *Am. Mineral.* **1970,** *55* (1-2), 106-117.

56. Liu, L.; Zhong, H.; Bai, Z.; Zhang, T.; Fu, W.; Shi, L.; Xie, H.; Deng, L.; Zou, B., Controllable Transformation from Rhombohedral $Cu_{1.8}S$ Nanocrystals to Hexagonal CuS Clusters: Phase- and Composition-Dependent Plasmonic Properties. *Chem. Mater.* **2013,** *25* (23), 4828-4834.

57. Faucheaux, J. A.; Stanton, A. L.; Jain, P. K., Plasmon Resonances of Semiconductor Nanocrystals: Physical Principles and New Opportunities. *J Phys Chem Lett* **2014,** *5* (6), 976-85.

58. Kriegel, I.; Scotognella, F.; Manna, L., Plasmonic Doped Semiconductor Nanocrystals: Properties, Fabrication, Applications and Perspectives. *Phys. Rep.* **2017,** *674*, 674.

59. Zhao, Q.; Yi, X.; Li, M.; Zhong, X.; Shi, Q.; Yang, K., High near-infrared absorbing Cu_5FeS_4 nanoparticles for dual-modal imaging and photothermal therapy. *Nanoscale* **2016,** *8* (27), 13368-13376.

60. Qiu, P.; Zhang, T.; Qiu, Y.; Shi, X.; Chen, L., Sulfide bornite thermoelectric material: a natural mineral with ultralow thermal conductivity. *Energy Environ. Sci.* **2014,** *7* (12), 4000-4006.

61. G. Kresse, J. H., Norm-conserving and ultrasoft pseudopotentials for first-row and transition elements. *J. Phys.: Condens. Matter* **1994,** *6*.

62. Vanderbilt, D., Soft self-consistent pseudopotentials in a generalized eigenvalue formalism. *Phys. Rev. B* **1990,** *41* (11), 7892-7895.

63. John P. Perdew; Kieron Burke; Ernzerhof, M., Generalized Gradient Approximation Made Simple. *Phys. Rev. Lett.* **1996,** *77*.

64. Cococcioni, M.; de Gironcoli, S., Linear response approach to the calculation of the effective interaction parameters in the LDA+Umethod. *Phys. Rev. B* **2005,** *71* (3).

65. Kresse, G.; Hafner, J., Ab initiomolecular dynamics for liquid metals. *Phys. Rev. B* **1993,** *47* (1), 558-561.

66. Kresse, G.; Hafner, J., Ab initiomolecular-dynamics simulation of the liquid-metal–amorphous-semiconductor transition in germanium. *Phys. Rev. B* **1994,** *49* (20), 14251-14269.

67. G. Kresse, J. F., Efficiency of ab-initio total energy calculations for metals and

semiconductors using a plane-wave basis set. *Comput. Mat. Sci.* **1996,** *6*, 15-50.

68. G. Kresse, J. F., Efficient iterative schemes for ab initio total-energy calculations using a plane-wave basis set. *Phys. Rev. B* **1996,** *54*.

69. Monkhorst, H. J.; Pack, J. D., Special points for Brillouin-zone integrations. *Phys. Rev. B* **1976,** *13* (12), 5188-5192.

Chapter 4. PHASE-CONTROLLED SYNTHESIS AND QUASI-STATIC DIELECTRIC RESONANCES IN SILVER IRON SULFIDE ($AGFES_2$) NANOCRYSTALS

4.1 INTRODUCTION

Ternary I-III-VI_2 metal chalcogenide semiconductors have been widely studied over the past few decades for a variety of applications, including photovoltaic devices,[1-3] photocatalysis,[4-5] light-emitting diodes,[6-8] and biomedical diagnostics,[9-11] because of their versatile optical properties, earth abundance, and low toxicity.[12-15] The typical representative of the I-III-VI_2 family is the ternary, copper-based chalcogenide system.[16-18] As an example, copper indium sulfide ($CuInS_2$) shows particular promise in solar energy conversion applications due to its large absorption cross section, robust photostability, and a direct band gap ($E_g \approx 1.5$ eV) that matches well with the solar spectrum.[17-19] Copper iron sulfide ($CuFeS_2$) is another important member of the I-III-VI_2 ternary semiconductors that has recently attracted considerable attention owing to its unique optical properties that exhibit a pronounced "plasmon-like" resonant absorption in the visible region, similar to that observed in metal nanocrystals (NCs).[20-22] Previous studies have shown that a strong intermediate band (IB) of states generated by empty Fe 3d orbitals in chalcopyrite $CuFeS_2$ NCs can lead to a negative permittivity in the visible region, thus enabling the occurrence of a visible-frequency, quasi-static dielectric resonance (DR).[21, 23]

Recently, several theoretical and experimental investigations have been devoted to both further understanding and practical exploitation of DR properties in IB semiconductors.[21-25] For example, Liu *et al.* showed the DR nature of copper vanadium sulfide (Cu_3VS_4) NCs on the basis of their unique spectral properties and dynamics studied using transient absorption (TA) spectroscopy.[24] To date, however, the DR has received limited attention and is rarely reported in

literature. Moreover, due to the similarity between the resultant optical characteristics of an IB-enabled DR and a localized surface plasmon resonance (LSPR), IB-enabled DRs have often been misidentified as a classic LSPR excitation.[20, 25] A better understanding of the DR properties of IB semiconductors is necessary to fully realize their potential applications. This has motivated us to study DRs in other NC systems, in this case for silver iron sulfide ($AgFeS_2$), which is likely to exhibit DR characteristics since it possesses an IB semiconductor electronic structure similar to that of $CuFeS_2$.[21, 26-27]

In this work, a facile hot-injection method for the phase-controlled synthesis of colloidal $AgFeS_2$ NCs was developed to gain additional insight into the unique optical properties of IB semiconductor NCs. We show that the crystallographic phase of the $AgFeS_2$ NCs can be tuned from the thermodynamically stable tetragonal phase to the metastable orthorhombic phase by simply adjusting the amounts of a mixed surfactants (oleic acid and oleylamine). In addition, systematic investigations demonstrate how the concentration of oleic acid (OA) and oleylamine (OAM) affects the crystal structure of the resulting $AgFeS_2$ NCs. Moreover, we provide a detailed study of the optical characteristics of $AgFeS_2$ NCs, which shows that the main absorption band is attributed to an IB-enabled DR. In analogy to the optical features of $CuFeS_2$, $AgFeS_2$ NCs exhibit resonant absorption in the ultraviolet-visible (UV-vis) spectral region and a broad shoulder in the near-infrared (NIR). Spectroscopic studies coupled with computational calculations demonstrate that the absorption peaks in the UV-vis and NIR are attributed to the occurrence of a UV-vis-frequency, IB-enabled DR and lower-energy, off-resonant excitonic transitions from the valence band (VB) to the IB, respectively.

4.2 Results and Discussion

It is well-known that ternary I-III-VI_2 semiconductors have temperature-dependent crystalline polymorphs, including tetragonal, cubic, hexagonal, and orthorhombic phases.[28-32] In general, ternary I-III-VI_2 semiconductor compounds are found to crystallize in two types of cation-ordered crystalline phases: the thermodynamically stable tetragonal/chalcopyrite phase and the metastable orthorhombic phase, which are regarded as superstructures of cubic zincblende and hexagonal wurtzite, respectively.[4, 32-35] $AgFeS_2$, which is a member of the ternary I-III-VI_2 semiconductors, can also exist in two forms: either the tetragonal or orthorhombic phase (Figure B.1). Here, colloidal $AgFeS_2$ NCs were synthesized via a hot-injection route, where a sulfur precursor solution (elemental sulfur dissolved in OAM) was rapidly injected into a hot reaction solution of silver(I) nitrate and iron(III) acetylacetonate in a mixture of dioctyl ether, OA, and OAM.

As shown in **Figure 4.1**a, the X-ray diffraction (XRD) patterns of a series of samples synthesized using different OA and OAM concentrations clearly show the effect that the amounts of the mixed surfactants has on the phase of the $AgFeS_2$ NCs. For NCs synthesized in the presence of 12.8 mmol of OA/OAM, all of the observed diffraction peaks match the expected positions for tetragonal phase $AgFeS_2$ (Lenaite, PDF# 04-013-1184). In addition, it was found that the strongest characteristic peak of tetragonal $AgFeS_2$ slightly shifts to lower diffraction angle with decreasing OA and OAM concentration. Moreover, upon decreasing the concentration of the mixed surfactants, additional peaks emerge at lower diffraction angles, which correspond to the expected reflection positions for the orthorhombic phase of a I-III-VI_2 material,[30-31, 33-36] suggesting the structural evolution from tetragonal phase to orthorhombic phase $AgFeS_2$ NCs.

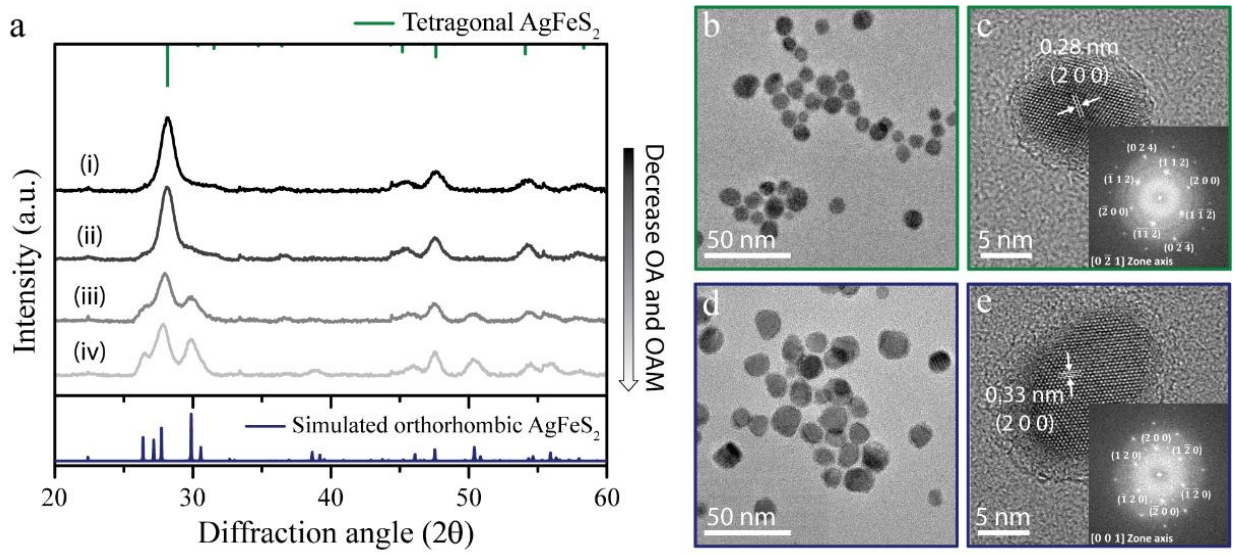

Figure 4.1. (a) XRD patterns of silver-iron-sulfide NCs synthesized with varying amounts of OA/OAM: (i) 12.8 mmol, (ii) 3.2 mmol, (iii) 0.8 mmol, and (iv) 0.4 mmol. Simulated XRD patterns of the orthorhombic phase and the standard diffraction peaks of the tetragonal phase $AgFeS_2$ (PDF# 04-013-1184) are shown for reference on the bottom and the top, respectively. TEM and HR-TEM images of representative (b, c) tetragonal and (d, e) orthorhombic phase $AgFeS_2$ NCs synthesized in the presence of 12.8 mmol and 0.4 mmol of OA/OAM, respectively. The inset shows an indexed fast Fourier transform (FFT) of an individual NC.

To verify the crystal structure of the sample synthesized with low amounts of OA and OAM, we simulated the diffraction pattern of orthorhombic $AgFeS_2$ by using lattice parameters reported in a previous study (where the lattice constants are $a = 6.56$ Å, $b = 7.87$ Å , and $c = 6.43$ Å).[37] A comparison between the simulated XRD pattern and the experimental results indicates that the experimental XRD pattern is in good agreement with the expected pattern for orthorhombic-phase $AgFeS_2$. Although there were some differences in intensity between the simulated and experimental diffraction patterns, no characteristics peaks of binary impurities

such as silver sulfide or iron sulfide were observed. The crystal structure of the resulting $AgFeS_2$ NCs was further confirmed by high-resolution transmission electron microscopy (HR-TEM) and the associate fast Fourier transform (FFT). The clear lattice fringes with interplanar spacings of 0.28 nm and 0.32 nm observed in the HR-TEM images (**Figure 4.1**, panels c and e) correspond to the (002) planes of tetragonal and orthorhombic phase $AgFeS_2$, respectively. Moreover, the corresponding FFT patterns also verify the formation of two different phases of $AgFeS_2$ NCs, which is consistent with the XRD results.

The chemical composition of the tetragonal and orthorhombic phase $AgFeS_2$ NCs was also evaluated to check for any significant differences between the samples. Energy-dispersive X-ray spectroscopy (EDXS) measurements of both phases of $AgFeS_2$ NCs reveal that the stoichiometric ratio of Ag:Fe:S is close to 1:1:2 (Table B1). While similar chemical composition is observed, TEM images clearly show the changes in size and morphology of the tetragonal and orthorhombic phase $AgFeS_2$ NCs. The tetragonal-phase $AgFeS_2$ NCs exhibit a quasi-spherical shape and relatively small particle size distributions, whereas the orthorhombic-phase $AgFeS_2$ NCs are more irregularly shaped and polydisperse with an increase in the average size, likely due to a reduction in the concentration of surfactants.

Growth mechanism of $AgFeS_2$ NCs

To rationalize the mechanism that directs the resultant phase of the NCs in this system, we first collected a series of aliquots for both representative tetragonal and orthorhombic phase $AgFeS_2$ NCs (when 12.8 mmol and 0.4 mmol of the mixed surfactants were used, respectively). Six aliquots were taken from the reaction mixture at different time intervals, with the first aliquot collected when the system had reached the target reaction temperature, but prior to injection of

the sulfur precursor solution, and the remainder being collected after the injection of the chalcogen source. **Figure 4.2** shows the phase evolution of the $AgFeS_2$ NCs, which was evaluated by collecting XRD patterns and UV-vis spectra of each aliquot. Interestingly, XRD analysis indicates that $AgFeS_2$ NC formation occurs in discrete steps, beginning with the initial formation of silver NC seeds for both of the resultant tetragonal and orthorhombic phase products. UV-vis spectra collected from the aliquots of each reaction provide additional confirmation of the presence of silver NCs prior to the injection of sulfur precursor solution by the strong Ag-NC LSPR extinction feature in the visible region (**Figure 4.2**, panels b and d). It is also important to note that that evolution of the characteristic absorption peak of the orthorhombic-phase $AgFeS_2$ NCs occurs much faster than that of the tetragonal phase. This observation implies that the formation of the metastable orthorhombic phase $AgFeS_2$ is likely due to conditions that favor faster reaction kinetics.

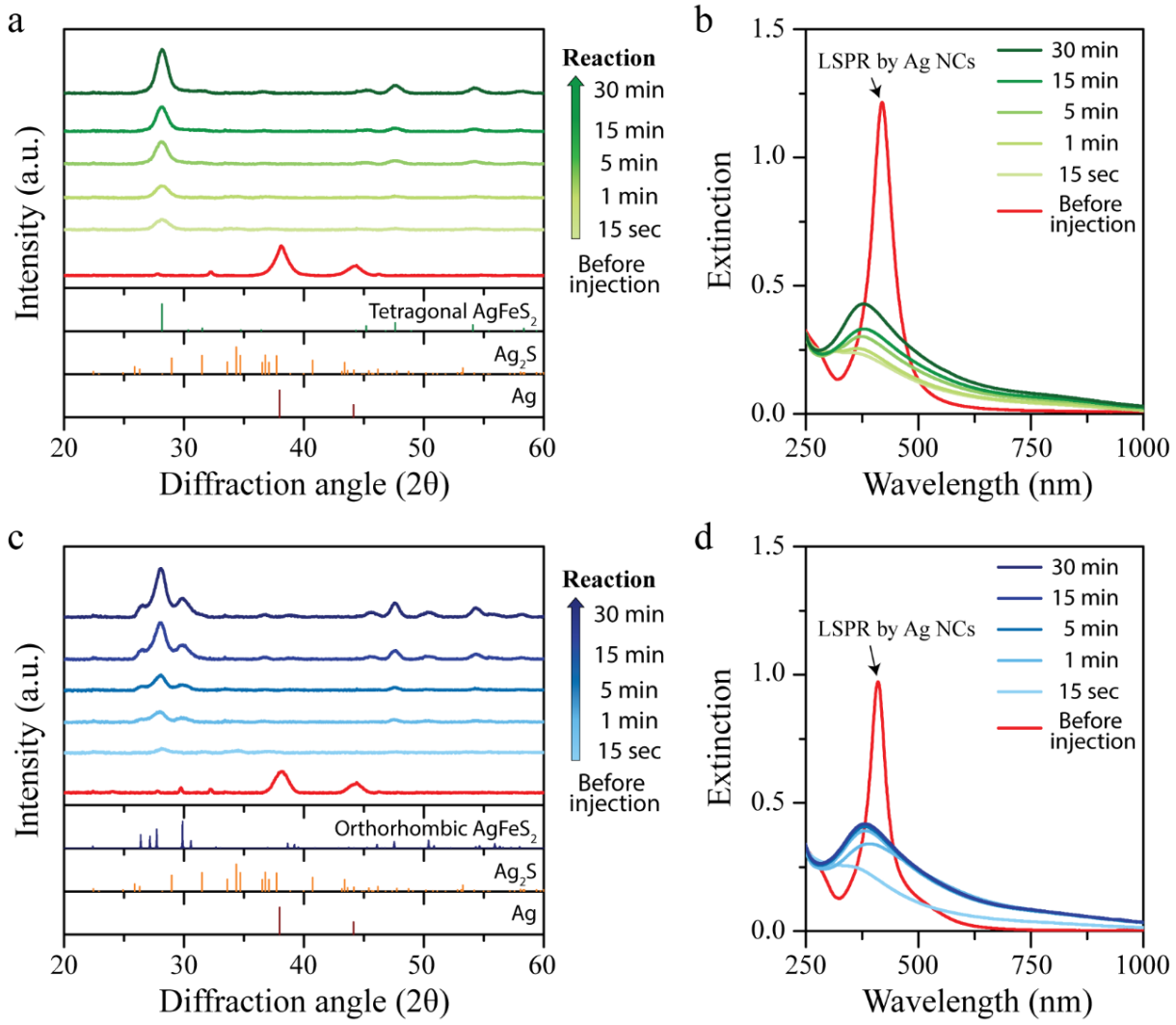

Figure 4.2. Time series of aliquots showing the formation of (a, b) tetragonal and (c, d) orthorhombic phase $AgFeS_2$ NCs monitored using XRD and UV-vis spectroscopy.

Role of oleic acid and oleylamine

In addition to the time series discussed above, several control experiments were carried out to elucidate the effect of OA/OAM concentration and its role in the phase determination of the $AgFeS_2$ NCs. For this purpose, $AgFeS_2$ NCs were synthesized in the absence of OA or OAM with varying concentrations (Figure B.6). Interestingly, when OAM is utilized as the only surfactant, we find that orthorhombic-phase $AgFeS_2$ NCs are obtained, irrespective of changes in the

surfactant concentration. In contrast, control experiments in which OA was used as the sole ligand in the synthesis revealed that $AgFeS_2$ NCs undergo a transition from orthorhombic to tetragonal phase with increasing OA concentration. This suggests that OA plays a major role in determining the crystal phase of the final product. However, it should be noted that the presence of OAM decreases the amount of OA that is required to form tetragonal phase $AgFeS_2$ NCs. Remarkably, if OA is used in combination with OAM, the concentration of OA required to trigger a phase change of the resulting $AgFeS_2$ NC product is reduced by more than 87.5% relative to the case of using OA alone.

It is well known that coordinating ligands have a great impact on precursor conversion and the reactivity of monomers in the synthesis of colloidal NCs.[38-43] In particular, OA is known to effectively coordinate to metal ions, and changing the concentration of OA in the reaction solution can greatly affect NC growth kinetics.[40-44] On the basis of the experimental results presented above, it is likely that the added excess oleic acid decreases the reactivity of the monomers, thus slowly converting the Ag NC seeds into the thermodynamically preferred tetragonal $AgFeS_2$ phase due to the reduced reaction kinetics. This is supported by a comparison with literature showing that NC growth kinetics are an important factor in guiding the preferential formation of metastable phases of binary, ternary, and quaternary metal chalcogenide NCs.[45-47]

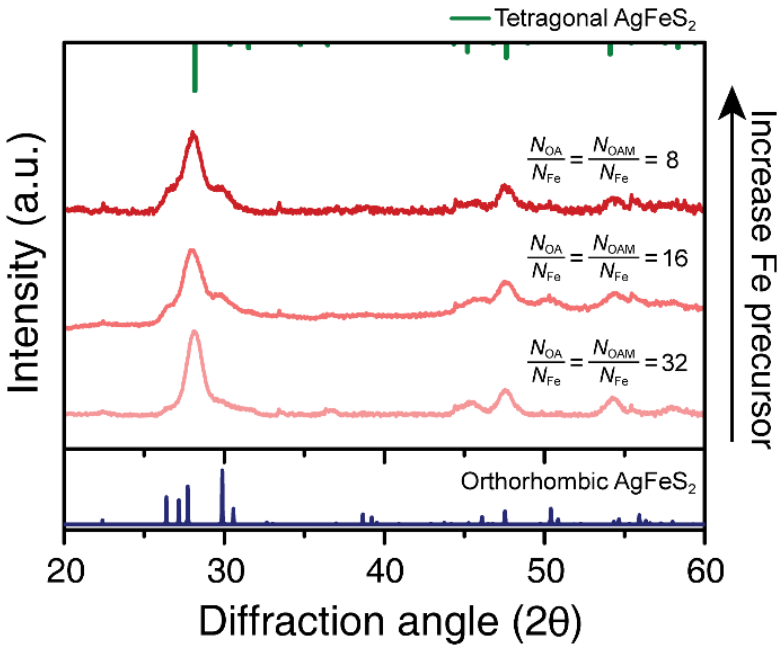

Figure 4.3. XRD patterns of $AgFeS_2$ NCs synthesized with different molar ratios of the mixed surfactants (OA+OAM) to the iron precursor by increasing the amount of $Fe(acac)_3$ while keeping the concentration of OA/OAM unchanged (3.2 mmol).

To test this further, we conducted another set of control experiments in which $AgFeS_2$ NCs were synthesized by adjusting the quantity of iron precursor while keeping the amount of OA/OAM fixed (**Figure 4.3**). In this framework, it is more appropriate to parametrize the results in terms of the molar ratio of surfactants to iron precursor ($N_{surfactants}/N_{Fe}$), as opposed to the concentration of surfactants. Changing the molar ratio of surfactants to iron precursor indicated that a decrease in the molar ratio of $N_{surfactants}/N_{Fe}$ could also aid in the formation of the metastable orthorhombic-phase $AgFeS_2$ NCs. This suggests that addition of the iron precursor further facilitates the growth of $AgFeS_2$ NCs, which in turn facilitates a kinetically favored reaction. Therefore, it can be concluded that the crystal phase of the final $AgFeS_2$ product is dictated by controlling the growth rate of the NCs.

Moreover, in this respect, a possible OA/OAM cooperative effect in the final crystal structure of $AgFeS_2$ NCs can be explained by considering the adjuvant role of OAM in promoting the deprotonation of OA.[48-50] Negatively charged, deprotonated carboxylate anions ($C_{17}H_{33}COOH^-$), which possess considerable electron-donating ability in the reaction system,[48-50] could then effectively inhibit rapid $AgFeS_2$ NC growth by strong chemical bonding to both the precursors and the NCs. Therefore, when OA and OAM were used equimolarly as a mixture of surfactants, the thermodynamically favored tetragonal phase $AgFeS_2$ NCs could be preferentially synthesized with only a small amount of OA. Finally, **Figure 4.4** schematically depicts the phase-selective growth mechanism of $AgFeS_2$ NCs with varying concentrations of OA/OAM.

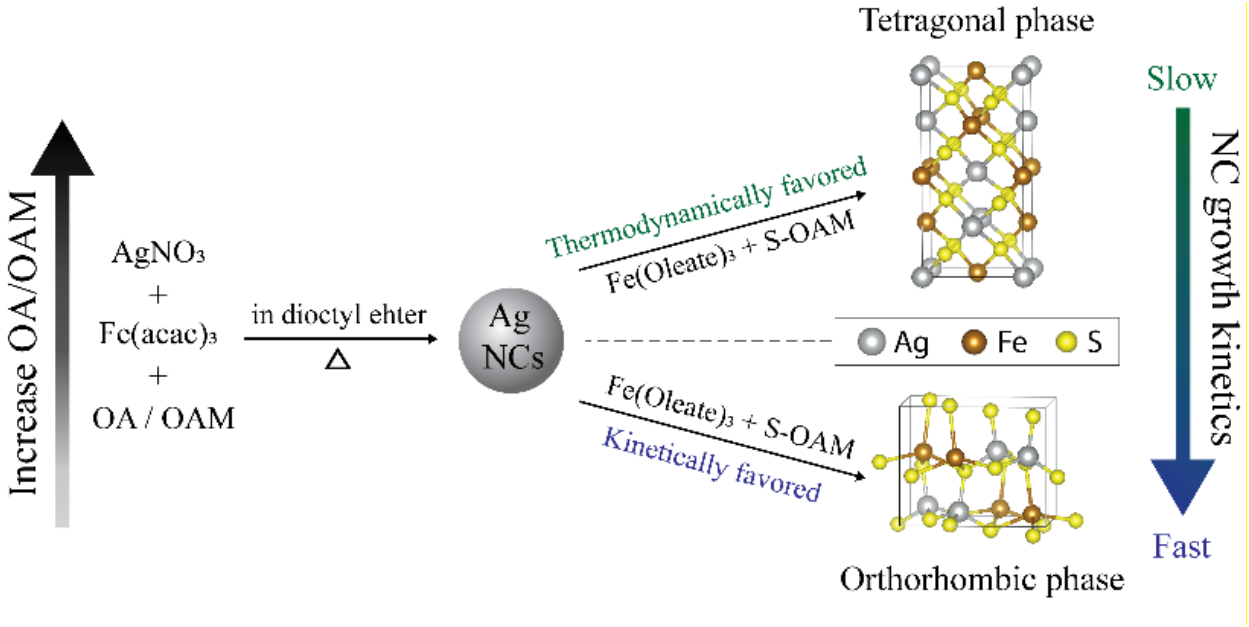

Figure 4.4. A schematic illustration of the phase-controlled synthesis of tetragonal and orthorhombic $AgFeS_2$ NCs, depending on the concentration of OA/OAM.

Optical properties of $AgFeS_2$ NCs

Figure 4.5a shows the UV-vis-NIR extinction spectra of the tetragonal and orthorhombic phase $AgFeS_2$ NCs. Both phases of $AgFeS_2$ NCs exhibit a distinct, intense absorption peak at 380 nm, along with broad absorption in the NIR region, which is analogous to what is observed in chalcopyrite $CuFeS_2$ NCs. As discussed in the introduction, it has been demonstrated that the occurrence of visible-frequency DRs in ternary Cu-Fe-S systems is attributed to a negative permittivity in the visible range, resulting in resonant, IB-enabled excitations.[21, 26-27] Considering that $AgFeS_2$ is known to be an IB semiconductor, the spectral similarities with $CuFeS_2$ NCs imply that the strong extinction features of $AgFeS_2$ NCs could also be due to resonant absorption enabled by the occurrence of an IB-enabled DR.

To identify the nature of the resonant extinction features observed in $AgFeS_2$ NCs, we investigated the influence of the dielectric permittivity of the medium surrounding the NCs on the position of the observed absorption peak (Figure B.5). The results clearly show that the maximum absorption peak of both phases of $AgFeS_2$ NCs continuously redshifts with an increasing solvent refractive index, as expected for the characteristics of either an IB-enabled DR or an LSPR, due to the related shifts in the Frölich resonance frequency that occur with increases to the permittivity of the surrounding medium.[21, 23] Although the resultant extinction features of an IB-enabled DR appear similar in nature to the typical resonance features of plasmonic NCs, it should be noted that absorption through an IB-enabled DR occurs via resonant VB-IB excitation, as opposed to the resonant excitation of the free charge carriers present in materials that exhibit LSPRs. Since $AgFeS_2$ NCs are all-dielectric in nature and have no ground-state free charge carriers to support an LSPR, it is thus inferred that the strong absorption peak of $AgFeS_2$ NCs arises from excitation

of an IB-enabled, quasi-static DR. This interpretation is also supported by the immediate disappearance of the Ag NC seed LSPR upon injection of the sulfur precursor.

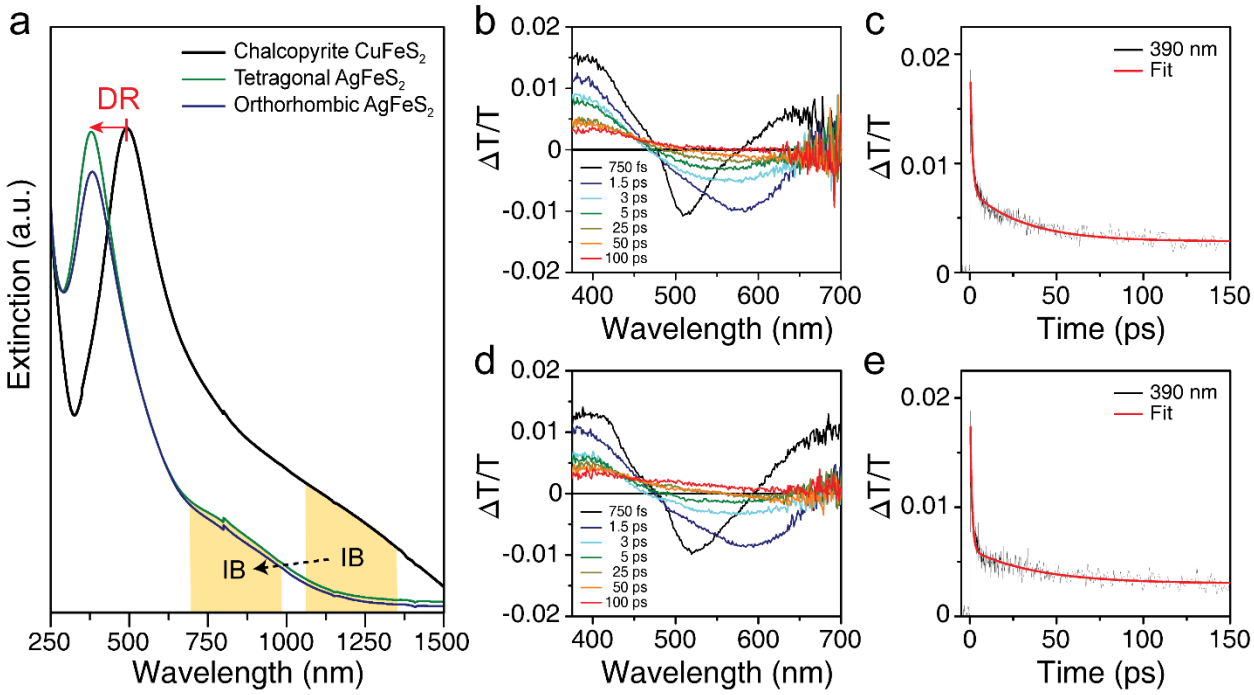

Figure 4.5. (a) UV-vis-NIR extinction spectra of the as-synthesized tetragonal and orthorhombic phase $AgFeS_2$ NCs dispersed in chloroform, in comparison with colloidal chalcopyrite $CuFeS_2$ NCs. (b, d) Transient absorption spectra of tetragonal and orthorhombic phase $AgFeS_2$ NCs at different time delays after photoexcitation by 365 nm pump pulses. (c, e) Decay dynamics of tetragonal and (d) orthorhombic phase $AgFeS_2$ NCs at 390 nm.

Further analysis of the optoelectronic characteristics of the $AgFeS_2$ NCs was performed using transient absorption (TA) measurements (See **Appendix B** for details). TA spectra of tetragonal and orthorhombic phase $AgFeS_2$ NCs after photoexcitation at 365 nm show similar spectroscopic features as those observed in $CuFeS_2$ IB NCs: A strong bleach signature at around 390 nm, which is in-line with the spectral range of the DR, and a broad photoinduced absorption at longer wavelengths. The time-dependent evolution of the TA spectra further highlights this

analogy (**Figure 4.5**, panels b and d). Moreover, analogous with the DR relaxation dynamics of $CuFeS_2$ NCs, the decay dynamics of $AgFeS_2$ NCs at the bleach maximum are well described by a biexponential fit with a fast decay within the first few picoseconds followed by a slower decay on the time scale of several tens of picoseconds.[21] Given the similarity between the TA features of $AgFeS_2$ and $CuFeS_2$ NCs, the bleach is attributable to the excitation-induced damping and broadening of the DR caused by scattering between the photoexcited charge carriers with phonons and defects.[21] In addition, the photoinduced absorption feature on the lower energy side of the DR bleach can be ascribed to further interband transitions from the IB to the conduction band (CB).[51]

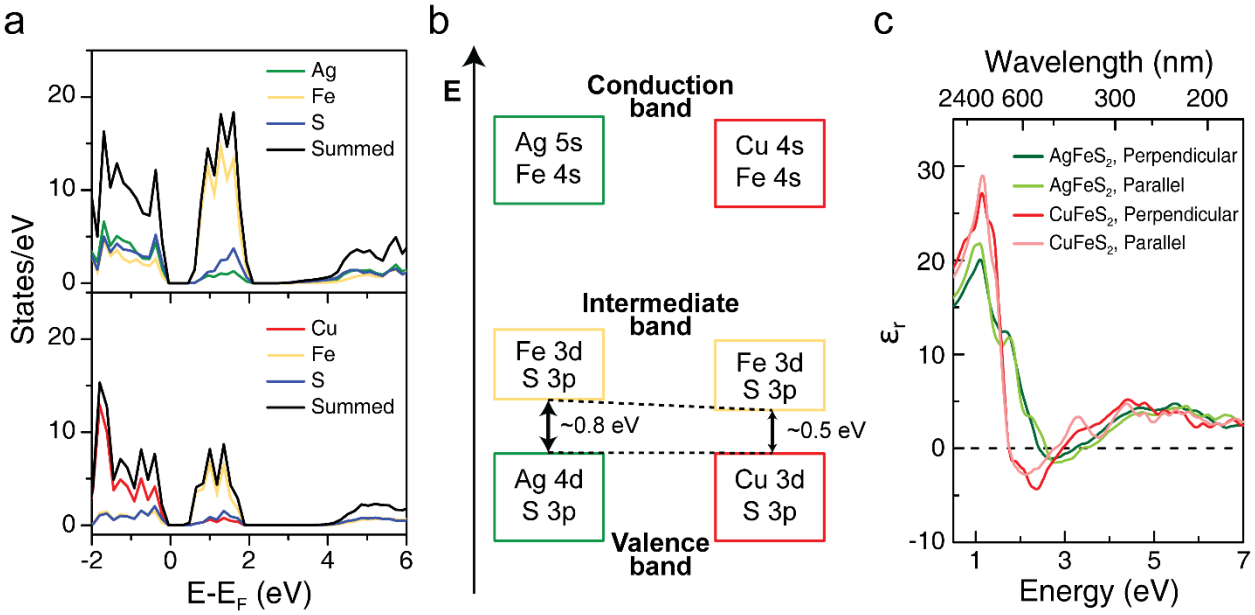

Figure 4.6. Computed DOS of tetragonal/chalcopyrite $AgFeS_2$ and $CuFeS_2$. Green, yellow, blue, and red lines correspond to the projection of the DOS on the Ag, Fe, S, and Cu atoms, respectively. (b) Schematic diagram of the band structure of $AgFeS_2$ and $CuFeS_2$. (c) Comparison of the calculated real component of the permittivity for $AgFeS_2$ and $CuFeS_2$.

Despite the similarity between the optical properties of $AgFeS_2$ and $CuFeS_2$ NCs, it should be noted the peak absorption features occur at significantly higher energies in the $AgFeS_2$ NC

system. As pointed out by Gaspari *et al.*, previous computational work showed that the dielectric responses of IB semiconductors should be strongly influenced by the position of the IB within the VB-CB gap.[21] Thus, the observed shift in spectral features to higher energies can likely be attributed to changes in the dielectric function that result from the electronic structure of $AgFeS_2$. To gain more insight into the observed DR absorption and further interpret the UV-vis-NIR measurements, the electronic structure of tetragonal and orthorhombic phase $AgFeS_2$ were investigated using density functional theory (DFT) calculations (**Figure 4.6**a).

By comparison of the calculated electronic structures for chalcopyrite/tetragonal phase $CuFeS_2$ and $AgFeS_2$, it can be seen that the distance between the VB and IB increases from 0.53 eV for $CuFeS_2$ to 0.83 eV for $AgFeS_2$. Moreover, computational calculations of the real component of the permittivity for each system clearly indicates that the region of negative permittivity indeed shifts to higher energy as a result of the change in separation between the VB and IB (**Figure 4.6**c). Thus, the resulting blue-shift of the DR band to higher energy for the $AgFeS_2$ NC system is consistent with previous theoretical understanding.[23] Taken together with the observed spectroscopic data, the computational calculations further confirm the nature of the IB-enabled DR excitation in $AgFeS_2$ NCs.

4.3 Summary and Conclusions

In summary, we have investigated the phase-controlled synthesis and resonant optical characteristics of $AgFeS_2$ IB semiconductor NCs. It was found that the concentration of coordinating ligands plays a significant role in determining the final crystal structure of the $AgFeS_2$ NCs. Comprehensive mechanistic studies reveal that increasing concentrations of the mixed OA and OAM coordinating surfactants in the reaction solution result in decreased precursor reactivity,

resulting in the formation of the thermodynamically favored tetragonal phase $AgFeS_2$. Additionally, control experiments conducted using solely OA or OAM as the ligand provided additional insight into their individual roles in the phase-controlled synthesis of $AgFeS_2$.

Moreover, it was also demonstrated that $AgFeS_2$ NCs exhibit a strong quasi-static DR extinction band centered at 380 nm, and a weaker absorption onset in the NIR region that occurs due to off-resonant interband transitions from the VB to the IB, in analogy to what has been observed in chalcopyrite copper iron sulfide NCs. TA measurements along with DFT calculations showed that the strong optical resonance in $AgFeS_2$ NCs is attributed to the occurrence of a DR enabled by a negative permittivity in the UV-vis range that results from the unique IB electronic structure of the material. In addition to expanding the current library of IB semiconductor NCs that exhibit DR excitation, our study constitutes the first combined experimental-computational demonstration showing how the IB electronic structure effects shifts in the DR frequency. Overall, these findings shed more light on the DR characteristics of ternary metal iron sulfide NCs, which may serve as important insight for future applications of these materials.

4.4 Experimental Details

Materials

Silver nitrate ($AgNO_3$, 99.9999%), copper (I) iodide (CuI, 99.999%), iron (III) acetylacetonate ($Fe(acac)_3$, ≥ 99.9%), sulfur powder (S, 99.998%), Dioctyl ether (99%), oleylamine (OAM, ≥98%), oleic acid (OA, 90%), and chloroform (anhydrous, ≥99%) were obtained from Sigma-Aldrich. 2-propanol (Certified ACS Plus), and methanol (certified ACS) were obtained from Fisher Scientific. Ethanol (anhydrous, 200 proof, ≥99.5%) were purchased from Decon Laboratories. All chemicals were used as received without further purification.

Preparation of Oleylamine-Sulfur precursor complex

Sulfur precursor solution was prepared by dissolving 2 mmol of S powder (64 mg) in 2.5 mL of OAM at 120°C for 30min under nitrogen atmosphere. The solution was then cooled to 50°C for further use.

Synthesis of Silver Iron Sulfide ($AgFeS_2$) NCs

Silver iron sulfide NCs were synthesized following some modifications of a previous reported protocol.[37] In a typical procedure, 0.1 mmol of silver nitrate (17 mg) and 0.1 mmol of iron (III) acetylacetonate (35.3 mg) were mixed with 10 mL of dioctyl ether, and varying amounts of oleic aicd and oleylamine (between 0.4 and 12.8 mmol) in a three neck round bottom flask. The reaction mixture was degassed at 90°C for 1hr under vacuum with vigorous stirring. After degassing, the reaction mixture was heated to 180°C under nitrogen atmosphere. Subsequently, 0.5 mL of the 0.8M OAm-S precursor solution was rapidly injected, and the mixture was allowed to react at 180°C for 30min. Then, the flask was cooled down to room temperature by removing the heating mantle. The final $AgFeS_2$ Nanocrystals were precipitated by adding 10mL of isopropanol and 5mL of methanol, followed by centrifugation at 6,000 rpm (4200 RCF) for 10min. Finally, the resultant precipitate was dispersed in 5mL of chloroform, and washed twice with chloroform and ethanol to clean the sample thoroughly.

Synthesis of Chalcopyrite Copper Iron Sulfide ($CuFeS_2$) NCs

In a three-neck round bottom flask, 0.1 mmol of copper (I) iodide (19 mg) and 0.1 mmol of iron (III) acetylacetonate (35.3 mg) were mixed with 10 mL of dioctyl ether, 1.2 mL of OA, and 1.2 mL of OAM. The reaction mixture was degassed at 90°C for 1 hour under vacuum with vigorous stirring. Thereafter, the reaction mixture was heated to 180°C under nitrogen atmosphere. At this temperature, 0.5 mL of the 0.8M OAm-S precursor solution was rapidly injected into the flask,

and the mixture was allowed to react at 180°C for 30 minutes. Subsequently, the flask was cooled to room temperature by removing the heating mantle. The final $CuFeS_2$ nanocrystals were purified by adding 10 mL of ethanol, followed by centrifugation at 6000 rpm (4200 RCF) for 10 minutes. Finally, the resulting precipitate was dispersed in 5 mL of chloroform.

X-ray Diffraction (XRD) Analysis

XRD analysis were performed using a Bruker D8 Discover diffractometer with a Cu Kα X-ray source operating at 50 kV and 1000 μA. XRD samples were prepared by drop-casting concentrated NC dispersions on a clean silicon wafer.

Transmission Electron Microscopy (TEM) Analysis

TEM images were taken on a FEI Tecnai G2 F20 transmission electron microscope operating at an accelerating voltage of 200 kV. Samples were prepared by drop-casting a diluted NC dispersion in chloroform onto carbon-coated 200 mesh nickel grids (Electron Microscopy Sciences). Additional energy dispersive X-ray spectroscopy (EDXS) was carried out using an X-ray energy-dispersive spectroscopy detector (EDAX Element Silicon Drift Detector) to analyze the chemical composition of the nanocrystals.

UV-vis-NIR Spectroscopy

Extinction spectra of all NC dispersions were measured in a quartz cuvette (Spectrocell) with an optical path length of 10 mm using either Varian Cary 60 UV-vis or Varian Cary 5000 UV-vis-NIR spectrophotometers.

Transient Absorption (TA) Spectroscopy

Transient absorption measurements were performed using the 365 nm output of an optical parametric amplifier (Coherent/Light Conversion OPerA Solo) that was pumped with 50 fs pulses

from a 1 kHz Ti:sapphire laser system (Coherent, Libra-HE). White-light supercontinuum probe pulses (~200 fs) were generated by focusing a portion of the Ti:sapphire output onto a sapphire plate. Spectra were collected with a complementary metal-oxide semiconductor (CMOS) sensor and InGaAs fiber-coupled multichannel photodiode array spectrometer. The excitation energy per pulse was kept in the linear regime at around 320 nJ and the pump pulses were focused in a 300 μm diameter spot. Surface Xplorer software (Ultrafast Systems) was used to collect and process spectra. All measurements were conducted at room temperature on the chloroform dispersions of $AgFeS_2$ NCs in a 2 mm path length quartz cuvette prepared under nitrogen atmosphere.

4.5 REFERENCES

1. Guo, Q.; Kim, S. J.; Kar, M.; Shafarman, W. N.; Birkmire, R. W.; Stach, E. A.; Agrawal, R.; Hillhouse, H. W., Development of $CuInSe_2$ Nanocrystal and Nanoring Inks for Low-Cost Solar Cells. *Nano Letters* **2008,** *8* (9), 2982-2987.

2. Panthani, M. G.; Akhavan, V.; Goodfellow, B.; Schmidtke, J. P.; Dunn, L.; Dodabalapur, A.; Barbara, P. F.; Korgel, B. A., Synthesis of $CuInS_2$, $CuInSe_2$, and $Cu(In_xGa_{1-x})Se_2$ (CIGS) Nanocrystal "Inks" for Printable Photovoltaics. *Journal of the American Chemical Society* **2008,** *130* (49), 16770-16777.

3. Santra, P. K.; Nair, P. V.; George Thomas, K.; Kamat, P. V., $CuInS_2$-Sensitized Quantum Dot Solar Cell. Electrophoretic Deposition, Excited-State Dynamics, and Photovoltaic Performance. *The Journal of Physical Chemistry Letters* **2013,** *4* (5), 722-729.

4. Fan, C.-M.; Regulacio, M. D.; Ye, C.; Lim, S. H.; Zheng, Y.; Xu, Q.-H.; Xu, A.-W.; Han, M.-Y., Colloidal synthesis and photocatalytic properties of orthorhombic $AgGaS_2$ nanocrystals. *Chemical Communications* **2014,** *50* (54), 7128-7131.

5. Zhao, M.; Huang, F.; Lin, H.; Zhou, J.; Xu, J.; Wu, Q.; Wang, Y., $CuGaS_2$–ZnS p–n nanoheterostructures: a promising visible light photo-catalyst for water-splitting hydrogen production. *Nanoscale* **2016,** *8* (37), 16670-16676.

6. Song, W.-S.; Kim, J.-H.; Lee, J.-H.; Lee, H.-S.; Do, Y. R.; Yang, H., Synthesis of color-tunable Cu–In–Ga–S solid solution quantum dots with high quantum yields for application to white light-emitting diodes. *Journal of Materials Chemistry* **2012,** *22* (41), 21901-21908.

7. Chuang, P.-H.; Lin, C. C.; Liu, R.-S., Emission-Tunable $CuInS_2$/ZnS Quantum Dots: Structure, Optical Properties, and Application in White Light-Emitting Diodes with High Color Rendering Index. *ACS Applied Materials & Interfaces* **2014,** *6* (17), 15379-15387.

8. Park, S. H.; Hong, A.; Kim, J.-H.; Yang, H.; Lee, K.; Jang, H. S., Highly Bright Yellow-Green-Emitting $CuInS_2$ Colloidal Quantum Dots with Core/Shell/Shell Architecture for White Light-Emitting Diodes. *ACS Applied Materials & Interfaces* **2015,** *7* (12), 6764-6771.

9. Li, L.; Daou, T. J.; Texier, I.; Kim Chi, T. T.; Liem, N. Q.; Reiss, P., Highly Luminescent $CuInS_2$/ZnS Core/Shell Nanocrystals: Cadmium-Free Quantum Dots for In Vivo Imaging. *Chemistry of Materials* **2009,** *21* (12), 2422-2429.

10. Cassette, E.; Pons, T.; Bouet, C.; Helle, M.; Bezdetnaya, L.; Marchal, F.; Dubertret, B., Synthesis and Characterization of Near-Infrared Cu−In−Se/ZnS Core/Shell Quantum Dots for In vivo Imaging. *Chemistry of Materials* **2010,** *22* (22), 6117-6124.

11. Regulacio, M. D.; Win, K. Y.; Lo, S. L.; Zhang, S.-Y.; Zhang, X.; Wang, S.; Han, M.-Y.; Zheng, Y., Aqueous synthesis of highly luminescent $AgInS_2$–ZnS quantum dots and their biological applications. *Nanoscale* **2013,** *5* (6), 2322-2327.

12. Allen, P. M.; Bawendi, M. G., Ternary I−III−VI Quantum Dots Luminescent in the Red to Near-Infrared. *Journal of the American Chemical Society* **2008,** *130* (29), 9240-9241.

13. Xie, R.; Rutherford, M.; Peng, X., Formation of High-Quality I−III−VI Semiconductor Nanocrystals by Tuning Relative Reactivity of Cationic Precursors. *Journal of the American Chemical Society* **2009,** *131* (15), 5691-5697.

14. Chen, B.; Pradhan, N.; Zhong, H., From Large-Scale Synthesis to Lighting Device Applications of Ternary I–III–VI Semiconductor Nanocrystals: Inspiring Greener Material Emitters. *The Journal of Physical Chemistry Letters* **2018,** *9* (2), 435-445.

15. Regulacio, M. D.; Han, M.-Y., Multinary I-III-VI_2 and I_2-II-IV-VI_4 Semiconductor Nanostructures for Photocatalytic Applications. *Accounts of Chemical Research* **2016,** *49* (3), 511-519.

16. Coughlan, C.; Ibáñez, M.; Dobrozhan, O.; Singh, A.; Cabot, A.; Ryan, K. M., Compound Copper Chalcogenide Nanocrystals. *Chemical Reviews* **2017,** *117* (9), 5865-6109.

17. Kolny-Olesiak, J.; Weller, H., Synthesis and Application of Colloidal $CuInS_2$ Semiconductor Nanocrystals. *ACS Applied Materials & Interfaces* **2013,** *5* (23), 12221-12237.

18. Meinardi, F.; McDaniel, H.; Carulli, F.; Colombo, A.; Velizhanin, K. A.; Makarov, N. S.; Simonutti, R.; Klimov, V. I.; Brovelli, S., Highly efficient large-area colourless luminescent solar concentrators using heavy-metal-free colloidal quantum dots. *Nature Nanotechnology* **2015,** *10* (10), 878-885.

19. Jara, D. H.; Yoon, S. J.; Stamplecoskie, K. G.; Kamat, P. V., Size-Dependent Photovoltaic Performance of $CuInS_2$ Quantum Dot-Sensitized Solar Cells. *Chemistry of Materials* **2014,** *26* (24), 7221-7228.

20. Sugathan, A.; Bhattacharyya, B.; Kishore, V. V. R.; Kumar, A.; Rajasekar, G. P.; Sarma, D. D.; Pandey, A., Why Does $CuFeS_2$ Resemble Gold? *The Journal of Physical Chemistry Letters* **2018,** *9* (4), 696-701.

21. Gaspari, R.; Della Valle, G.; Ghosh, S.; Kriegel, I.; Scotognella, F.; Cavalli, A.; Manna, L., Quasi-Static Resonances in the Visible Spectrum from All-Dielectric Intermediate Band Semiconductor Nanocrystals. *Nano Letters* **2017,** *17* (12), 7691-7695.

22. Avellini, T.; Soni, N.; Silvestri, N.; Fiorito, S.; De Donato, F.; De Mei, C.; Walther, M.; Cassani, M.; Ghosh, S.; Manna, L.; Stephan, H.; Pellegrino, T., Cation Exchange Protocols to Radiolabel Aqueous Stabilized ZnS, ZnSe, and $CuFeS_2$ Nanocrystals with ^{64}Cu for Dual Radio- and Photo-Thermal Therapy. *Advanced Functional Materials* **2020,** *30* (28), 2002362.

23. Lee, S.; Ghosh, S.; Hoyer, C. E.; Liu, H.; Li, X.; Holmberg, V. C., Iron-Content-Dependent, Quasi-Static Dielectric Resonances and Oxidative Transitions in Bornite and Chalcopyrite Copper Iron Sulfide Nanocrystals. *Chemistry of Materials* **2021,** *33* (5), 1821-1831.

24. Liu, Y.; Ding, T.; Luo, X.; Li, Y.; Long, J.; Wu, K., Tuning Intermediate-Band Cu_3VS_4 Nanocrystals from Plasmonic-like to Excitonic via Shell-Coating. *Chemistry of Materials* **2020,** *32* (1), 224-233.

25. Yao, Y.; Bhargava, A.; Robinson, R. D., Fe Cations Control the Plasmon Evolution in $CuFeS_2$ Nanocrystals. *Chemistry of Materials* **2021,** *33* (2), 608-615.

26. Djaafri, T.; Bouafia, H.; Sahli, B.; Djebour, B.; Uğur, Ş.; Uğur, G.; Moussa, H., Study of the ground-state magnetic ordering, magnetic and optoelectronic properties of (Lenaite) $AgFeS_2$ in its chalcopyrite structure. *Journal of Magnetism and Magnetic Materials* **2020,** *493*, 165730.

27. Peng, X.; Liu, J.; Ming, C.; Li, B.; Zhao, Z.; Ye, K.; Zeng, M.; Zou, R.; Lu, X.; Hu, J., $AgFeS_2$ nanoparticles as a novel photothermal platform for effective artery stenosis therapy. *Nanoscale* **2020,** *12* (20), 11288-11296.

28. Shay, J. L.; Tell, B.; Schiavone, L. M.; Kasper, H. M.; Thiel, F., Energy bands of $AgInS_2$ in the chalcopyrite and orthorhombic structures. *Physical Review B* **1974,** *9* (4), 1719-1723.

29. Binsma, J. J. M.; Giling, L. J.; Bloem, J., Phase relations in the system Cu_2S-In_2S_3. *Journal of Crystal Growth* **1980,** *50* (2), 429-436.

30. Krustok, J.; Raudoja, J.; Krunks, M.; Mändar, H.; Collan, H., Nature of the native deep localized defect recombination centers in the chalcopyrite and orthorhombic $AgInS_2$. *Journal of Applied Physics* **2000,** *88* (1), 205-209.

31. Cholula-Díaz, J. L.; Wagner, G.; Friedrich, D.; Oeckler, O.; Krautscheid, H., Synthesis of $CuInS_2$ nanocrystals from a molecular complex – characterization of the orthorhombic domain structure. *Dalton Transactions* **2015,** *44* (32), 14227-14234.

32. Qi, Y.; Liu, Q.; Tang, K.; Liang, Z.; Ren, Z.; Liu, X., Synthesis and Characterization of Nanostructured Wurtzite $CuInS_2$: A New Cation Disordered Polymorph of $CuInS_2$. *The Journal of Physical Chemistry C* **2009,** *113* (10), 3939-3944.

33. Bai, T.; Xing, S.; Li, C.; Shi, Z.; Feng, S., Phase-controlled synthesis of orthorhombic and tetragonal $AgGaSe_2$ nanocrystals with high quality. *Chemical Communications* **2016,** *52* (55), 8581-8584.

34. Tappan, B. A.; Horton, M. K.; Brutchey, R. L., Ligand-Mediated Phase Control in Colloidal $AgInSe_2$ Nanocrystals. *Chemistry of Materials* **2020,** *32* (7), 2935-2945.

35. Park, Y. J.; Oh, J. H.; Han, N. S.; Yoon, H. C.; Park, S. M.; Do, Y. R.; Song, J. K., Photoluminescence of Band Gap States in $AgInS_2$ Nanoparticles. *The Journal of Physical Chemistry C* **2014,** *118* (44), 25677-25683.

36. Ng, M. T.; Boothroyd, C. B.; Vittal, J. J., One-Pot Synthesis of New-Phase $AgInSe_2$ Nanorods. *Journal of the American Chemical Society* **2006,** *128* (22), 7118-7119.

37. Leach, A. D. P., The Phase Dependent Optoelectronic Properties of Ternary I-III-VI_2 Semiconductor Nanocrystals and Their Synthesis. *Doctoral dissertation* **2017,** *Vanderbilt University* (Vanderbilt University).

38. Bai, T.; Li, C.; Li, F.; Zhao, L.; Wang, Z.; Huang, H.; Chen, C.; Han, Y.; Shi, Z.; Feng, S., A simple solution-phase approach to synthesize high quality ternary $AgInSe_2$ and band gap tunable quaternary $AgIn(S_{1-x}Se_x)_2$ nanocrystals. *Nanoscale* **2014,** *6* (12), 6782-6789.

39. Yu, W. W.; Wang, Y. A.; Peng, X., Formation and Stability of Size-, Shape-, and Structure-Controlled CdTe Nanocrystals: Ligand Effects on Monomers and Nanocrystals. *Chemistry of Materials* **2003,** *15* (22), 4300-4308.

40. Yu, W. W.; Peng, X., Formation of High-Quality CdS and Other II–VI Semiconductor Nanocrystals in Noncoordinating Solvents: Tunable Reactivity of Monomers. *Angewandte Chemie International Edition* **2002,** *41* (13), 2368-2371.

41. Bullen, C. R.; Mulvaney, P., Nucleation and Growth Kinetics of CdSe Nanocrystals in Octadecene. *Nano Letters* **2004,** *4* (12), 2303-2307.

42. Geisenhoff, J. Q.; Tamura, A. K.; Schimpf, A. M., Using ligands to control reactivity, size and phase in the colloidal synthesis of WSe_2 nanocrystals. *Chemical Communications* **2019,** *55* (60), 8856-8859.

43. Moya, C.; Batlle, X.; Labarta, A., The effect of oleic acid on the synthesis of $Fe_{3-x}O_4$ nanoparticles over a wide size range. *Physical Chemistry Chemical Physics* **2015,** *17* (41), 27373-27379.

44. Yang, H.; Hamachi, L. S.; Rreza, I.; Wang, W.; Chan, E. M., Design Rules for One-Step Seeded Growth of Nanocrystals: Threading the Needle between Secondary Nucleation and Ripening. *Chemistry of Materials* **2019,** *31* (11), 4173-4183.

45. Washington, A. L.; Foley, M. E.; Cheong, S.; Quffa, L.; Breshike, C. J.; Watt, J.; Tilley, R. D.; Strouse, G. F., Ostwald's Rule of Stages and Its Role in CdSe Quantum Dot Crystallization. *Journal of the American Chemical Society* **2012,** *134* (41), 17046-17052.

46. Tappan, B. A.; Barim, G.; Kwok, J. C.; Brutchey, R. L., Utilizing Diselenide Precursors toward Rationally Controlled Synthesis of Metastable $CuInSe_2$ Nanocrystals. *Chemistry of Materials* **2018,** *30* (16), 5704-5713.

47. Zou, Y.; Su, X.; Jiang, J., Phase-Controlled Synthesis of Cu_2ZnSnS_4 Nanocrystals: The Role of Reactivity between Zn and S. *Journal of the American Chemical Society* **2013,** *135* (49), 18377-18384.

48. Almeida, G.; Goldoni, L.; Akkerman, Q.; Dang, Z.; Khan, A. H.; Marras, S.; Moreels, I.; Manna, L., Role of Acid–Base Equilibria in the Size, Shape, and Phase Control of Cesium Lead Bromide Nanocrystals. *ACS Nano* **2018,** *12* (2), 1704-1711.

49. Harris, R. A.; Shumbula, P. M.; van der Walt, H., Analysis of the Interaction of Surfactants Oleic Acid and Oleylamine with Iron Oxide Nanoparticles through Molecular Mechanics Modeling. *Langmuir* **2015,** *31* (13), 3934-3943.

50. Li, J.; Bloemen, M.; Parisi, J.; Kolny-Olesiak, J., Role of Copper Sulfide Seeds in the Growth Process of $CuInS_2$ Nanorods and Networks. *ACS Applied Materials & Interfaces* **2014,** *6* (22), 20535-20543.

51. Ghosh, S.; Avellini, T.; Petrelli, A.; Kriegel, I.; Gaspari, R.; Almeida, G.; Bertoni, G.; Cavalli, A.; Scotognella, F.; Pellegrino, T.; Manna, L., Colloidal CuFeS2 Nanocrystals: Intermediate Fe d-Band Leads to High Photothermal Conversion Efficiency. *Chemistry of Materials* **2016,** *28* (13), 4848-4858.

Chapter 5. CONCLUSIONS AND OUTLOOK

In this dissertation, a set of experimental and computational results has been given to unambiguously identify two fundamentally different modes of resonant excitation present in ternary metal chalcogenide nanocrystal systems.

In Chapter 3, we investigated the iron-content-dependent optical characteristics of copper iron sulfide nanocrystals (NCs). After developing a protocol for the synthesis of bornite-phase copper iron sulfide NCs with controlled size and compositionally tunable iron content, systematic experimental and computational studies revealed that the presence of an intermediate band of states formed by empty Fe d-orbitals gives rise to the occurrence of a quasi-static dielectric resonance (DR) in the visible-frequency regime, analogous to the observed optical response in all-dielectric intermediate band chalcopyrite $CuFeS_2$ NCs. Moreover, we demonstrated that the spectral position of the DR does not change while its intensity is reduced, as the iron content of ternary Cu-Fe-S NCs is decreased via post-synthetic oxidation, clearly differentiating this mode of resonant excitation from the well-known localized surface plasmon resonance (LSPR) response, which shifts substantially in frequency as the free-carrier concentration is modified.

In Chapter 4, we extended these findings to the occurrence of quasi-static dielectric resonances in the silver iron sulfide ($AgFeS_2$) NC system. In the silver iron sulfide system, we confirmed analogous behavior, where quasi-static dielectric resonances arise from a negative permittivity in the UV-visible region of the electromagnetic spectrum, facilitated once again by the distinctive electronic structure of iron-enabled intermediate band of states. Moreover, we once again clearly differentiated two different types of resonant excitation between an IB-enabled DR and an LSPR through the synthesis of $AgFeS_2$ colloidal NCs, which occurs in discrete steps that begin with the formation of silver NCs. In addition, through spectroscopic studies and

computational calculations, we demonstrated that the increased distance between the valence band and Fe-enabled intermediate band significantly blueshifts the dielectric resonance energy due to the changes in the total permittivity that are affected by the position of the intermediate band.

Within this work, Fe-containing ternary metal chalcogenide intermediate band semiconductor nanocrystals have been identified as materials that can exhibit a DR in the UV-vis region. Overall, our work represents a significant step forward in a more complete understanding of the plasmonic-like resonant optical response of intermediate band semiconductor NCs, which might lead to important ramifications for future applications of these materials. Considering the dielectric permittivity of ternary metal iron chalcogenide intermediate band semiconductor NCs, we envision their potential use in epsilon-near-zero photonics as a new platform to enable finer control of light-matter interaction and enhancement of nonlinear-optical processes. To this end, an important step for future study will be the testing of the optical losses associated with the imaginary components of the material dielectric function. Moreover, another interesting future avenue of research is investigating the catalytic activity of ternary metal iron chalcogenide NCs in visible-light photocatalysis, benefiting from their low transition energies between the valence and intermediate band that have potential for enhanced charge separation.

5.1 Future Work: Synthesis of Novel Hetero-nanostructures by Cation Exchange Reaction of Copper Sulfide Nanocrystals

This dissertation has helped lay the groundwork for engineering resonant light-matter interactions in ternary metal chalcogenide intermediate band semiconductor NCs. Besides furthering knowledge towards their practical application, future experiments regarding the design of novel hetero-nanostructures (HNs) that exhibit both a visible-frequency DR and a near-infrared

LSPR in a single nanocrystal system could be of great interest for broadband enhancement of light absorption.

5.1.1 *Motivation*

Multifunctional nanomaterials have attracted great attention for various applications such as photocatalysis,[1-3] spintronics,[4-5] and biomedical applications.[6-8] Heterostructured NCs containing two or more different nanocrystal systems represent an important type of multifunctional nanomaterial due to their ability to provide a means of integrating multiple properties from different materials.[9-13] Currently, the development of synthetic protocols for HNs using copper sulfide NCs is an active research topic due to the potential to possess both the plasmonic properties of non-stoichiometric copper sulfides and additional properties of other semiconductors or metals.[14-19] For example, Lian *et al.* reported LSPR-induced hot-hole transfer in CdS/CuS HNs that show 19% charge transfer efficiencies along with long-lived 9.2 μs charge separation, potentially leading to developments in the photocatalyst field.[14]

Moreover, the dual plasmonic properties of noble metal and copper sulfide HNs with broad-spectrum light absorption have recently been explored for biomedical application.[17-18, 20-21] However, their synergistic effects are restricted by the different nature of the plasmonic materials in that the occurrence of LSPRs in copper sulfide NCs arises from resonantly excited free hole oscillations while LSPRs in metals are attributed to their free electrons.[19, 22] In this dissertation, we showed that $CuFeS_2$ NCs exhibit strong resonant light absorption and scattering in the visible region via a DR that originates from their distinctive electronic band structure. To solve the problem of damped dual plasmonic response in noble metal and copper sulfide HNs, here we

propose a new class of hybrid entity composed of copper sulfide and copper iron sulfide for broadband enhancement of light absorption.

5.1.2 *Preliminary Results and Discussion*

To date, the cation exchange reaction has been widely used as a versatile tool for the synthesis of diverse copper sulfide HNs due to the advantage of Cu atoms that enable efficient interstitial diffusion and substitution of incoming cations by their high mobility at high temperature.[23-26] One notable example of this is the successful synthesis of 47 distinct copper sulfide HNs via cation exchange by Fenton *et al.* in 2018.[26] However, precise control of the stoichiometry and crystal phase of copper chalcogenide HNs is still challenging as different precursors require varying reaction conditions.

Before controlling specific reaction conditions to synthesize copper sulfide and copper iron sulfide HNs, the possibility of incorporation of Fe into covellite-phase copper sulfide (CuS) NCs was first investigated under different reaction conditions: (i) in the presence of 1-dodecanethiol (1-DDT), (ii) with the addition of trioctylphosphine (TOP), and (iii) without the addition of 1-DDT or TOP (See **Appendix C** for experimental details). Preliminary experiments have demonstrated that iron can be incorporated into CuS NCs in the presence of 1-DDT and without the addition of 1-DDT or TOP, as shown by the XRD patterns in **Figure 5.1**. Moreover, the results show that the addition of 1-DDT plays a significant role in the phase-selective synthesis of $CuFeS_2$ NCs. In addition to the XRD analysis, the extinction spectra of the samples before and after cation exchange reactions with 1-DDT corroborate the selective formation of $CuFeS_2$ NCs (**Figure 5.2**).

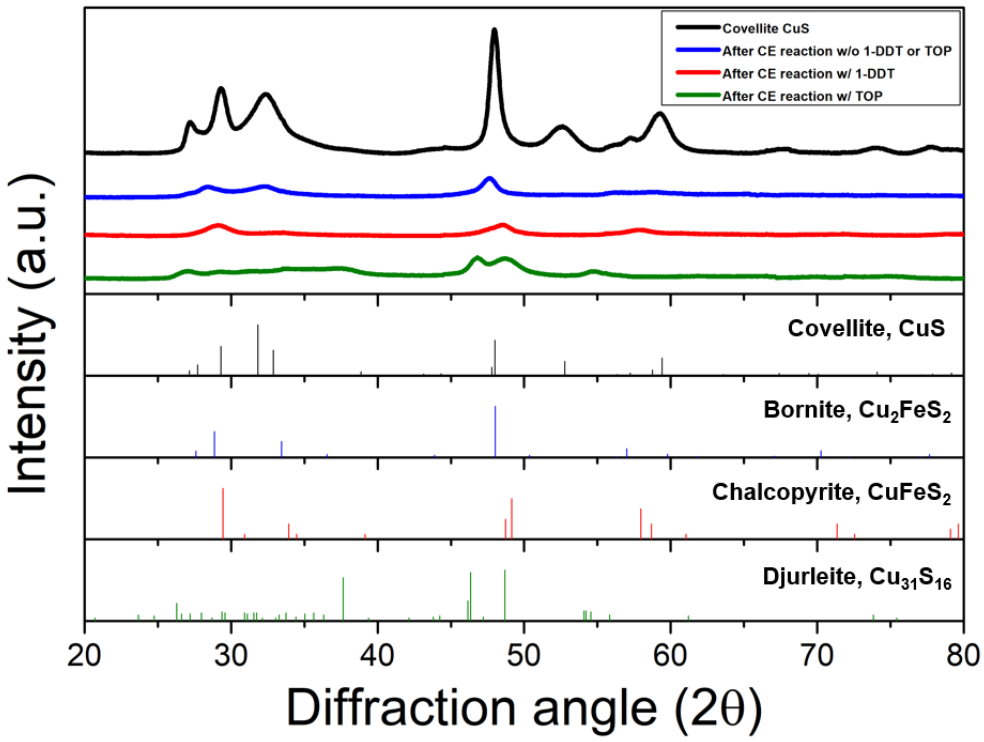

Figure 5.1. XRD patterns of the pristine CuS NCs and the samples after cation exchange (CE) reaction under various condition (Blue: Without 1-DDT or TOP, Red: With 1-DDT, Green: With TOP).

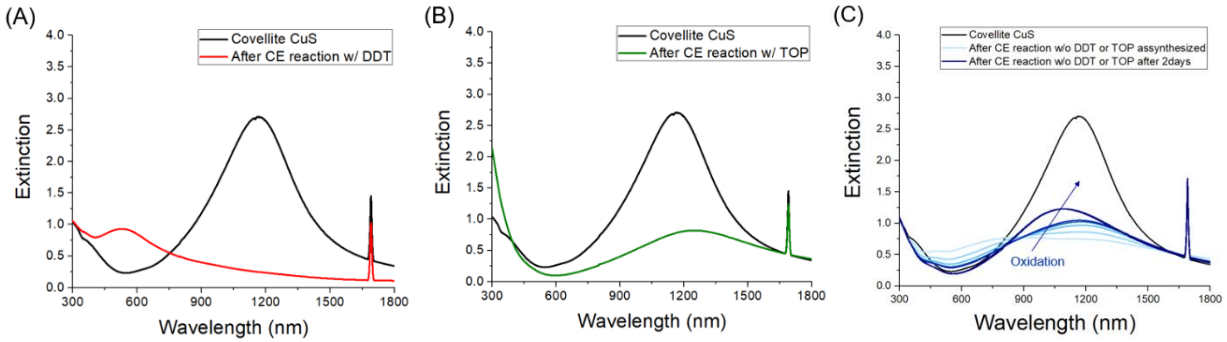

Figure 5.2. The extinction spectra of the samples after cation exchange reaction (A) with 1-DDT, (B) with TOP, and (C) without 1-DDT or TOP.

Moreover, no obvious changes in the size distribution of the samples before and after cation exchange reactions supports the successful incorporation of Fe into CuS NCs via cation exchange reaction (**Figure 5.3**). However, although the Fe ions are successfully incorporated into the CuS lattice with the addition of 1-DDT, the reaction conditions need to be further engineered in order to synthesize CuS/$CuFeS_2$ HNs. Based on previous studies of the cation exchange reactions of colloidal copper chalcogenide NCs, the extent of cation incorporation is highly dependent on the reaction time, temperature, and type and concentration of cation precursors and ligands.[23, 27-29] Therefore, we are currently working to develop a synthetic protocol for novel CuS/$CuFeS_2$ HNs by careful tuning the necessary reaction parameters.

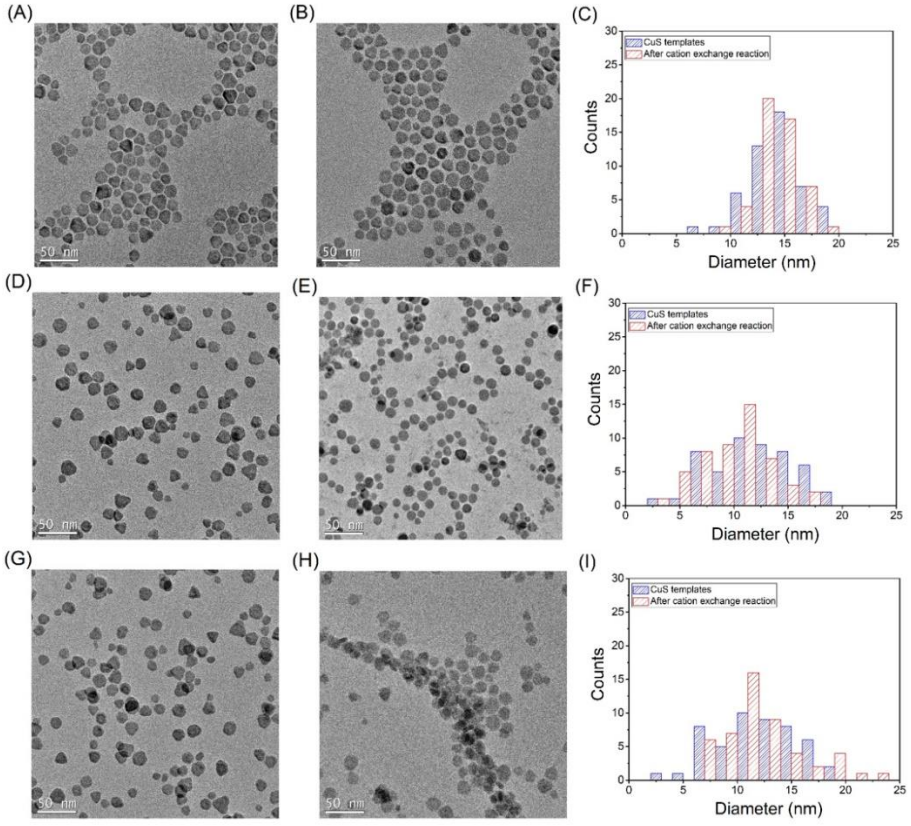

Figure 5.3. TEM images of (A, D, and G) pristine CuS NCs before cation exchange reaction, (B, E, and H) after cation exchange reaction with 1-DDT, with TOP, and without any additional reagents, respectively. (C, F, and I) The corresponding size distributions.

5.1.3 *Preliminary Conclusions*

Herein, we provide preliminary data for the synthesis of binary copper sulfide and ternary copper iron sulfide HNs by means of cation exchange reaction. Combining all of the above results and observations, we found that the presence of 1-DDT plays an important role in the phase-selective synthesis of $CuFeS_2$ NCs through cation exchange. A future direction of study will be reducing the reaction rate of cation exchange for the synthesis of $CuS/CuFeS_2$ HNs. We believe that rationally designed $CuS/CuFeS_2$ HNs have the potential for unprecedent optical properties that could be obtained from the concurrence of an IB-enabled DR and an LSPR.

5.2 SUMMARY OF CONTRIBUTIONS

The work presented in this dissertation aimed to understand the unique light-matter interactions in ternary metal chalcogenide intermediate band semiconductor NCs. Extensive experimental and computational work provided clear evidence that the resonant optical characteristics of ternary metal chalcogenide intermediate band semiconductor NCs in the visible region look similar to the optical response of noble metal NCs on the account of an IB-enabled DR, which represents a different type of resonant excitation than the well-known LSPR. Notably, Chapter 3 demonstrated how the removal or addition of iron atoms in ternary Cu-Fe-S NCs can be used to investigate the key role that the presence of the intermediate Fe d-band plays in enabling a Fröhlich resonance in the visible region of the the electromagnetic spectrum, and to modulate between the DR and LSPR responses, with potential use in dynamically responsive material applications. Moreover, Chapter 4 contributed to not only expanding the library of intermediate band semiconductor NCs that exhibit DR excitation, but also to achieving a better understanding of the DR characteristics of ternary metal iron sulfide NCs.

As a final note, I hope that this dissertation provides a strong foundation for future research in the use of ternary metal chalcogenide intermediate band semiconductor NCs for a variety of applications, benefiting from their resonant light-matter interactions.

5.3 REFERENCES

1. Lin, Z.; Ye, M.; Wang, M., *Multifunctional Photocatalytic Materials for Energy*. Elsevier Science: 2018.

2. Li, X.; Zhu, Z.; Li, F.; Huang, Y.; Hu, X.; Huang, H.; Peng, R.; Zhai, X.; Fu, Z.; Lu, Y., Multifunctional Single-Phase Photocatalysts: Extended Near Infrared Photoactivity and Reliable Magnetic Recyclability. *Scientific Reports* **2015,** *5* (1), 15511.

3. Tahir, M.; Cao, C.; Mahmood, N.; Butt, F. K.; Mahmood, A.; Idrees, F.; Hussain, S.; Tanveer, M.; Ali, Z.; Aslam, I., Multifunctional g-C_3N_4 Nanofibers: A Template-Free Fabrication and Enhanced Optical, Electrochemical, and Photocatalyst Properties. *ACS Applied Materials & Interfaces* **2014,** *6* (2), 1258-1265.

4. Žutić, I.; Fabian, J.; Das Sarma, S., Spintronics: Fundamentals and applications. *Reviews of Modern Physics* **2004,** *76* (2), 323-410.

5. Wolf, S. A.; Awschalom, D. D.; Buhrman, R. A.; Daughton, J. M.; von Molnár, S.; Roukes, M. L.; Chtchelkanova, A. Y.; Treger, D. M., Spintronics: A Spin-Based Electronics Vision for the Future. *Science* **2001,** *294* (5546), 1488.

6. Huh, Y.-M.; Jun, Y.-w.; Song, H.-T.; Kim, S.; Choi, J.-s.; Lee, J.-H.; Yoon, S.; Kim, K.-S.; Shin, J.-S.; Suh, J.-S.; Cheon, J., In Vivo Magnetic Resonance Detection of Cancer by Using Multifunctional Magnetic Nanocrystals. *Journal of the American Chemical Society* **2005,** *127* (35), 12387-12391.

7. Wang, X.; Liu, H.; Chen, D.; Meng, X.; Liu, T.; Fu, C.; Hao, N.; Zhang, Y.; Wu, X.; Ren, J.; Tang, F., Multifunctional Fe_3O_4@P(St/MAA)@Chitosan@Au Core/Shell Nanoparticles for Dual Imaging and Photothermal Therapy. *ACS Applied Materials & Interfaces* **2013,** *5* (11), 4966-4971.

8. Wang, H.; An, L.; Tao, C.; Ling, Z.; Lin, J.; Tian, Q.; Yang, S., A smart theranostic platform for photoacoustic and magnetic resonance dual-imaging-guided photothermal-enhanced chemodynamic therapy. *Nanoscale* **2020,** *12* (8), 5139-5150.

9. Wang, H.; Wang, Y.; Jiang, C.; Ye, K.; He, X.; Xue, C.; Yang, Z.; Zhou, X.; Ji, H., Hybridization of CuO with Bi_2MoO_6 Nanosheets as a Surface Multifunctional Photocatalyst for Toluene Oxidation under Solar Irradiation. *ACS Applied Materials & Interfaces* **2020,** *12* (2), 2259-2268.

10. Sinha, T.; Ahmaruzzaman, M.; Adhikari, P. P.; Bora, R., Green and Environmentally Sustainable Fabrication of Ag-SnO_2 Nanocomposite and Its Multifunctional Efficacy As Photocatalyst and Antibacterial and Antioxidant Agent. *ACS Sustainable Chemistry & Engineering* **2017,** *5* (6), 4645-4655.

11. Lin, Y.; Zhou, S.; Sheehan, S. W.; Wang, D., Nanonet-Based Hematite Heteronanostructures for Efficient Solar Water Splitting. *Journal of the American Chemical Society* **2011,** *133* (8), 2398-2401.

12. Ha, M.; Kim, J.-H.; You, M.; Li, Q.; Fan, C.; Nam, J.-M., Multicomponent Plasmonic Nanoparticles: From Heterostructured Nanoparticles to Colloidal Composite Nanostructures. *Chemical Reviews* **2019,** *119* (24), 12208-12278.

13. Sun, Z.; Du, J.; Yan, L.; Chen, S.; Yang, Z.; Jing, C., Multifunctional Fe_3O_4@SiO_2–Au Satellite Structured SERS Probe for Charge Selective Detection of Food Dyes. *ACS Applied Materials & Interfaces* **2016,** *8* (5), 3056-3062.

14. Lian, Z.; Sakamoto, M.; Matsunaga, H.; Vequizo, J. J. M.; Yamakata, A.; Haruta, M.; Kurata, H.; Ota, W.; Sato, T.; Teranishi, T., Near infrared light induced plasmonic hot hole transfer at a nano-heterointerface. *Nature Communications* **2018,** *9* (1), 2314.

15. Liu, M.; Liu, Y.; Gu, B.; Wei, X.; Xu, G.; Wang, X.; Swihart, M. T.; Yong, K.-T., Recent advances in copper sulphide-based nanoheterostructures. *Chemical Society Reviews* **2019,** *48* (19), 4950-4965.

16. Han, S.-K.; Gong, M.; Yao, H.-B.; Wang, Z.-M.; Yu, S.-H., One-Pot Controlled Synthesis of Hexagonal-Prismatic $Cu_{1.94}S$-ZnS, $Cu_{1.94}S$-ZnS-$Cu_{1.94}S$, and $Cu_{1.94}S$-ZnS-$Cu_{1.94}S$-ZnS-$Cu_{1.94}S$ Heteronanostructures. *Angewandte Chemie International Edition* **2012,** *51* (26), 6365-6368.

17. Sun, M.; Fu, X.; Chen, K.; Wang, H., Dual-Plasmonic Gold@Copper Sulfide Core–Shell Nanoparticles: Phase-Selective Synthesis and Multimodal Photothermal and Photocatalytic Behaviors. *ACS Applied Materials & Interfaces* **2020,** *12* (41), 46146-46161.

18. Zhu, H.; Wang, Y.; Chen, C.; Ma, M.; Zeng, J.; Li, S.; Xia, Y.; Gao, M., Monodisperse Dual Plasmonic Au@$Cu_{2-x}E$ (E= S, Se) Core@Shell Supraparticles: Aqueous Fabrication, Multimodal Imaging, and Tumor Therapy at in Vivo Level. *ACS Nano* **2017,** *11* (8), 8273-8281.

19. Hu, C.; Chen, W.; Xie, Y.; Verma, S. K.; Destro, P.; Zhan, G.; Chen, X.; Zhao, X.; Schuck, P. J.; Kriegel, I.; Manna, L., Generating plasmonic heterostructures by cation exchange and redox reactions of covellite CuS nanocrystals with Au^{3+} ions. *Nanoscale* **2018,** *10* (6), 2781-2789.

20. Leng, C.; Zhang, X.; Xu, F.; Yuan, Y.; Pei, H.; Sun, Z.; Li, L.; Bao, Z., Engineering Gold Nanorod–Copper Sulfide Heterostructures with Enhanced Photothermal Conversion Efficiency and Photostability. *Small* **2018,** *14* (12), 1703077.

21. Sun, C.; Liu, M.; Zou, Y.; Wei, J.; Jiang, J., Synthesis of plasmonic Au–CuS hybrid nanocrystals for photothermal transduction and chemical transformations. *RSC Advances* **2016,** *6* (31), 26374-26379.

22. Wolf, A.; Kodanek, T.; Dorfs, D., Tuning the LSPR in copper chalcogenide nanoparticles by cation intercalation, cation exchange and metal growth. *Nanoscale* **2015,** *7* (46), 19519-19527.

23. Lee, S.; Baek, S.; Park, J. P.; Park, J. H.; Hwang, D. Y.; Kwak, S. K.; Kim, S.-W., Transformation from $Cu_{2-x}S$ Nanodisks to $Cu_{2-x}S@CuInS_2$ Heteronanodisks via Cation Exchange. *Chemistry of Materials* **2016,** *28* (10), 3337-3344.

24. Park, J.; Park, J.; Lee, J.; Oh, A.; Baik, H.; Lee, K., Janus Nanoparticle Structural Motif Control via Asymmetric Cation Exchange in Edge-Protected $Cu_{1.81}S@Ir_xS_y$ Hexagonal Nanoplates. *ACS Nano* **2018,** *12* (8), 7996-8005.

25. Liu, Y.; Liu, M.; Yin, D.; Qiao, L.; Fu, Z.; Swihart, M. T., Selective Cation Incorporation into Copper Sulfide Based Nanoheterostructures. *ACS Nano* **2018,** *12* (8), 7803-7811.

26. Fenton, J. L.; Steimle, B. C.; Schaak, R. E., Tunable intraparticle frameworks for creating complex heterostructured nanoparticle libraries. *Science* **2018,** *360* (6388), 513.

27. Lesnyak, V.; Brescia, R.; Messina, G. C.; Manna, L., Cu Vacancies Boost Cation Exchange Reactions in Copper Selenide Nanocrystals. *Journal of the American Chemical Society* **2015,** *137* (29), 9315-9323.

28. Hinterding, S. O. M.; Berends, A. C.; Kurttepeli, M.; Moret, M.-E.; Meeldijk, J. D.; Bals, S.; van der Stam, W.; de Mello Donega, C., Tailoring Cu^+ for Ga^{3+} Cation Exchange in $Cu_{2-x}S$ and $CuInS_2$ Nanocrystals by Controlling the Ga Precursor Chemistry. *ACS Nano* **2019,** *13* (11), 12880-12893.

29. Liu, Y.; Yin, D.; Swihart, M. T., Ag^+-Induced Shape and Composition Evolution of Covellite CuS Nanoplatelets To Produce Plate–Satellite and Biconcave−Particle Heterostructures. *Chemistry of Materials* **2018,** *30* (21), 8089-8098.

APPENDIX A

Effects of excess chloride addition on the synthesis of bornite NCs

In the absence of excess chloride, polydisperse, bornite-phase copper iron sulfide nanoplatelets with low iron content were consistently obtained. The presence of excess chloride in the reaction solution was necessary to achieve monodisperse bornite nanocrystal samples with tunable iron content.

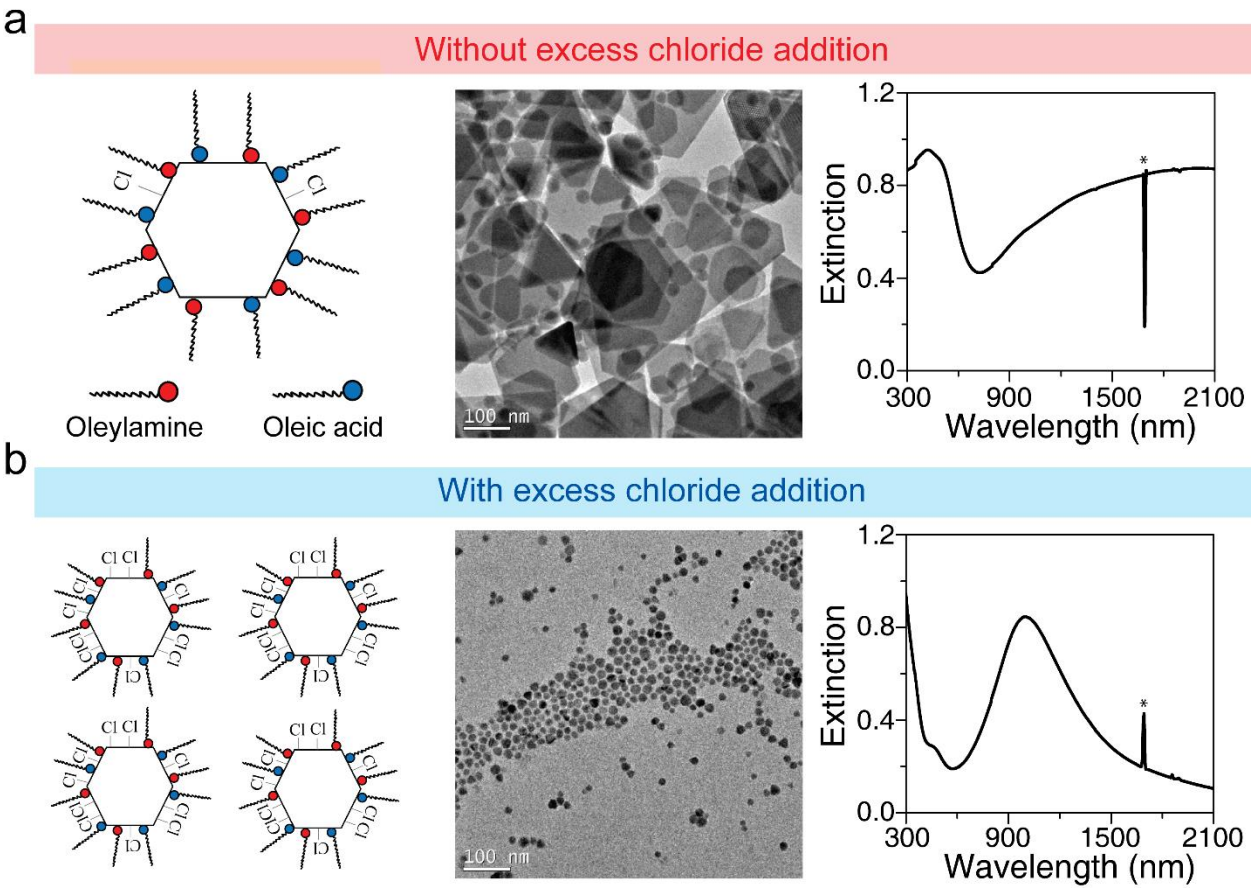

Figure A.1. Schematic illustration and representative TEM and UV-vis-NIR extinction spectra of copper iron sulfide NCs synthesized using 0.8 mmol of copper (II) chloride and 0.4 mmol of iron (III) chloride (a) without and (b) with addition of excess chloride anions. Spectral artifacts caused by the NIR absorption bands of the chloroform solvent are marked by asterisks.

TEM images and size distribution histograms of bornite NCs

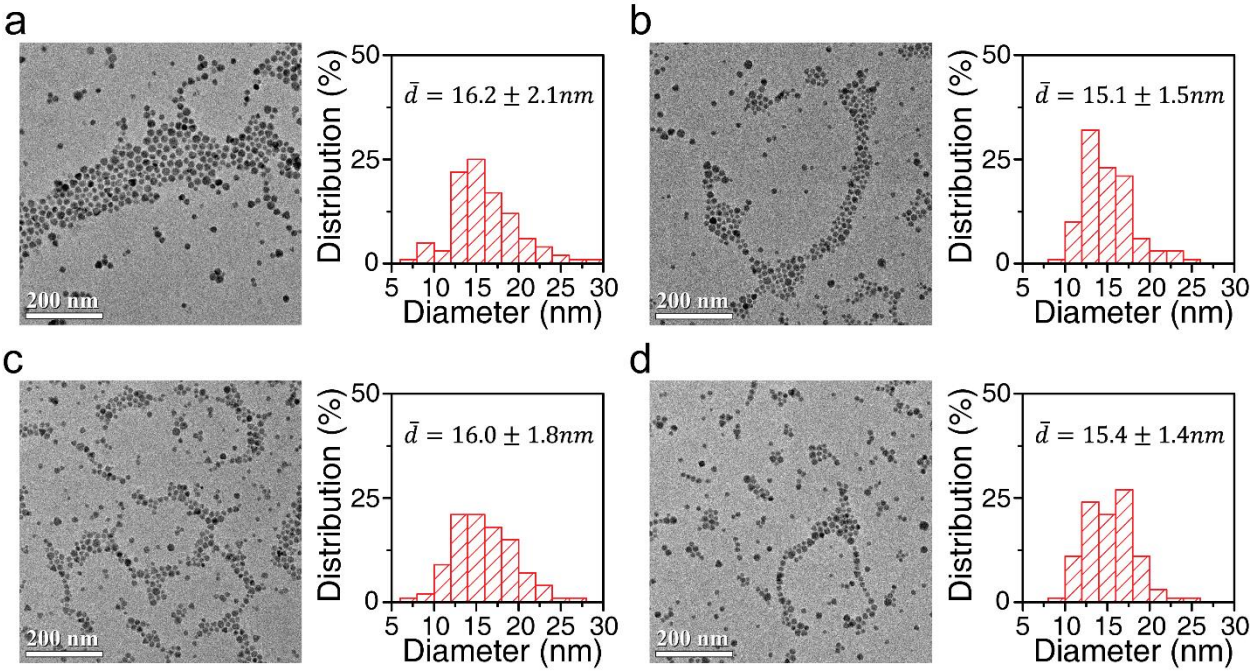

Figure A.2. TEM images and size distribution histograms of bornite NCs with (a) 4.1, (b) 6.3, (c) 9.5, and (d) 12.5% Fe. The corresponding size distributions were determined by analysis of 100 individual NCs.

Elemental analysis by energy-dispersive X-ray spectroscopy (EDXS)

Table A.1. Elemental compositions of bornite NCs

Precursor ratio (Cu:Fe)	Atomic (%)			Nanocrystal Stoichiometry
	Cu	Fe	S	
1:0.5	58.7	4.1	37.2	$Cu_{1.58}Fe_{0.11}S$
1:0.75	56.6	6.3	37.1	$Cu_{1.53}Fe_{0.17}S$
1:1	52.6	9.5	37.9	$Cu_{1.39}Fe_{0.25}S$
1:1.25	49.6	12.5	37.9	$Cu_{1.31}Fe_{0.33}S$

Crystal structures of bornite and chalcopyrite phases

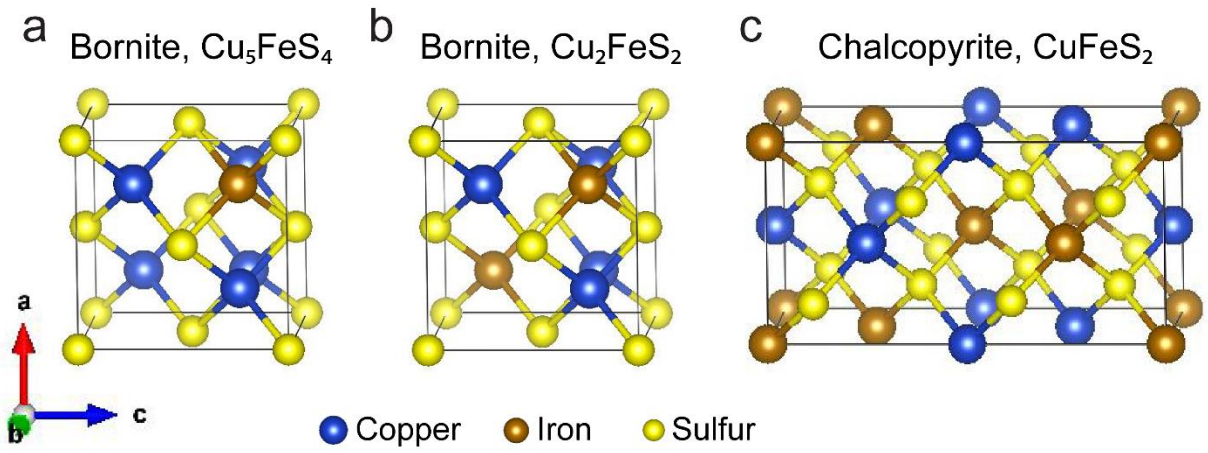

Figure A.3. Schematic representations of the crystal structure of (a) bornite Cu_5FeS_4, (b) bornite Cu_2FeS_2, and (c) chalcopyrite $CuFeS_2$.

Lattice constant calculation of bornite NCs

The lattice constants of bornite NCs were determined by applying Bragg's law to the (222), (400), (440), (622), (800), (844) X-ray diffraction peaks. For a cubic phases, the lattice constant can be expressed as follows[1-2]:

$$2d_{hkl}sin\theta = n\lambda \quad \text{(A.1)}$$

$$\text{a} = d_{hkl}\sqrt{h^2 + k^2 + l^2} \quad \text{(A.2)}$$

Where d_{hkl} is an inter-lattice spacing, θ is a Bragg diffraction angle, n is a positive integer, λ is the wavelength of the incident X-rays (λ=1.5406Å), a is the lattice constant, and h, k, and l are the Miller indices that correspond to each diffraction peak.

Table A.2. The X-ray diffraction peak positions used to calculate the lattice constants for bornite NCs with different iron content

Elemental fraction of Fe in NCs (%)	Peak positions (θ, degrees)						Lattice constant (Å)
	(222)	(400)	(440)	(622)	(800)	(844)	
4.1	14.10	16.34	23.49	27.84	34.31	43.42	10.95 ± 0.02
6.3	14.15	16.4	23.53	27.89	34.36	43.68	10.92 ± 0.01
9.5	14.25	16.5	23.73	28.08	34.61	44.04	10.85 ± 0.01
12.5	14.33	16.61	23.82	28.25	34.83	44.36	10.79 ± 0.01

Lattice compression from low-Fe to high-Fe bornite NCs

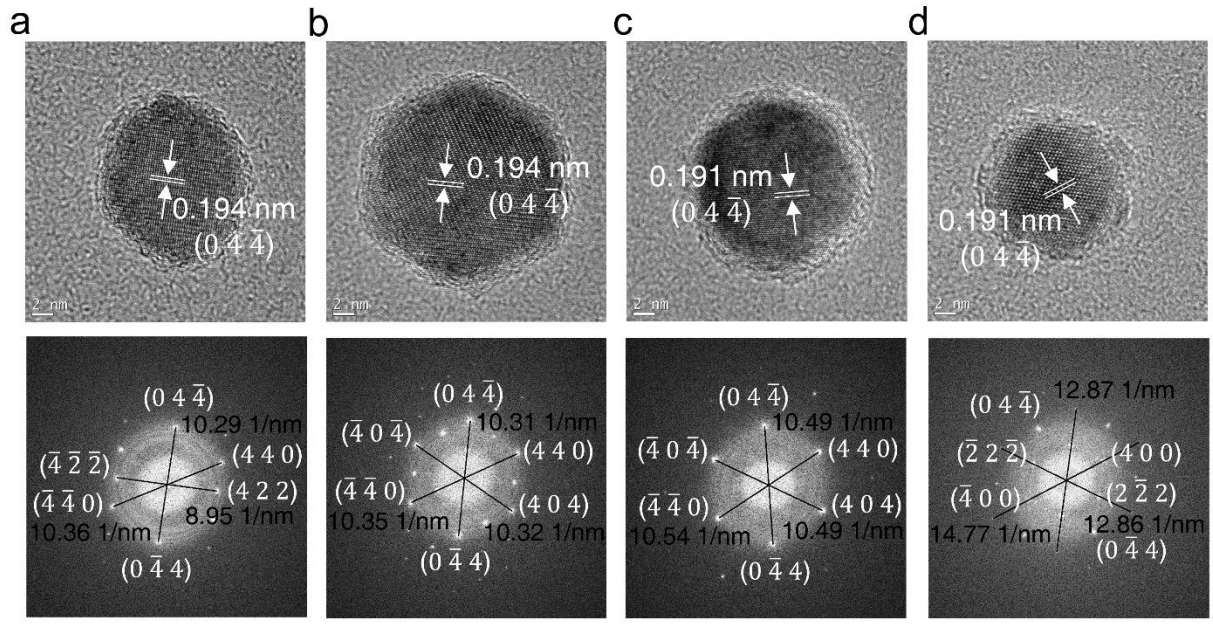

Figure A.4. HRTEM images of (a and b) low-Fe, and (c and d) high-Fe bornite NCs with the corresponding fast Fourier transforms shown below each panel.

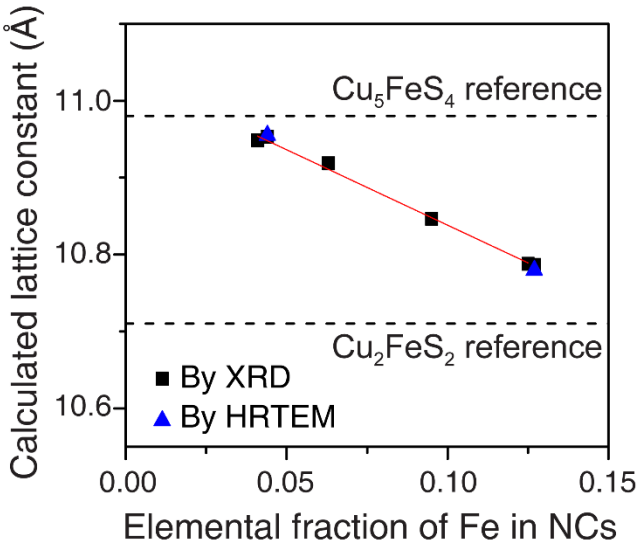

Figure A.5. Comparison of the calculated lattice constants for low-Fe and high-Fe bornite NCs as determined by XRD and HRTEM measurements.

Density functional theory (DFT) calculations

As mentioned in the computational details section of the main text, we modeled three different materials of varying Fe concentration: Cu_2FeS_2 (20 at.% Fe), $Cu_9Fe_3S_8$ (15 at.% Fe), and Cu_5FeS_4 (10 at.% Fe). We used a supercell approach composed of eight unit-cells in a 2x2x2 expansion. The lattice constant of the cubic supercell is 10.95 Å.[3] Norm-conserving pseudopotentials[4-5] and unrestricted PBE+U[6-7] were used in VASP.[8-11] A cutoff energy of 500 eV was used for the plane-wave basis. We optimized the atomic positions while keeping the lattice constant fixed on a 2x2x2 Monkhorst-Pack k-point mesh of the Brillouin zone.[12] A 6x6x6 k-point mesh was used for a subsequent density of states calculation.

Spin Coupling of Iron Atoms

Since we are interested in a qualitative characterization of the electronic structure, we used the same U parameter for PBE+U as a recent study of $CuFeS_2$.[13] We estimated the relative stability

of ferromagnetically and antiferromagnetically aligned iron atoms for each material. The geometries used for the single point were optimized with the corresponding Fe spin alignment except for $Cu_9Fe_3S_8$ which used the ferromagnetic (FM) geometry due to convergence difficulties for the antiferromagnetic (AFM) solution. As shown in Table A.3, the antiferromagnetic solution is lowest in energy for Cu_2FeS_2 and $Cu_9Fe_3S_8$; however, the Cu_5FeS_4 has a near degenerate AFM and FM configuration, the total energy difference is within in 0.1 eV, which is beyond the resolution of the DFT method. We expect our computational approach to be semi-quantitative and are therefore unable to make claims at a precision of more than 0.4 eV. Thus, we included both FM and AFM Cu_5FeS_4 in our study.

Table A.3. Difference in energy (eV) between ferromagnetic (FM) and antiferromagnetic (AFM) solutions computed with PBE+U

	Cu_2FeS_2	$Cu_9Fe_3S_8$	Cu_5FeS_4
FM	-362.36	-354.68	-344.98
AFM	-365.41	-355.57[a]	-344.88
AFM-FM	-3.05	-0.89	0.10

[a]Computed with FM geometry

Geometries

We used a supercell to model our material which consisted of 2x2x2 unit cells. Two types of unit cells were used: one containing iron defects and one containing vacuum defects. To maintain the long-range iron/vacancy defect clustering, we alternate the unit cells within the supercell.[14] For each choice of iron concentration, we optimized the atomic positions while keeping the supercell dimensions fixed. In the case of $Cu_9Fe_3S_8$, we were unable to converge to a stable structure for the antiferromagnetic case, so we use the ferromagnetic geometry. The iron-defect unit cells for AFM Cu_2FeS_2, AFM $Cu_9Fe_3S_8$, AFM Cu_5FeS_4, and FM Cu_5FeS_4 are shown in Figure S6. There is little difference between the structures; all of which exhibit a Cu-Fe distance of 2.75 Å.

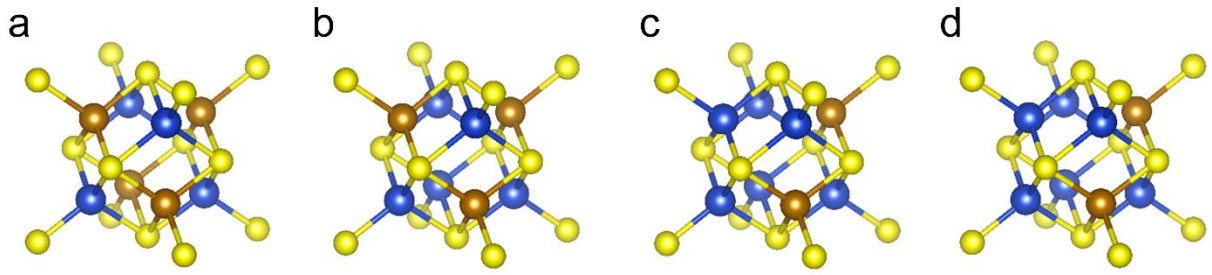

Figure A.6. Iron-defect unit cell for (a) antiferromagnetic Cu_2FeS_2, (b) antiferromagnetic $Cu_9Fe_3S_8$, (c) antiferromagnetic Cu_5FeS_4, and (d) ferromagnetic Cu_5FeS_4. Blue atoms are Cu, brown atoms are Fe, and yellow atoms are S.

Density of States

We report the atomic-projected density of states (DOS) for the three different materials. We were interested in understanding the qualitative nature of the intermediate band, specifically with respect to the Fe 3*d* contribution. The resulting DOS can be found for AFM Cu_5FeS_4, $Cu_9Fe_3S_8$, and Cu_2FeS_2 in Figure 3 of the manuscript. Due to the small energetic difference between the AFM and FM Cu_5FeS_4 shown in Table A.3, we also show the DOS and integrated density of states over the intermediate-band energy range of FM Cu_5FeS_4 in Figure A.7.

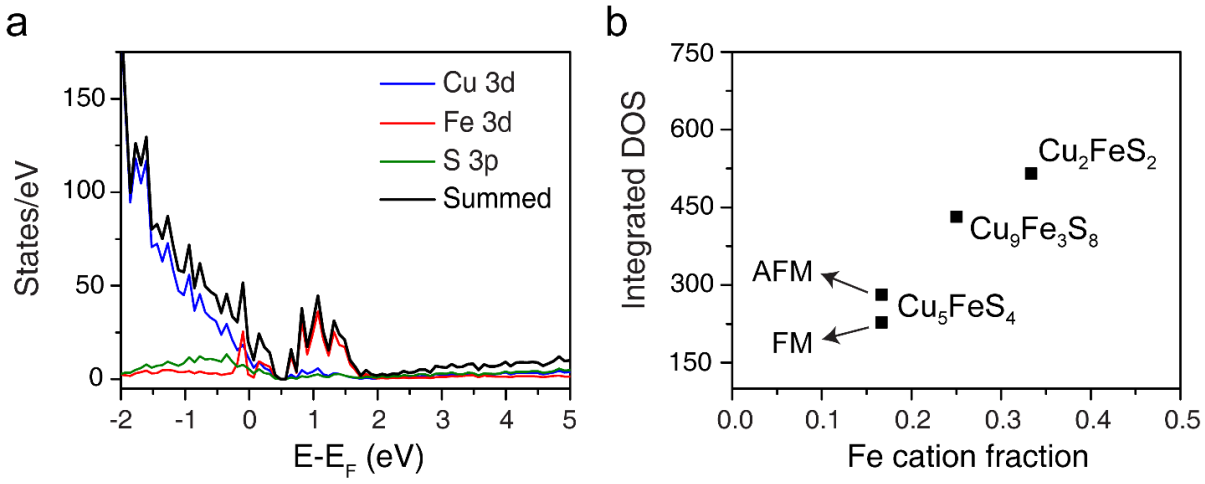

Figure A.7. (a) Atomic-projected density of states for ferromagnetic Cu_5FeS_4 and (b) integrated density of states of the intermediate band for all studied materials.

Band Structures

To understand the band characteristics near the Fermi energy, we performed band structure calculations for AFM Cu_5FeS_4, $Cu_9Fe_3S_8$, and Cu_2FeS_2 as shown in Figure A.8. We did not consider FM Cu_5FeS_4 due to the similar DOS observed when compared to AFM Cu_5FeS_4 (compare Figure 3.3 with Figure A.7). The lowest-energy band above the Fermi energy (E_F) that is dominated by the Fe 3*d* (compare with DOS in Figure 3.3) exhibits dispersion on the Γ point.

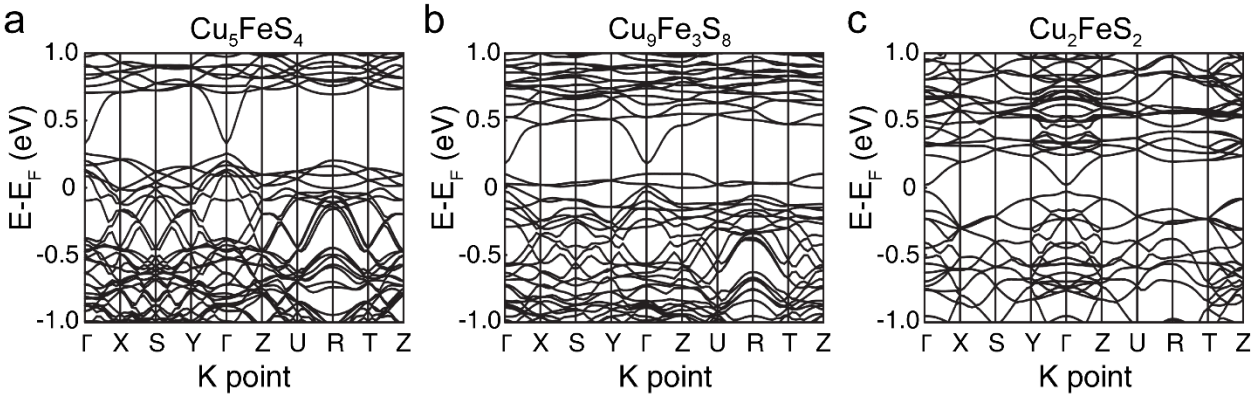

Figure A.8. Band structures computed relative to the Fermi energy for antiferromagnetic (a) Cu_5FeS_4, (b) $Cu_9Fe_3S_8$, and (c) Cu_2FeS_2, respectively.

Oxidation characteristics of bornite NCs

We found that differences in the extent of iron content in the bornite NCs have a large impact on their oxidation characteristics, particularly for NCs with between 6.3 and 9.5 at.% Fe. Moreover, an interesting observation is made when we compare the bornite NCs with controlled iron-content by synthesis and the post-synthetically oxidized NCs. In addition to the iron-content-dependent intermediate Fe d-band, it is possible that the abrupt spectral changes between 6.3 and 9.5 at.% Fe in the bornite NCs are a result of the Moss-Burstein effect caused by the appreciable number of free charge carriers (holes) in the valence band that are due to the formation of cation

vacancies,[15-16] thus leading to further changes in the electronic structure. These differences may seem small in number, but it is necessary to note that the occurrence of the DR is highly dependent on the position of the intermediate band between the valence band and conduction band, which has been well-demonstrated in previous literature.[17] Based on our observations and previous literature, we believe that oxidizing the bornite NC dispersion gradually under ambient air, which slowly ejects the iron from the lattice, effectively provides a gradual tuning of iron contents between 6.3% and 9.5%. As a result, the optical responses of the bornite NCs with post-synthetic oxidation treatment gradually converted from DR to LSPR.

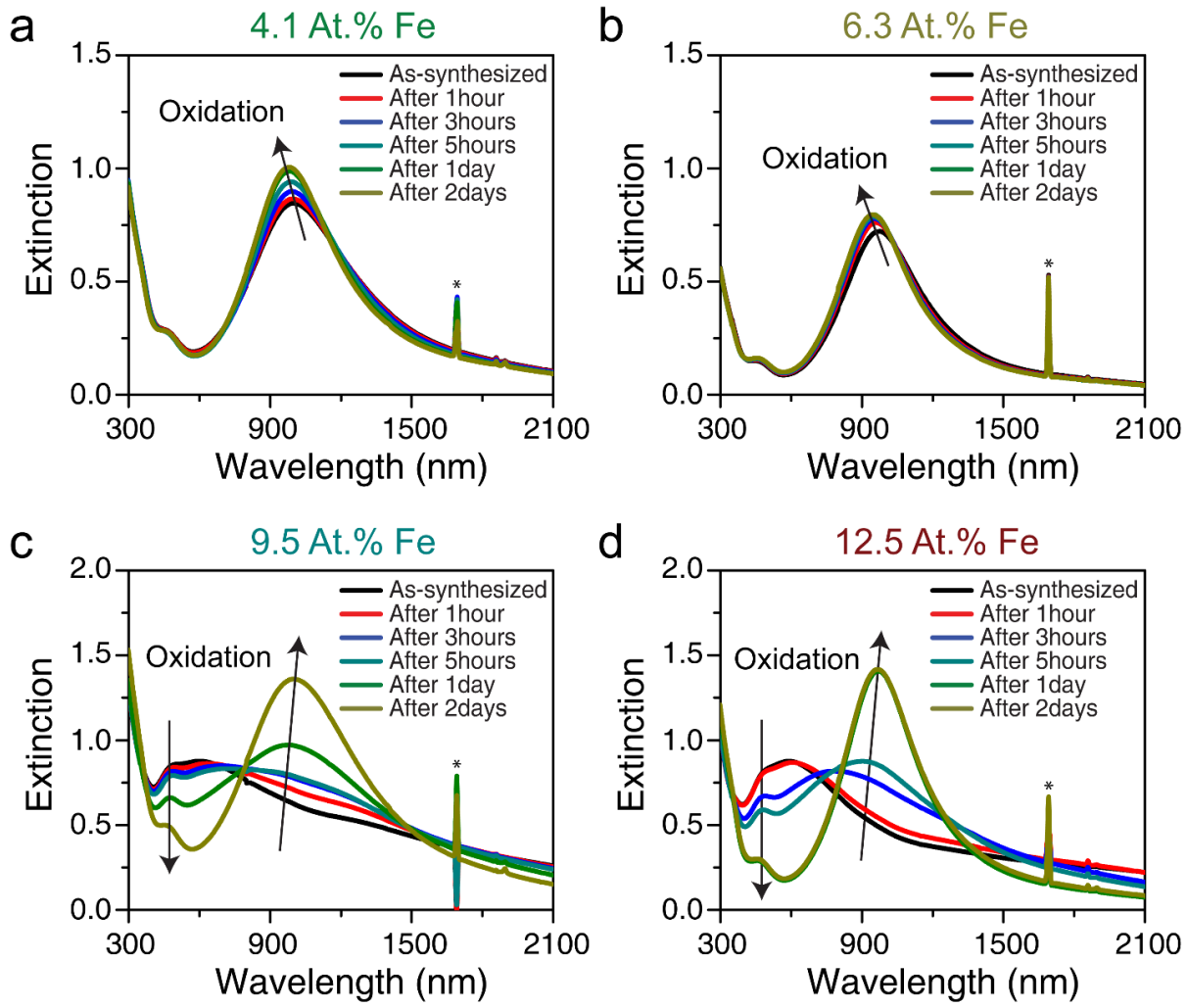

Figure A.9. UV-vis-NIR extinction spectra of bornite NCs with different Fe content – (a) 4.1, (b) 6.3, (c) 9.5, and (d) 12.5 at.% – as a function of oxidation time under ambient conditions. Spectral artifacts caused by the NIR absorption bands of the chloroform solvent are marked by asterisks.

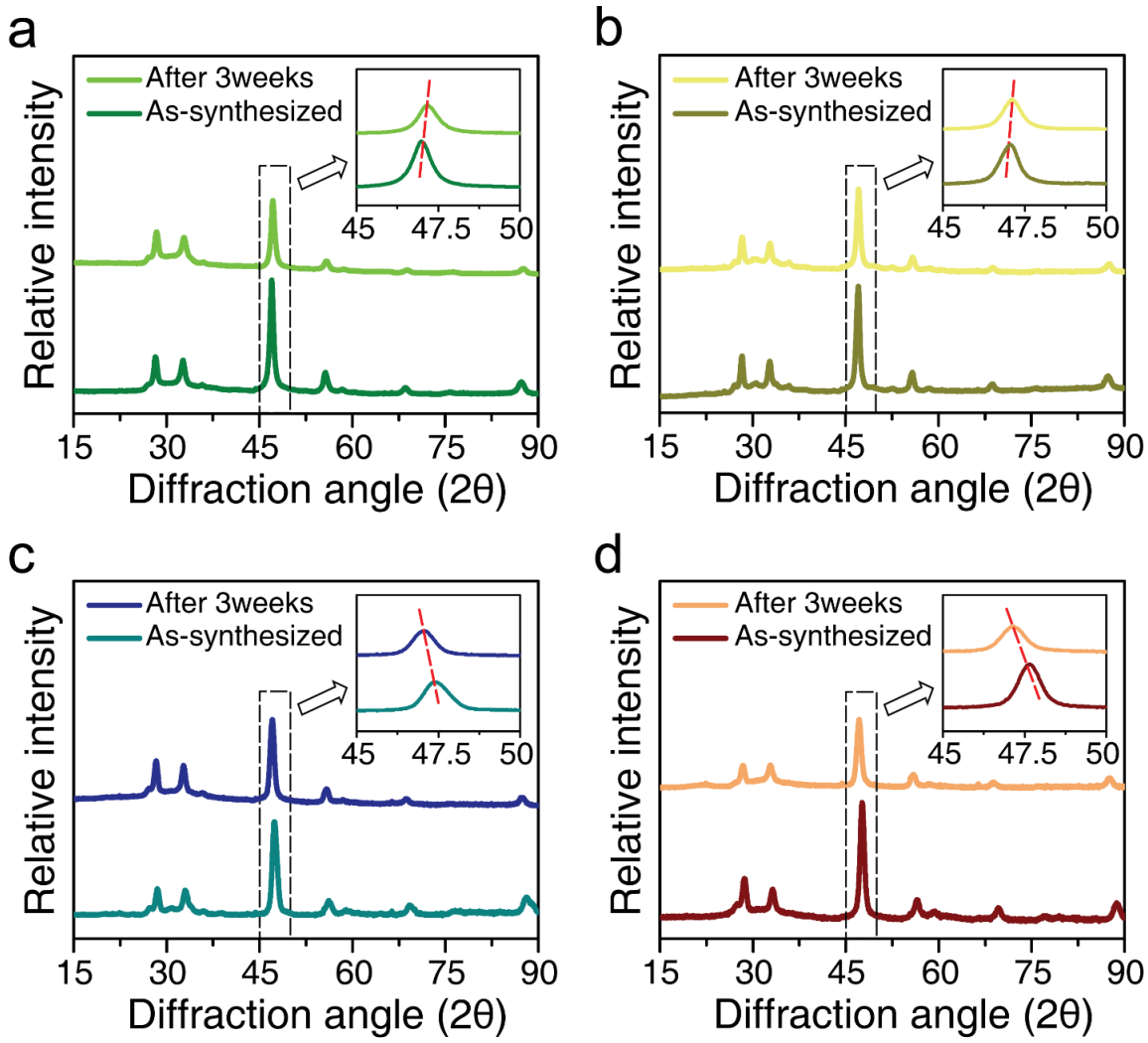

Figure A.10. XRD patterns of bornite NCs with different levels of Fe incorporation (a) 4.1, (b) 6.3, (c) 9.5, and (d) 12.5 at.% as-synthesized, and after three weeks of oxidation under ambient conditions.

Elemental analysis of high-Fe bornite NCs before and after oxidation

Inductively coupled plasma optical emission spectroscopy (ICP-OES) was conducted to determine the chemical composition of high-Fe bornite NCs before and after oxidation. To check for oxidative leaching of iron, we analyzed the composition of high-Fe bornite NCs before oxidation, the oxidized high-Fe bornite NC precipitates, and their supernatants. Elemental analysis shows that the Cu/Fe molar ratio of high-Fe bornite NCs before oxidation is about 3.9, which is similar to the molar ratio of Cu and Fe determined by EDXS. After oxidation, the Cu:Fe stoichiometric ratio of the high-Fe bornite NC precipitates increased significantly to 8.9, while the Cu:Fe stoichiometric ratio of the supernatant decreased to 0.41:1, confirming that iron atoms leave the bornite NCs and remain in the supernatant upon oxidation. The results are summarized in Table S4. Furthermore, we confirm that the initial Fe content of the high-Fe bornite NCs before oxidation matches the sum of the oxidized bornite NC iron content and the amount of iron measured in the supernatant.

Table A.4. ICP-OES results of high-Fe bornite NCs before oxidation, the oxidized high-Fe bornite NC precipitates, and their supernatants.

Samples	Weight (%)		Atomic (%)		Atomic ratio (Cu:Fe)
	Cu	Fe	Cu	Fe	
Bornite NCs before oxidation	81.7	18.3	79.7	20.3	3.92:1
Oxidized bornite NC precipitates	91.0	9.0	89.9	10.1	8.91:1
Oxidized supernatants	31.7	68.3	29.0	71.0	0.41:1

Dependence of the bornite NC visible extinction band on the refractive index of the surrounding medium

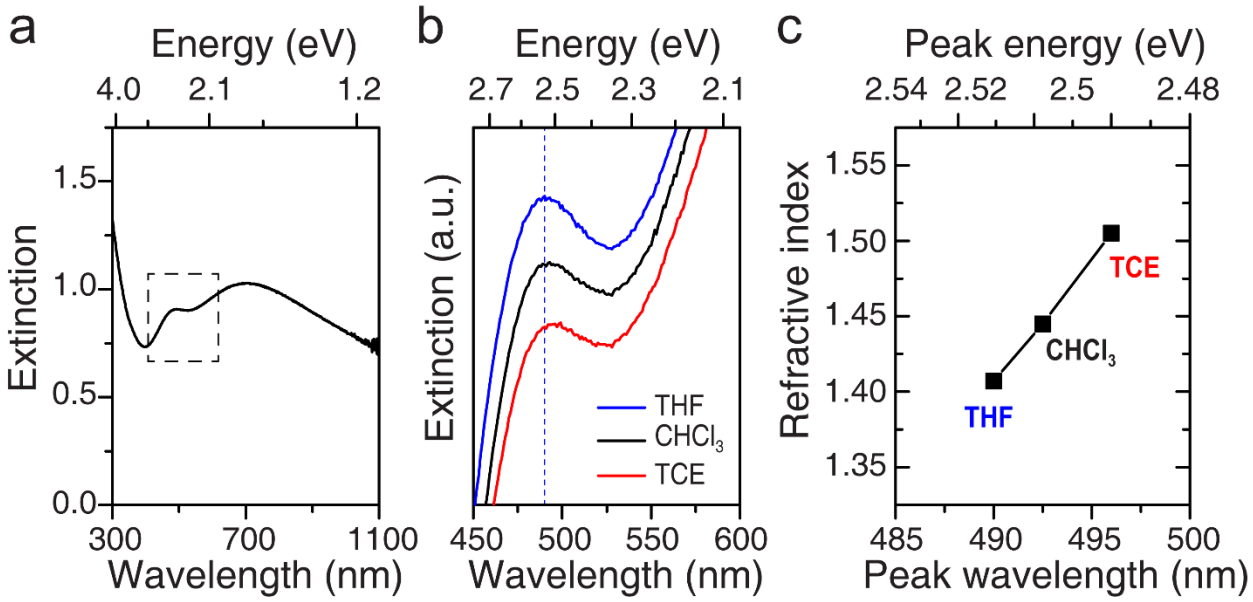

Figure A.11. (a) The UV-vis extinction spectrum of partially oxidized, high-Fe bornite NCs in chloroform. (b) Comparison of the extinction characteristics of the partially oxidized bornite NCs in three different solvents (tetrahydrofuran, chloroform, and tetrachloroethylene), and (c) changes in the absorption peak position as a function of the environment refractive index.

Calculated permittivities of bornite phases with different iron content

To estimate the frequency-dependent real permittivity, we applied a simplified version of a model previously developed for $CuFeS_2$.[17] The band energy cutoffs and state densities were obtained from our density of states calculations, as shown in Table A.5, where VB, IB, and CB indicate valence band, intermediate band, and conduction band, respectively, and where the CB energy minimum was selected as the first nonzero point after the IB. The resulting frequency-dependent permittivity curves are shown in Figure A.12. Since we were interested in the point

where the permittivity becomes negative, the curves in Figure A.12 were scaled by the scaling factor λ (0.0008).

Table A.5. Data used to generate permittivity curves using the model presented in Reference 15. Energies are in eV and densities are in states per eV.

	Cu_2FeS_2	$Cu_9Fe_3S_8$	Cu_5FeS_4
$E_{\min}^{VB}$	2.61	2.36	2.33
$E_{\max}^{VB}$	5.75	5.70	5.72
$E_{\min}^{IB}$	6.05	6.07	6.24
$E_{\max}^{IB}$	6.95	6.96	6.83
$E_{\min}^{CB}$	7.03	7.03	6.90
$E_{\max}^{CB}$	10.70	10.74	10.73
ρ^{VB}	912.4	932.4	1061.8
ρ^{IB}	515.6	411.0	384.9
ρ^{CB}	72.7	68.5	63.2

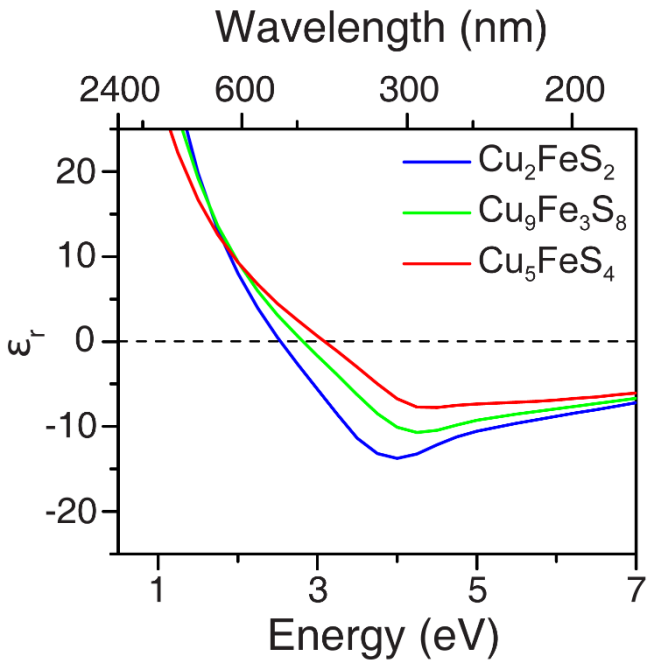

Figure A.12. Calculated real component of the permittivity for each of the bornite phases.

REFERENCES

1. JS Nkoma, G. E., X-ray diffraction study of chalcopyrite, pentlandite and pyrrhotite obtained from Cu-Ni ore bodies. *J. Phys.: Condens. Matter* **1999,** *11*, 121-127.

2. Bastola, E. B., Khagendra P. Ellingson, Randy J., Application of composition controlled nickel-alloyed iron sulfide pyrite nanocrystal thin films as the hole transport layer in cadmium telluride solar cells. *J. Mater. Chem. C* **2017,** *5* (20), 4996-5004.

3. Qiu, P.; Zhang, T.; Qiu, Y.; Shi, X.; Chen, L., Sulfide bornite thermoelectric material: a natural mineral with ultralow thermal conductivity. *Energy Environ. Sci.* **2014,** *7* (12), 4000-4006.

4. G. Kresse, J. H., Norm-conserving and ultrasoft pseudopotentials for first-row and transition elements. *J. Phys.: Condens. Matter* **1994,** *6*.

5. Vanderbilt, D., Soft self-consistent pseudopotentials in a generalized eigenvalue formalism. *Phys. Rev. B* **1990,** *41* (11), 7892-7895.

6. John P. Perdew; Kieron Burke; Ernzerhof, M., Generalized Gradient Approximation Made Simple. *Phys. Rev. Lett.* **1996,** *77*.

7. Cococcioni, M.; de Gironcoli, S., Linear response approach to the calculation of the effective interaction parameters in the LDA+U method. *Phys. Rev. B* **2005,** *71* (3).

8. Kresse, G.; Hafner, J., Ab initiomolecular dynamics for liquid metals. *Phys. Rev. B* **1993,** *47* (1), 558-561.

9. Kresse, G.; Hafner, J., Ab initiomolecular-dynamics simulation of the liquid-metal–amorphous-semiconductor transition in germanium. *Phys. Rev. B* **1994,** *49* (20), 14251-14269.

10. G. Kresse, J. F., Efficiency of ab-initio total energy calculations for metals and semiconductors using a plane-wave basis set. *Comput. Mat. Sci.* **1996,** *6*, 15-50.

11. G. Kresse, J. F., Efficient iterative schemes for ab initio total-energy calculations using a plane-wave basis set. *Phys. Rev. B* **1996,** *54*.

12. Monkhorst, H. J.; Pack, J. D., Special points for Brillouin-zone integrations. *Phys. Rev. B* **1976,** *13* (12), 5188-5192.

13. Ghosh, S.; Avellini, T.; Petrelli, A.; Kriegel, I.; Gaspari, R.; Almeida, G.; Bertoni, G.; Cavalli, A.; Scotognella, F.; Pellegrino, T.; Manna, L., Colloidal $CuFeS_2$ Nanocrystals: Intermediate Fe d-Band Leads to High Photothermal Conversion Efficiency. *Chem. Mater.* **2016,** *28* (13), 4848-4858.

14. Yasuo Kanazawa, K. K., Nobuo Morimoto, Bornite (Cu_5FeS_4): Stability and crystal structure of the intermediate form. *Can. Mineral.* **1978,** *16*, 397-404.

15. Jain, P. K.; Manthiram, K.; Engel, J. H.; White, S. L.; Faucheaux, J. A.; Alivisatos, A. P., Doped Nanocrystals as Plasmonic Probes of Redox Chemistry. *Angew. Chem. Int. Ed.* **2013,** *52* (51), 13671-13675.

16. Luther, J. M.; Jain, P. K.; Ewers, T.; Alivisatos, A. P., Localized surface plasmon resonances arising from free carriers in doped quantum dots. *Nat. Mater.* **2011,** *10* (5), 361-366.

17. Gaspari, R.; Della Valle, G.; Ghosh, S.; Kriegel, I.; Scotognella, F.; Cavalli, A.; Manna, L., Quasi-Static Resonances in the Visible Spectrum from All-Dielectric Intermediate Band Semiconductor Nanocrystals. *Nano Lett.* **2017,** *17* (12), 7691-7695.

APPENDIX B

Crystal structures of tetragonal and orthorhombic phase $AgFeS_2$

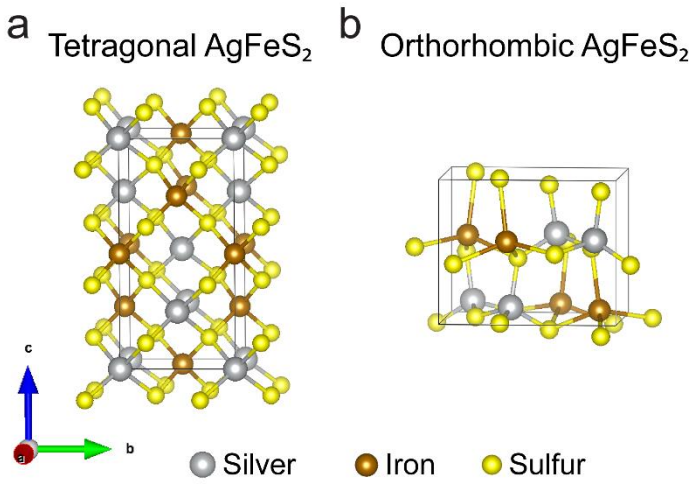

Figure B.1. Schematic representations of the crystal structure of (a) tetragonal and (b) orthorhombic phase $AgFeS_2$.

Comparison of experimental and simulated fast Fourier transform (FFT)

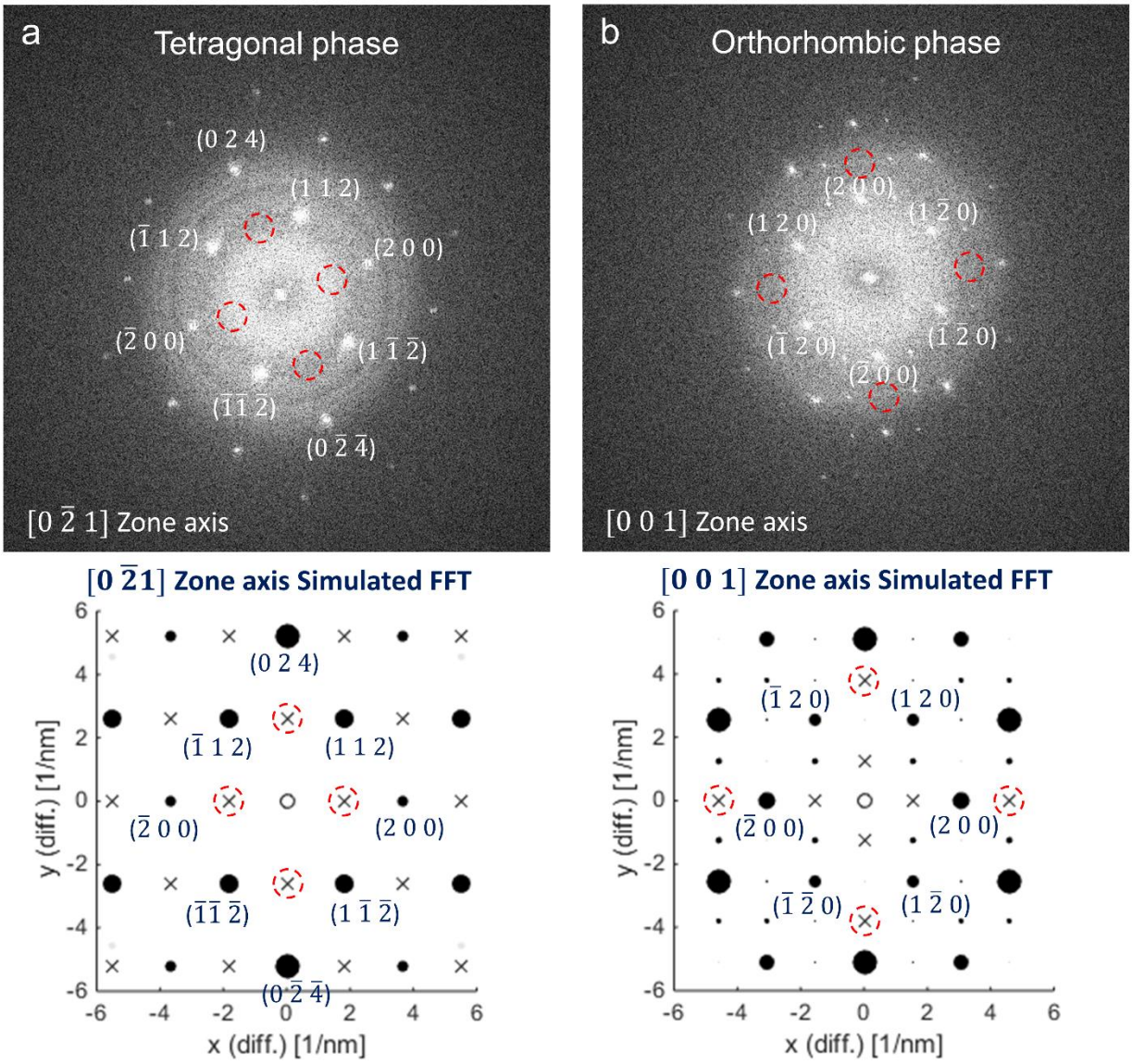

Figure B.2. Experimental and simulated fast Fourier transform (FFT) patterns of (a) tetragonal and (b) orthorhombic phase $AgFeS_2$ oriented along the zone axis [0 $\bar{2}$ 1] and [0 1 1], respectively.

Elemental analysis by energy-dispersive X-ray spectroscopy (EDXS)

Table B.1. Elemental compositions of representative tetragonal and orthorhombic phase $AgFeS_2$ NCs

Crystal structure	Atomic (%)			Nanocrystal Stoichiometry
	Ag	Fe	S	
Tetragonal	24.9	28.2	46.9	$AgFe_{1.13}S_{1.88}$
Orthorhombic	24.5	24.7	50.8	$AgFe_{1.01}S_{2.07}$

Size distribution histograms of tetragonal and orthorhombic AgFeS2 NCs

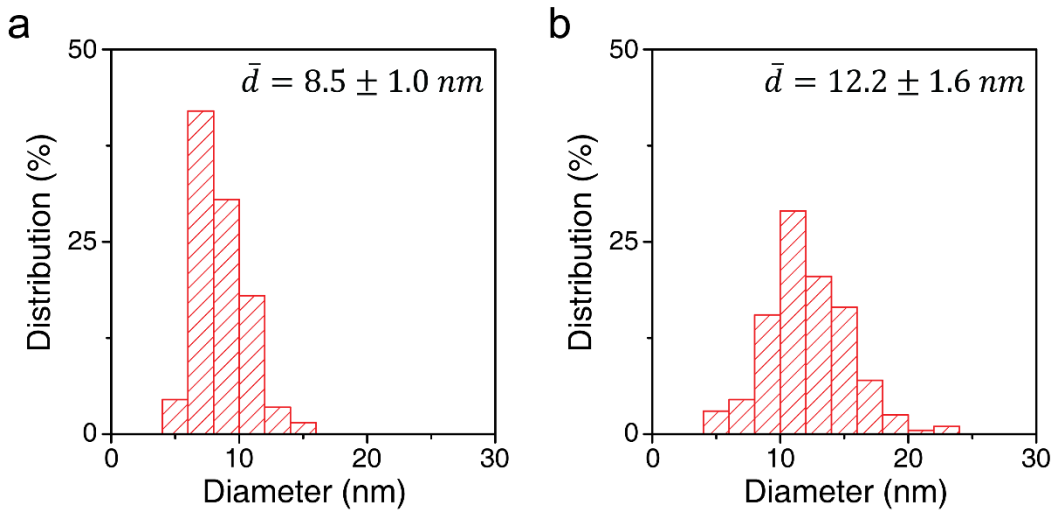

Figure B.3. Size distribution histograms of (a) tetragonal and (b) orthorhombic phase $AgFeS_2$ NCs synthesized with 12.8 and 0.4 mmol of OA and OAM, respectively. The corresponding size distributions were determined by analysis of 200 individual NCs.

More characterization of Ag NCs before the injection of sulfur

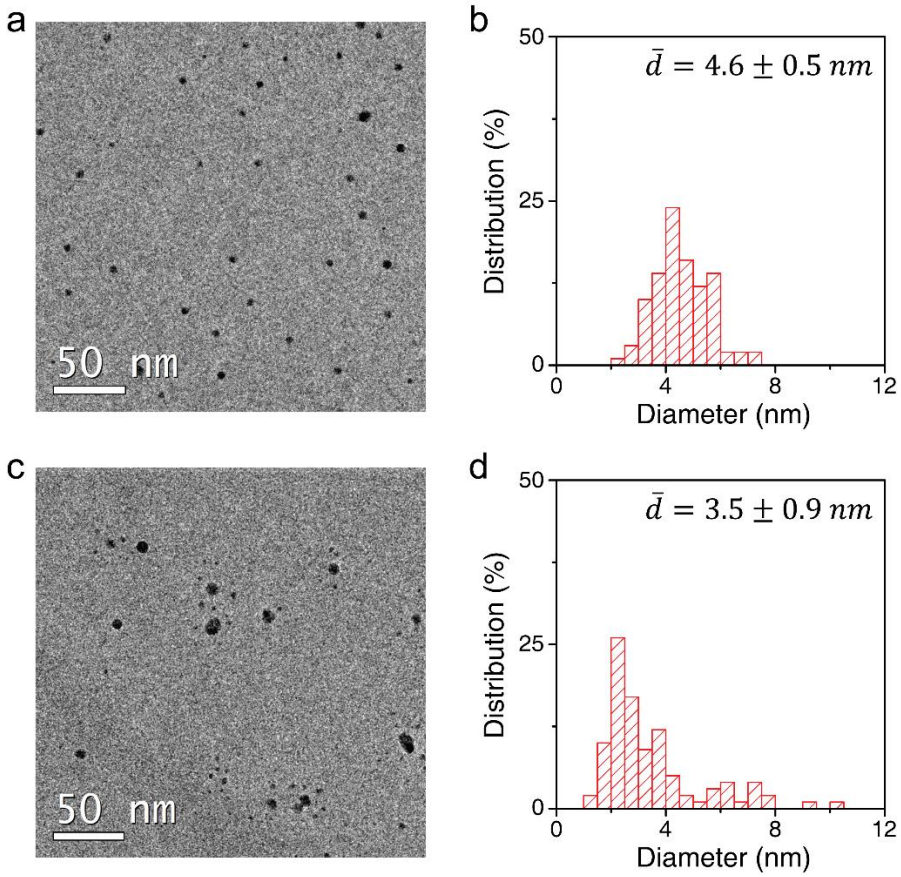

Figure B.4. TEM images and size distribution histograms of Ag NCs synthesized with (a) 12.8 and (b) 0.4 mmol of OA and OAM before the sulfur precursor injection.

Characterization of $CuFeS_2$ NCs

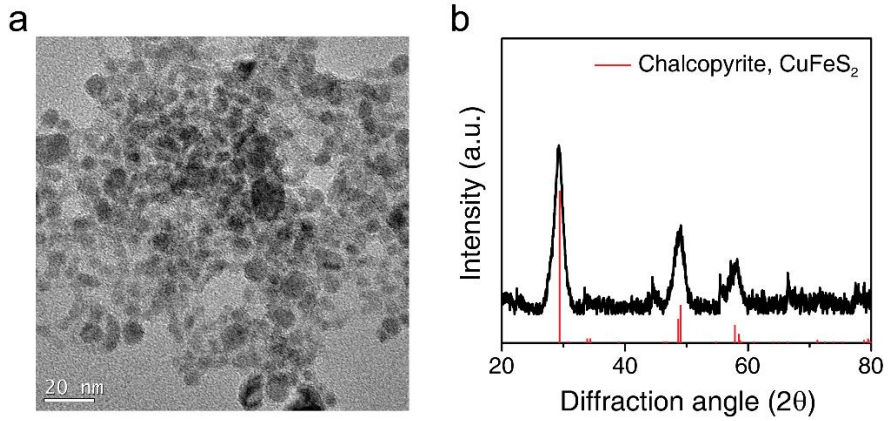

Figure B.5. (a) TEM image and (b) XRD pattern of $CuFeS_2$ NCs.

Control experiments on the synthesis of $AgFeS_2$ NCs

To clarify the role of oleic acid (OA) and oleylamine (OAM) in the phase-controlled synthesis of $AgFeS_2$ NCs, control experiments were conducted by progressively increasing the amount of OA or OAM.

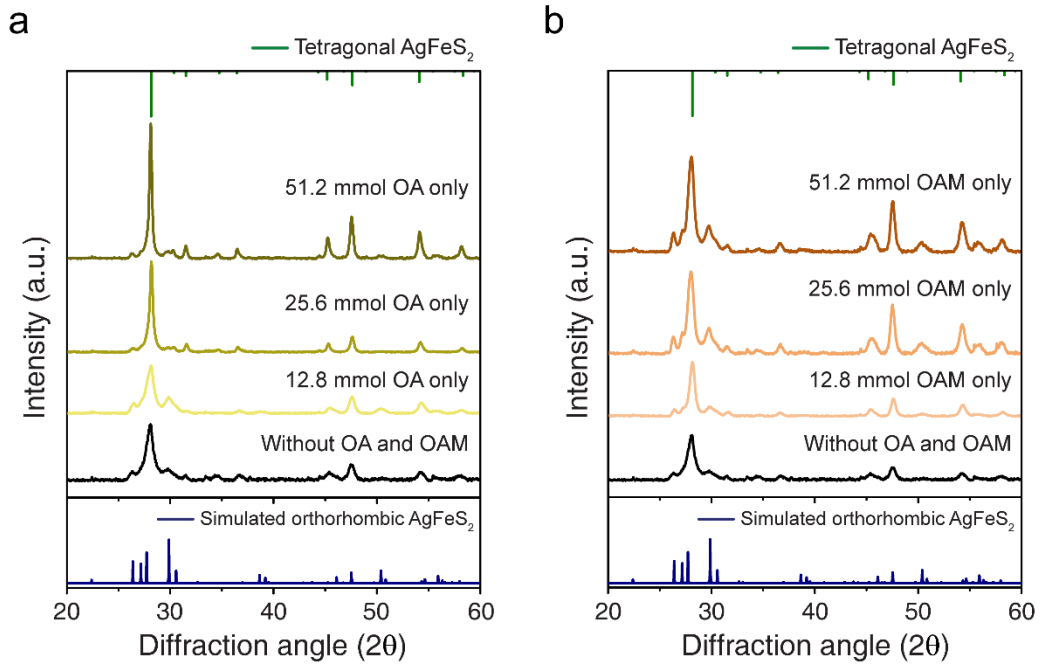

Figure B.6. Comparison of the XRD patterns of $AgFeS_2$ NCs synthesized with different amounts of (a) OA or (b) OAM.

Dependence of the $AgFeS_2$ NC extinction band on the refractive index of the surrounding medium

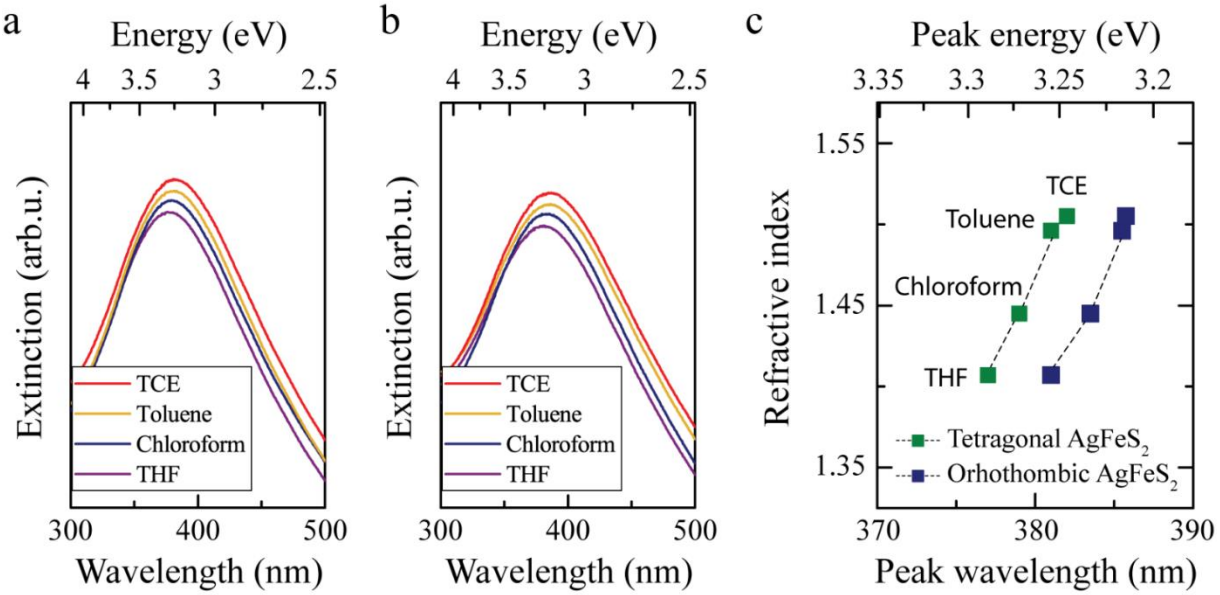

Figure B.7. Comparison of the extinction characteristics of the (a) tetragonal and (b) orthorhombic phase $AgFeS_2$ NCs in four different solvents (tetrahydrofuran, chloroform, toluene, and tetrachloroethylene), and (c) changes in the absorption peak position as a function of the environment refractive index.

Density functional theory (DFT) calculations

We modeled the tetragonal phase of $CuFeS_2$ and $AgFeS_2$ and the orthorhombic phase of $AgFeS_2$. Projector augmented wave (PAW) potentials[1-2] and unrestricted PBE+U[3-4] were used in VASP.[5-8] A cutoff energy of 500 eV was used for the plane wave basis. Since the tetragonal phases have been studied previously, we used some references for the geometries and lattice constants.[9-11] For the orthorhombic cell, we optimized the atomic positions and lattice constants on a 6x6x6 Monkhorst-Pack k-point mesh of the Brillouin zone with a value of 0.001 eV for Gaussian

smearing.[12] We assumed antiferromagnetic coupling of the Fe atoms and used a value of 3.1 and 2.8 for U on the Fe *d* orbitals of $CuFeS_2$ and $AgFeS_2$, respectively.

Density of States

We present the calculated atomic-projected density of states (DOS) for tetragonal $CuFeS_2$ and $AgFeS_2$, and orthorhombic $AgFeS_2$ in Figure 4.6 and B.8, respectively. The curves exhibit qualitative agreement with previous computing works.[9, 11] We find that both tetragonal and orthorhombic $AgFeS_2$ exhibit an intermediate band derived from Fe, and the valence band is a mixture of Ag/S. The valence-intermediate (VB-IB) gap is 0.83 eV for tetragonal $AgFeS_2$ and 1.28 eV for orthorhombic $AgFeS_2$. The VB-IB gap is in good agreement with previously computed value of 0.99 eV, and the $AgFeS_2$ band gap agrees well with experimental results of 0.88/1.2 eV.[11, 13-14]

Permittivity

The real component of the permittivity was computed under the independent-particle approximation and reported for $CuFeS_2$ and $AgFeS_2$ in Figures 4.6 and B.8, respectively.[15] The parallel component is aligned along the *c* axis of the tetragonal structure. We find good agreement with previously computed real permittivity of $CuFeS_2$, where the real permittivity dips below 0 in the region 2-2.5 eV with a minimum around -3 to -5 as expected from the Fröhlich condition.[10] The real permittivity of tetragonal and orthorhombic $AgFeS_2$ are negative in the 2.5-3.5 eV region, which correlates with the increased VB-IB gap of $AgFeS_2$ relative to $CuFeS_2$ and change in absorption peak in Figure 4.5. The computational data supports a dielectric resonance at higher energy for $AgFeS_2$.

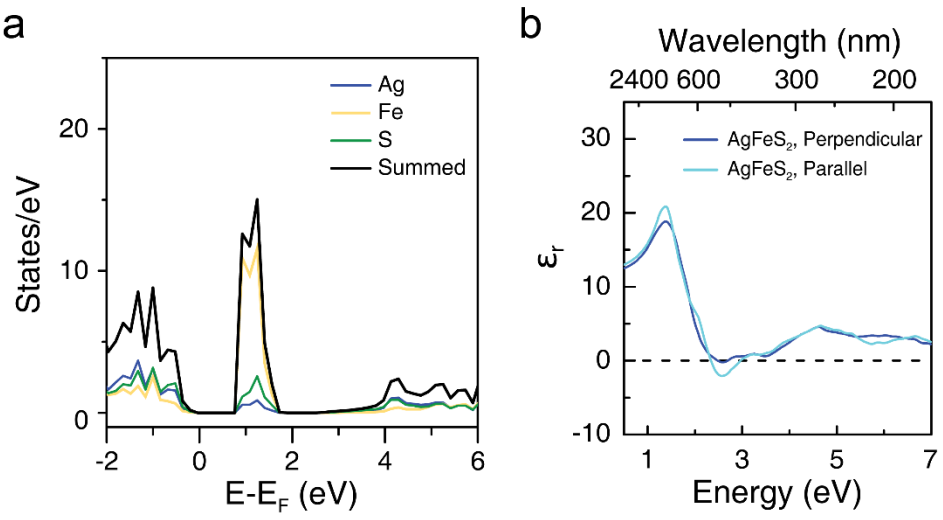

Figure B.8. Computed (a) DOS and (b) real permittivity for orthorhombic $AgFeS_2$.

References

1. Kresse, G.; Joubert, D., From ultrasoft pseudopotentials to the projector augmented-wave method. *Physical Review B* **1999,** *59* (3), 1758-1775.

2. Blöchl, P. E., Projector augmented-wave method. *Physical Review B* **1994,** *50* (24), 17953-17979.

3. Perdew, J. P.; Burke, K.; Ernzerhof, M., Generalized Gradient Approximation Made Simple. *Physical Review Letters* **1996,** *77* (18), 3865-3868.

4. Cococcioni, M.; de Gironcoli, S., Linear response approach to the calculation of the effective interaction parameters in the LDA+U method. *Physical Review B* **2005,** *71* (3), 035105.

5. Kresse, G.; Hafner, J., Ab initio molecular dynamics for liquid metals. *Physical Review B* **1993,** *47* (1), 558-561.

6. Kresse, G.; Hafner, J., Ab initio molecular-dynamics simulation of the liquid-metal--amorphous-semiconductor transition in germanium. *Physical Review B* **1994,** *49* (20), 14251-14269.

7. Kresse, G.; Furthmüller, J., Efficiency of ab-initio total energy calculations for metals and semiconductors using a plane-wave basis set. *Computational Materials Science* **1996,** *6* (1), 15-50.

8. Kresse, G.; Furthmüller, J., Efficient iterative schemes for ab initio total-energy calculations using a plane-wave basis set. *Physical Review B* **1996,** *54* (16), 11169-11186.

9. Ghosh, S.; Avellini, T.; Petrelli, A.; Kriegel, I.; Gaspari, R.; Almeida, G.; Bertoni, G.; Cavalli, A.; Scotognella, F.; Pellegrino, T.; Manna, L., Colloidal $CuFeS_2$ Nanocrystals: Intermediate Fe d-Band Leads to High Photothermal Conversion Efficiency. *Chemistry of Materials* **2016,** *28* (13), 4848-4858.

10. Gaspari, R.; Della Valle, G.; Ghosh, S.; Kriegel, I.; Scotognella, F.; Cavalli, A.; Manna, L., Quasi-Static Resonances in the Visible Spectrum from All-Dielectric Intermediate Band Semiconductor Nanocrystals. *Nano Letters* **2017,** *17* (12), 7691-7695.

11. Peng, X.; Liu, J.; Ming, C.; Li, B.; Zhao, Z.; Ye, K.; Zeng, M.; Zou, R.; Lu, X.; Hu, J., $AgFeS_2$ nanoparticles as a novel photothermal platform for effective artery stenosis therapy. *Nanoscale* **2020,** *12* (20), 11288-11296.

12. Monkhorst, H. J.; Pack, J. D., Special points for Brillouin-zone integrations. *Physical Review B* **1976,** *13* (12), 5188-5192.

13. Sciacca, B.; Yalcin, A. O.; Garnett, E. C., Transformation of Ag Nanowires into Semiconducting $AgFeS_2$ Nanowires. *Journal of the American Chemical Society* **2015,** *137* (13), 4340-4343.

14. Han, S.-K.; Gu, C.; Gong, M.; Wang, Z.-M.; Yu, S.-H., Colloidal Synthesis of Ternary $AgFeS_2$ Nanocrystals and Their Transformation to Ag2S-Fe7S8 Heterodimers. *Small* **2013,** *9* (22), 3765-3769.

15. Gajdoš, M.; Hummer, K.; Kresse, G.; Furthmüller, J.; Bechstedt, F., Linear optical properties in the projector-augmented wave methodology. *Physical Review B* **2006,** *73* (4), 045112.

APPENDIX C

Experimental Method

Materials and Reagents

Copper(II) chloride ($CuCl_2$, 97%), sulfur powder (S, 99.998%), iron(III) acetylacetonate ($Fe(acac)_3$, ≥99.9% trace metals basis), 1-dodecanethiol (DDT, ≥98%), oleylamine (OAM, ≥98%), 1-octadecene (ODE, technical grade 90%) were purchased from Sigma-Aldrich. Chloroform (HPLC grade, 99.9%), ultrapure trace metal grade hydrochloric acid (HCl, 34-37%), and nitric acid (HNO_3, 67-70%) were supplied by Fisher Scientific. Ethanol (200 proof) was purchased from Alfa Aesar. All materials were used as received without further purification.

Synthesis of Covellite (CuS) Copper Sulfide Nanocrystals

CuS NCs were prepared using a previously reported procedure by Su-Wen *et al*.[1] Briefly, 1.0 mmol of copper(II) chloride (134 mg) and 1.5 mmol of sulfur (48 mg) were combined with 2.5 mL of oleylamine and 7.5 mL of 1-octadecene in a glass vial under air-free conditions. Afterwards, the glass vial was placed in an oil bath at 160°C and the mixture was allowed to react at this temperature for 30 min. Subsequently, the vial was cooled to room temperature naturally, and 5mL of ethanol was added to the reaction solution at room temperature. Then, the solution centrifuged at 4000 rpm (1,863 x g) for 5 min. Finally, the nanocrystals were dispersed in 8 mL of chloroform, followed by centrifugation at 8000 rpm (7,452 x g) for 7 min to remove any byproducts.

Incorporation of Fe into CuS Template NCs Using 1-Dodecanethiol (1-DDT)

To incorporate Fe into CuS NCs, 0.4 mmol of $Fe(acac)_3$ was dissolved by a mixture of 6mL of oelylamine and 6.25mmol of 1-DDT (1.5mL) in a three-neck flask. The mixture was degassed

at 50°C for 1hr under vacuum. Afterwards, the flask was filled with nitrogen and heated to 160°C. Meanwhile, 3mL of covellite CuS NC dispersion (0.134M Cu+ ions, in oleylamine) was prepared. Once the temperature reached to 160°C, the prepared 3mL of 0.134M Cu-OAM dispersion was quickly injected, and the solution was held at this temperature for 15min. After 15min, the flask was cooled to 50°C and 10mL of chloroform was injected to prevent solidification. Then, 15mL of ethanol was added at room temperature, followed by centrifuging at 7000rpm (5,705 x g) for 15min. Finally, the precipitates were dispersed in 7mL of chloroform, and the re-dispersed solution was passed through a 0.45µm PTFE syringe filter.

Incorporation of Fe into CuS Template NCs Using Trioctylphosphine (TOP)

In a typical synthesis, a mixture of 0.4 mmol of $Fe(acac)_3$, 6mL of oelylamine, and 6.25mmol of TOP (2.8mL) was prepared in a three-neck flask. The mixture was degassed at 50°C for 1hr and subsequently heated to 160°C under nitrogen flow. In the meantime, 3mL of covellite CuS NC dispersion (0.134M Cu+ ions, in oleylamine) was prepared. Once the temperature reached to 160°C, the prepared 3mL of 0.134M Cu-OAM dispersion was rapidly injected, and the reaction was allowed to run for 15min. Afterwards, the flask was cooled to 50°C and 10mL of chloroform was injected to prevent solidification. The nanocrystals are precipitated by adding 15mL of ethanol at room temperature, followed by centrifuging at 7000rpm (5,705 x g) for 15min. Finally, the precipitates were dispersed in 7mL of chloroform, and the re-dispersed solution was further filtered using a PTFE syringe filter with a nominal pore diameter of 0.45µm.

Incorporation of Fe into CuS Template NCs Without Using 1-DDT or TOP

In a three-neck flask, 0.4 mmol of $Fe(acac)_3$ and 6mL of oelylamine were mixed, and degassed under vacuum at a temperature of 50°C for 1hr. Then, the flask was filled with nitrogen and heated

to 160°C. Meanwhile, 3mL of covellite CuS NC dispersion (0.134M Cu+ ions, in oleylamine) was prepared. After heating up to 160°C, the prepared 3mL of 0.134M Cu-OAM dispersion was swiftly injected, and the solution was held at this temperature for 15min. After 15min, the flask was cooled to 50°C and 10mL of chloroform was injected to prevent solidification. Then, 15mL of ethanol was added at room temperature, followed by centrifuging at 7000rpm (5,705 x g) for 15min. The final products were then dispersed in 7mL of chloroform, and the re-dispersed solution was further filtered using a PTFE syringe filter (pore size, of 0.45μm).

Characterization Methods

The size and morphology of the samples were characterized using a FEI Tecnai G2 F20 at an acceleration voltage of 200 kV. X-ray Diffraction (XRD) scans were collected by a Burker D8 Discover and analyzed by using the JADE software. Extinction spectra of the NC dispersions were recorded with a Varian Cary 5000 UV-Vis-NIR spectrophotometer. All measurements were carried out from the NC dispersions in chloroform. Inductively coupled plasma atomic emission spectroscopy (ICP-AES) analysis was performed using a Perkin Elmer Optima 8300 to determine the concentration of CuS dispersion.

References

1. Hsu, S.-W.; Ngo, C.; Bryks, W.; Tao, A. R., Shape Focusing During the Anisotropic Growth of CuS Triangular Nanoprisms. *Chemistry of Materials* **2015,** *27* (14), 4957-4963.